

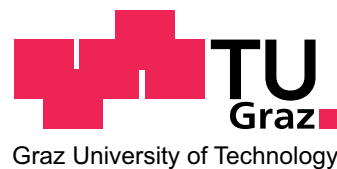
Manuel Johannes Zingl, BSc

**Real-frequency impurity solver
for dynamical mean-field theory
based on cluster perturbation theory**

MASTER THESIS

For obtaining the academic degree
Diplom-Ingenieur

Master Programme of
Technical Physics



Graz University of Technology

Supervisor:

Univ.-Prof. Dr.rer.nat. Enrico Arrigoni

Co-Supervisor:

Dr.techn. Markus Aichhorn

Institute of Theoretical and Computational Physics

Graz, September 2014

Abstract

The physics of materials with strongly correlated electrons is one of the most fascinating topics in modern solid-state research. Standard band structure methods often provide even qualitatively wrong results and are not suitable for an accurate description of strongly correlated systems and thus a many-body approach based on model Hamiltonians is required.

One of the most popular and successful methods available for strongly correlated materials is the dynamical mean-field theory (DMFT). To solve the self-consistent set of DMFT equations, it is necessary to determine the Green's function of the so-called Anderson impurity model. The main aim of this work is the development and the implementation of a new impurity solver based on exact diagonalization and an adapted version of cluster perturbation theory.

Subsequently, we test our method on the infinitely connected Bethe lattice by comparing the self-energy as well as the density of states to results obtained with exact diagonalization and other impurity solvers. A special focus is put on the Mott-Hubbard metal-insulator transition and the influence of electronic interaction on the quasiparticle weight. Furthermore, simple mixing and the Broyden method are investigated as mixing schemes to enhance the convergence of the DMFT self-consistency cycle.

Finally, we modify our solver to allow a treatment of multi-orbital impurity systems in the framework of DFT+DMFT, which is a general approach to combine realistic density functional theory (DFT) calculations with a successive application of DMFT to the strongly correlated subspace. The transition metal oxide SrVO_3 with its cubic crystal structure is chosen as a benchmark material.

With our real-frequency impurity solver we are able to obtain qualitatively correct results and to significantly improve on exact diagonalization for the same computational cost.

Kurzfassung

Die Physik der Materialien mit stark korrelierten Elektronen ist eines der faszinierendsten Gebiete der modernen Festkörperforschung. Standard Bandstrukturmethoden geben oft qualitativ falsche Resultate und sind nicht geeignet für die präzise Beschreibung von stark korrelierten Systemen, weswegen ein auf Modell-Hamiltonoperatoren basierender Vielteilchenzugang erforderlich ist.

Eine der gängigsten und erfolgreichsten Methoden der numerischen Vielteilchenphysik ist die dynamische Molekularfeldtheorie (DMFT). Um die selbstkonsistenten Gleichungen der DMFT zu lösen, muss die Green'sche Funktion eines sogenannten Anderson-Störstellenmodells bestimmt werden. Das Ziel dieser Arbeit ist die Entwicklung und die Implementierung einer neuen Lösungsmethode, welche auf exakter Diagonalisierung und einer adaptierten Version der Cluster-Störungstheorie basiert.

Anschließend testen wir unsere Methode auf dem unendlich koordinierten Bethe-Gitter, indem wir sowohl die Selbstenergie als auch die Zustandsdichte mit Resultaten von exakter Diagonalisierung und anderen Störstellenlösern vergleichen. Ein spezieller Fokus wird auf den Mott-Hubbard Metall-Isolator Übergang, sowie den Einfluss der elektronischen Wechselwirkung auf das Quasiteilchengewicht, gelegt. Um die Konvergenz des DMFT-Selbstkonsistenz-Zyklus zu verbessern, werden einfaches Mischen und die Broyden-Methode als mögliche Mischschemen untersucht.

Als letzten Teil dieser Arbeit modifizieren wir unseren Störstellenlöser für die Anwendung auf Mehrorbitalsysteme im Rahmen von DFT+DMFT. Dieser allgemeine Zugang kombiniert realistische Dichtefunktionaltheorierechnungen (DFT) mit einer darauffolgenden Anwendung von DMFT auf den stark korrelierten Unterraum. Das Übergangsmetalloxid SrVO_3 mit seiner kubischen Kristallstruktur wird als Benchmarkmaterial herangezogen.

Mit unserem Störstellenlöser für reelle Frequenzen gelingt es, qualitativ richtige Ergebnisse zu erzielen und eine signifikante Verbesserung im Vergleich zur exakten Diagonalisierung, bei gleichem Rechenaufwand, zu erreichen.

Acknowledgments

My sincere gratitude goes to my supervisor Prof. Enrico Arrigoni who supported me with great ideas and suggestions. I am especially thankful for giving me advices and the freedom to develop my own ideas.

I would like to express my gratitude to my second supervisor Markus Aichhorn for making himself available whenever I needed help and for his competence in answering my countless questions. I deeply appreciate his ongoing encouragement and support.

I am greatly indebted to Martin Nuss for his strong interest in my work and all the fruitful conversations we had. Without him and his previous work this thesis would not have been possible.

I like to thank Prof. Wolfgang von der Linden for his helpful proposals during our weekly group meetings.

I very much enjoyed the working atmosphere in the many-body theory group at the Institute of Theoretical and Computational Physics. I am particularly grateful to Ass. Prof. Lilia Boeri, Ass. Prof. Winfried Kernbichler, Werner Dobrautz, Antonius Dorda, Gerhard Dorn, Martin Ganahl, Faruk Geles, Christoph Heil, Jakob Neumayer, Max Sorantin, Georg Winkler and my office mates Zhian Asadzahdeh and Robert Triebl for all the discussions we had – not solely about physics.

For providing their CTQMC, NRG, and MPS data I thank Markus Aichhorn, Martin Nuss and Martin Ganahl.

Thanks are also due to our system administrator Andreas Hirzy for solving my computer issues and our secretary Brigitte Schwarz for her help with bureaucratic work.

Finally, I would like to thank my parents with all my heart for their continuous support and encouragement and most important Cornelia for all her love and patience.

Contents

1. Introduction	1
2. Strong correlations and the dynamical mean-field theory	3
2.1. Hubbard model	3
2.2. Method of Green's functions	5
2.3. The dynamical mean-field theory	7
2.4. Exact limits of DMFT	14
2.5. Mixing	14
2.6. Mott-Hubbard transition and quasiparticle weight	15
2.7. DFT + DMFT	19
2.7.1. Density functional theory	19
2.7.2. Hamiltonian and Wannier functions	20
2.7.3. DMFT for multi-orbital systems	22
3. Impurity solvers	23
3.1. Exact diagonalization	24
3.1.1. Cost function	25
3.1.2. Basis states and the Hamiltonian	26
3.1.3. Diagonalizing the Hamiltonian – ground state	29
3.1.4. Band Lanczos algorithm – Green's function	31
3.2. Cluster perturbation theory	33
3.2.1. CPT for the impurity model	35
3.2.2. Improving on the CPT approach	38
3.2.3. Determination of the parameter λ	39
4. Application to a single-orbital system on the Bethe lattice	45
4.1. The Bethe lattice	45
4.2. Calculation setup	46
4.3. Mixing	48
4.4. Fullfillment of the DMFT self-consistency	49
4.5. Self-energy and quasiparticle weight	51
4.6. Density of states	58

5. Application to a multi-orbital system - SrVO₃	65
5.1. The material and DFT results	65
5.2. DMFT calculation setup	68
5.3. DMFT results	69
6. Conclusions	75
A. Matsubara Green's function	77
B. Broyden's Method for DMFT	81
C. Generation of basis states with HAKMEM #175	83
D. Q-matrix formalism	85
E. Motivating the CPT equation	87
List of Abbreviations	89
List of Figures	91
Bibliography	93

1. Introduction

Nowadays, theoretical solid-state physics is able to explain physical properties of many materials, like simple metals, semiconductors and insulators. On the other hand, materials which are governed by a strong electronic correlation in narrow d- and f-orbitals turn out to be notoriously difficult to describe. In such materials the single electron picture fails, because the electrons experience a strong Coulomb repulsion. The pronounced influence of an electron on all the others prohibits the treatment of electrons as independent particles. Especially, in transition metals (e.g. copper, iron and vanadium) and their oxides correlations are the determinant factor for the emergence of fascinating properties. High- T_c superconductivity [1], colossal magneto-resistance [2] or a huge thermoelectric response [3] are just a few examples for the broad variety of exotic phenomena displayed by strongly correlated electron systems. But precisely the correlation effects, which lead to the richness of surprising phenomena, make the numerical and analytical study all the more challenging.

Density functional theory (DFT) [4, 5] calculations often give even qualitatively wrong results for such correlated materials (e.g. a compound is predicted to be a metal while it is in fact an insulator). Standard band structure methods are not sufficient for the treatment of strongly correlated materials and thus most theoretical attempts are based on the introduction and investigation of model Hamiltonians. That is, the full Hamiltonian is simplified to an effective Hamiltonian with only a few relevant degrees of freedom, which usually describe a few valence electron orbitals around the Fermi energy. The well-established Hubbard model [6] is one of the simplest, but it is considered to capture the essential physics of strongly correlated electron systems ranging from the Mott-Hubbard metal-insulator transition [7] and antiferromagnetism [8] to possible d-wave superconductivity [9].

Despite the lack of an exact solution for the Hubbard model, adequate theoretical approaches are obtained by using approximations. One of the most powerful attempts to cope with the Hubbard model, in particular regarding calculations for real materials, is the dynamical mean-field theory (DMFT) [10, 11, 12, 13]. DMFT, as discussed in chapter 2 of this thesis, is a non-perturbative method based on the idea of describing a correlated material in terms of a local model. The consequent mapping to a local system leads to the Anderson impurity model (AIM) [14] and a self-consistent set

of equations. Although the computational difficulty is now just shifted to solving the impurity model, the AIM is among the best studied quantum models and the advantage lies in the huge variety of different numerical tools available.

A simple and yet frequently used impurity solver is exact diagonalization (ED) [15], which is based on a finite discretization of the AIM bath degrees of freedom. Of course, the results are affected by severe finite-size effects and the solver is additionally limited by the exponential growth of the Hilbert space. However, ED does not suffer from a restriction to a certain class of problems and is therefore well suited for studying multi-orbital systems. ED turns out to be a very fast method that still allows for drawing qualitatively correct conclusions. In the first part of chapter 3 we give a review of ED and discuss the important aspects of an efficient numerical implementation.

The present work investigates a new approach based on cluster perturbation theory (CPT) [16, 17]. Within CPT a larger system is divided into small exactly solvable clusters while the coupling between the individual parts gets treated in strong-coupling perturbation theory. In principle, CPT allows to work with a larger impurity system for almost the same computational effort as ED. CPT and its variational extension named variational cluster approach (VCA) [18] were probed for the AIM by Martin Nuss [19, 20]. A logical consequence, as well as the aim of this work, is to develop an impurity solver for DMFT based on CPT. To stay within the scope of this thesis we focus only on CPT, but also VCA might be well suited as impurity solver. An introduction to CPT and a detailed guidance to our newly developed cluster based approach is elaborated in the second part of chapter 3.

In chapter 4 we benchmark our impurity solver for the single-orbital Hubbard model on the Bethe lattice. In the comparison of our results with other impurity solvers we consider the self-energy, the quasiparticle weight and the density of states as the important quantities of interest. Furthermore, we investigate Broyden's method as mixing scheme to enhance the convergence of to the DMFT solution. In a second step, our impurity solver is extended to multi-orbital problems and applied to the transition metal oxide SrVO_3 within the DFT+DMFT framework. The obtained results for SrVO_3 are presented in chapter 5.

2. Strong correlations and the dynamical mean-field theory

As discussed in the introduction, electrons in a solid are often described by an effective many-body model. One of the simplest model Hamiltonian – and yet without exact solution for dimensions higher than one – to describe strongly correlated materials is the so-called Hubbard model [6]. A prosperous approach to deal with this model is the dynamical mean-field theory (DMFT) [10, 11, 12, 13], which becomes exact in the limit of infinite dimensions. DMFT is mathematically formulated in terms of Green's functions and thus a short overview of the Green's functions theory is given before the introduction of DMFT. For simplicity reasons DMFT is first outlined for the single-orbital case and afterwards generalized to multi-orbital systems in terms of the ab-initio DFT+DMFT (or LDA+DMFT) method [12, 21, 22, 23].

2.1. Hubbard model

The principle picture leading to the Hubbard model is that of individual atoms (orbitals) arranged on a regular lattice, whereby the electrons can move to neighboring atoms and additionally experience an on-site interaction. Every lattice site is basically just one energy level (one orbital) which can be empty or occupied by either one spin up/down electron or one spin up and one spin down electron. The Pauli principle prohibits two electrons with the same spin sitting on the same lattice site.

The movement of electrons is modeled with a kinetic energy term that allows an electron sitting on a certain lattice site to hop to one of its neighboring sites. In principle, a direct hopping to any other site would be possible, but is due to the exponential diminution of atomic wave functions very unlikely. Therefore, very often only nearest-neighbor hopping is taken into account.¹ It should be noted that this treatment of the kinetic energy term in the Hubbard model is equivalent to a tight-binding approach.

¹For example, to describe high- T_c superconductors it is necessary to consider also next-nearest-neighbor hoppings [24].

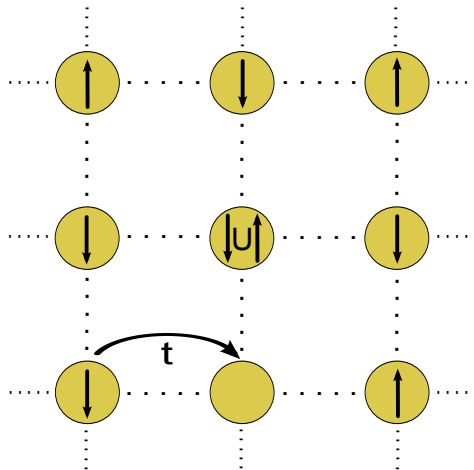


Figure 2.1.: Hubbard model describing electrons on a 2D square lattice. The electrons can move to neighboring sites with hopping strength t and additionally feel a local Coulomb repulsion U .

In addition to their movement the electrons interact with each other via the Coulomb interaction. In the Hubbard model those interactions are taken into account with a potential energy term, which is zero for empty sites and sites with one electron, but penalizes two electrons on the same site. Electronic interactions between different sites are neglected, because the apparently biggest contribution comes from two electrons occupying the same orbital.

Putting all of that together the single-band (single-orbital) Hubbard Hamiltonian in second quantization reads

$$H = \sum_{\langle i,j \rangle \sigma} t_{ij} \left(c_{i\sigma}^\dagger c_{j\sigma} + \text{h.c.} \right) - \mu \sum_{i\sigma} n_{i\sigma} + U \sum_i n_{i\uparrow} n_{i\downarrow}. \quad (2.1)$$

The kinetic energy (first term) models the electron movement by destructing it on site j and creating it again (with the same spin) on site i . This process is possible between all neighboring sites (denoted by $\langle i, j \rangle$) and for each spin σ . The potential energy (third term) counts the electrons on each site and adds an interaction energy U if a site is doubly occupied. The second term is the chemical potential of the system, which controls the filling. In the case of one electron per lattice site and particle symmetry (half-filling) the chemical potential is given by $\mu = U/2$. Dealing with the Hubbard Model might seem simple, but it turns out to be a truly difficult problem.

Moreover, the simple Hubbard model, although grasping the important physics, is hardly sufficient to describe the complexity of a real material. Hence, for a realistic description of materials two additional aspects have to be considered [25]: first, the effect of orbital degrees of freedom on the hopping of electrons and second, the role of intra-atom interactions between different orbitals on a certain site. That is why, the

Hubbard model has been extended to include *multiple* orbitals by assigning an orbital index to each lattice site and including additional orbital interaction terms [6, 26]

$$\begin{aligned}
 H = & - \sum_{\substack{\langle i,j \rangle \\ mm'\sigma}} t_{imjm'} \left(c_{im\sigma}^\dagger c_{jm'\sigma} + h.c. \right) - \mu \sum_{im\sigma} n_{im\sigma} \\
 & + \sum_i \left[U \sum_m n_{im\uparrow} n_{im\downarrow} + \sum_{m>m',\sigma} \left(U' n_{im\sigma} n_{im'\bar{\sigma}} + (U' - J) n_{im\sigma} n_{im'\sigma} \right) \right. \\
 & \left. - \sum_{m \neq m'} J \left(c_{im\downarrow}^\dagger c_{im'\uparrow}^\dagger c_{im'\downarrow} c_{im\uparrow} + c_{im'\downarrow}^\dagger c_{im'\uparrow}^\dagger c_{im\downarrow} c_{im\uparrow} + h.c. \right) \right]. \quad (2.2)
 \end{aligned}$$

The first line of equation 2.2 and the first interaction term in the second line are basically the same as in the single-orbital Hubbard model, but now carrying also an additional orbital index. The second (third) Coulomb term describes the interaction of two electrons with opposite (same) spin but sitting in different orbitals. This Hamiltonian essentially captures Hund's rule, because a configuration with two aligned spins has an energy lowered by J . Note that terms in the last line depict spin flip and pair hopping processes. The Hamiltonian 2.2 is often written in the more general form of the local interaction term

$$\begin{aligned}
 H = & - \sum_{\substack{\langle i,j \rangle \\ mm'\sigma}} t_{imjm'} \left(c_{im\sigma}^\dagger c_{jm'\sigma} + h.c. \right) - \mu \sum_{im\sigma} n_{im\sigma} \\
 & + \frac{1}{2} \sum_i \left[\sum_{\substack{\alpha\beta\gamma\delta \\ \sigma\sigma'}} \tilde{U}_{mm'm''m'''} c_{im\sigma}^\dagger c_{im'\sigma'}^\dagger c_{im''\sigma''} c_{im'''\sigma'''} \right], \quad (2.3)
 \end{aligned}$$

where $mm'm''m'''$ are orbital indices. $\tilde{U}_{mm'm''m'''}$ is the general 4-index interaction tensor.

2.2. Method of Green's functions

In this section, which is loosely based on the books [27, 28], a short introduction to the essential parts of the Green's function theory is given. More on the method of Green's function theory can be found therein.

The key quantity of interest is the fermionic single-particle² retarded Green's function

$$G_{\nu\nu'}(t, t') \equiv -i\Theta(t - t') \left\langle \left\{ c_\nu(t), c_{\nu'}^\dagger(t') \right\} \right\rangle, \quad (2.4)$$

²This Green's function is called *single-particle* Green's function, because it describes the propagation of a single particle in a full many-body system. Thus, the Green's function does also include all kind of correlation effects.

where $\{A, B\} \equiv AB + BA$ is the anticommutator. The indices $\nu = \{im\sigma\}$ and $\nu' = \{jm'\sigma'\}$ are composed indices of the lattice site, the orbital and the spin. If the Hamiltonian H is independent of time, i.e. the system is translationally invariant in time, the retarded Green's function only depends on the time difference $\tau = t - t'$. Hence, it is convenient to Fourier transform the Green's function to the frequency domain

$$G_{\nu\nu'}(\omega) = \int_{-\infty}^{+\infty} d\tau G_{\nu\nu'}(\tau) e^{i\omega\tau}. \quad (2.5)$$

To ensure the convergence of the integral $\omega \rightarrow \omega + i\eta$ has to be used, where $\eta = 0^+$ is a positive infinitesimal. This is necessary, because the Green's function has poles on the real axis exactly at the excitation energies of the system. Introducing a small η shifts the poles off the real axis into the lower complex half-plane and makes $G_{\nu\nu'}(\omega)$ analytic in the upper half-plane. As the Hubbard model is infinite and translationally invariant, a second Fourier transform is usually performed to obtain the Green's function in momentum space $G(\mathbf{k}, \omega)$. This retarded Green's function is of major interest, because the spectral function is embedded in its imaginary part

$$A(\mathbf{k}, \omega) = -\frac{1}{\pi} \Im [G(\mathbf{k}, \omega + i\eta)]. \quad (2.6)$$

Note that the spectral function $A(\mathbf{k}, \omega)$ has to obey the sum-rule

$$\int_{-\infty}^{+\infty} d\omega A(\mathbf{k}, \omega) = 1. \quad (2.7)$$

Summing the spectral function $A(\mathbf{k}, \omega)$ over \mathbf{k} gives³

$$\rho(\omega) = \hat{\sum}_{\mathbf{k}} A(\mathbf{k}, \omega), \quad (2.8)$$

which is the density of states (DOS) of the system. The electron density n , i.e. the filling of the system, is then given by

$$n = \int_{-\infty}^{\infty} d\omega \frac{\rho(\omega)}{e^{\beta\omega} + 1}. \quad (2.9)$$

Another important quantity is the so-called Matsubara Green's function, defined on the imaginary axis $i\omega$. This Green's function is directly connected to a finite temperature and in many cases easier to compute than the retarded Green's function. More on

³All \mathbf{k} sums $\hat{\sum}_{\mathbf{k}}$ in this work imply a normalized summation over the 1. Brillouin zone, i.e. $\hat{\sum}_{\mathbf{k} \in \text{BZ}} 1 = 1$.

Matsubara Green's functions can be found in appendix A. From this point onwards the complex variable z will be used for both imaginary and real frequencies.

A central concept in many-body physics is that of the self-energy $\Sigma(\mathbf{k}, z)$, which is defined by the Dyson equation

$$G^{-1}(\mathbf{k}, z) = G_0^{-1}(\mathbf{k}, z) - \Sigma(\mathbf{k}, z). \quad (2.10)$$

This equation expresses the full Green's function $G(\mathbf{k}, z)$ in terms of the non-interacting⁴ Green's function $G_0(\mathbf{k}, z)$ and the self-energy $\Sigma(\mathbf{k}, z)$. The self-energy contains *all* contributions coming from the Coulomb interaction. The Green's function of non-interacting electrons is given by

$$G_0(\mathbf{k}, z) = \frac{1}{z - \epsilon_{\mathbf{k}} + \mu}, \quad (2.11)$$

where $\epsilon_{\mathbf{k}}$ is the dispersion relation of the non-interacting tight-binding band. The dispersion is obtained by the Fourier transform of the hopping amplitudes t_{ij}

$$\epsilon_{\mathbf{k}} = \sum_j t_{ij} e^{i\mathbf{k}(r_i - r_j)}. \quad (2.12)$$

2.3. The dynamical mean-field theory

One of the most powerful methods to treat the models 2.1, 2.2 and 2.3 is the dynamical mean-field theory (DMFT). This theory, developed over the last 25 years, approximates the lattice model by an effective *dynamical* single-site problem [12]. The DMFT is based on two pivotal works namely

- the introduction of the limit of infinite lattice coordination q by Metzner and Vollhard in 1989 [10] and
- the self-consistent mapping of the Hubbard model onto a local impurity model by Georges and Kotliar in 1992 [11].

Metzner and Vollhard concluded that the self-energy $\Sigma(\mathbf{k}, z)$ becomes a *local* and thus \mathbf{k} -independent quantity in the limit of a lattice with infinite coordination q

$$\Sigma(\mathbf{k}, z) \stackrel{q \rightarrow \infty}{\approx} \Sigma(z) \quad (2.13)$$

Consequently, an exact mapping of the original physical problem onto an auxiliary *impurity* problem is possible. Strictly speaking, the whole translationally invariant

⁴or: free / bare / $U = 0$ Green's function

lattice can be replaced by identical impurity models – one at each lattice site.⁵ The auxiliary problem consists of an interacting impurity site coupled to an *infinite* non-interacting bath (figure 2.2).

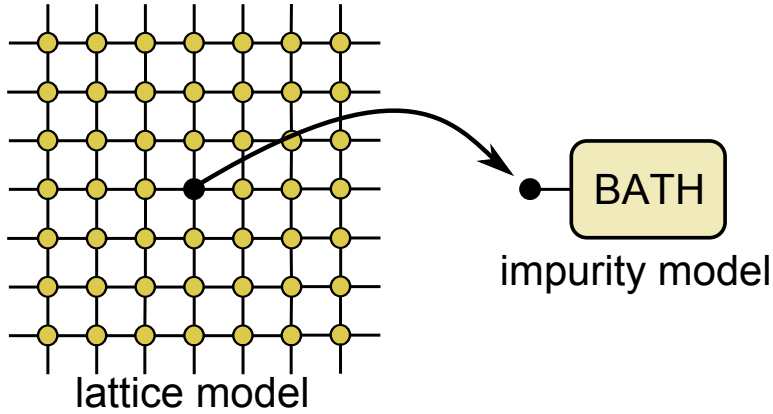


Figure 2.2.: Within the DMFT the lattice problem is mapped to a single impurity coupled to an effective bath.

This bath, determined in a self-consistent way, models the communication of the impurity site with the residual lattice. In the course of time electrons can come from the bath to occupy the impurity site and to eventually jump back again into the bath (see figure 2.3). As in the lattice model, the possible configurations on the impurity site are limited to the unoccupied, the single electron with spin up or down and the doubly occupied state with opposite spins.

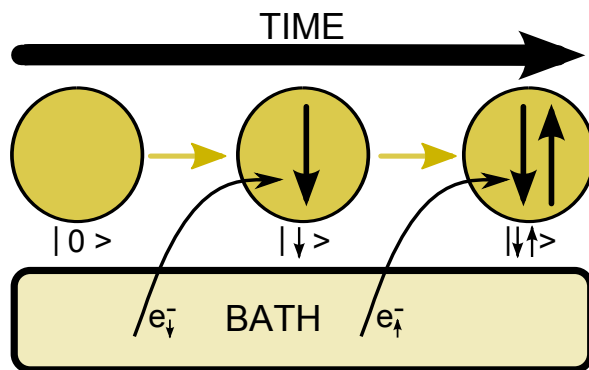


Figure 2.3.: The DMFT captures the dynamics of electrons on the impurity atom. One possible evolution of the occupation and how it fluctuates with time is shown.

⁵In this thesis only the paramagnetic phase is considered. For an antiferromagnetic phase two different types of lattice sites need to be taken into account due to the doubling of the unit cell.

Away from the special limit of infinite coordination the \mathbf{k} -independence of the self-energy is only an approximation

$$\Sigma(\mathbf{k}, z) \approx \Sigma(z). \quad (2.14)$$

However, it should be stressed that assuming a local self-energy is the *only* approximation within the DMFT. The interpretation of this assumption is that spatial correlations are neglected, but temporal correlations (fluctuations) are included and thus the quantum nature of each individual site is respected. This contrasts with standard mean-field theory where both spatial and temporal correlations are frozen out.

To allow a treatment of the impurity system in second quantization the coupled bath needs to be modeled with non-interacting sites. One representation of the impurity system is the so-called star geometry as shown in figure 2.4. In this geometry each bath site i is directly coupled to the impurity via the hopping t_{0i} . The associated Anderson impurity model (AIM) [14] for a single impurity site reads

$$H_{AIM} = \underbrace{Un_{0\uparrow}n_{0\downarrow} + \epsilon_0 \sum_{\sigma} n_{0\sigma}}_{\text{IMPURITY}} + \underbrace{\sum_{i=1,\sigma}^{\infty} \epsilon_i a_{i\sigma}^{\dagger} a_{i\sigma}}_{\text{BATH}} + \underbrace{\sum_{i=1,\sigma}^{\infty} t_{0i} (a_{i\sigma}^{\dagger} a_{0\sigma} + h.c.)}_{\text{COUPLING}}. \quad (2.15)$$

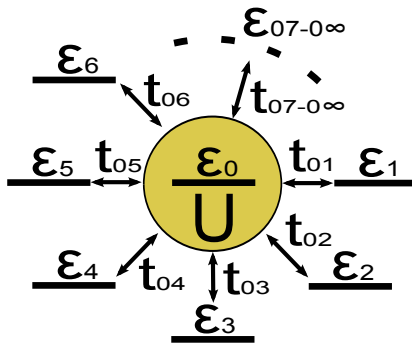


Figure 2.4.: AIM in *star* geometry, where each bath site is directly coupled to the impurity. Within DMFT the parameters ϵ_0 and U are fixed by the lattice model and the bath parameters get defined by the bath Green's function $\mathcal{G}_0(z)$.

The works mentioned above provide the cornerstones for the derivation of the DMFT self-consistency equations. Several ways to obtain those mean-field equations exist, e.g. the cavity method or an expansion around the atomic limit (those can be found in [13]). In this work we give a heuristic justification for the DMFT based on two very good reviews by A. Georges [12, 13].

First, we demand equivalence between the local lattice Green's function $G_{loc}(z)$ and the impurity Green's function $g(z)$ ⁶

$$G_{loc}(z) \stackrel{!}{=} g(z). \quad (2.16)$$

It should be emphasized that the impurity problem is a local problem, thus the impurity Green's function $g(z)$ is independent of \mathbf{k} . The local lattice Green's function $G_{loc}(z)$ is obtained by performing a \mathbf{k} -summation over the \mathbf{k} -dependent lattice Green's function $G(\mathbf{k}, z)$ and reads

$$G_{loc}(z) = \hat{\sum}_{\mathbf{k}} G(\mathbf{k}, z) = \hat{\sum}_{\mathbf{k}} \frac{1}{z - \epsilon_{\mathbf{k}} + \mu - \Sigma(z)}. \quad (2.17)$$

Taking the continuum limit of the \mathbf{k} -sum in equation 2.17 as well as transforming the integration variable to the energy ϵ yields

$$G_{loc}(z) = \int d\epsilon \frac{\rho_0(\epsilon)}{z - \epsilon + \mu - \Sigma(z)}. \quad (2.18)$$

Here, $\rho_0(\epsilon)$ is the non-interacting DOS of the lattice defined as

$$\rho_0(\epsilon) \equiv \hat{\sum}_{\mathbf{k}} \delta(\epsilon - \epsilon_{\mathbf{k}}). \quad (2.19)$$

In practice, expression 2.18 is often used instead of 2.17 to avoid the cumbersome \mathbf{k} -summation.

Equation 2.16 is central to DMFT, because it reflects the mapping of a lattice problem to an impurity problem. However, to conduct the mapping $G(\mathbf{k}, z)$ is needed, but that is actually the desired quantity we want to obtain within DMFT. In other words, the correct impurity model remains to be found in an iterative manner, which will lead us to the DMFT self-consistency cycle.

To conduct the mapping to the impurity model the Dyson equation is used to obtain the bath Green's function $\mathcal{G}_0(z)$

$$\mathcal{G}_0(z) = [G_{loc}^{-1}(z) + \Sigma(z)]^{-1}. \quad (2.20)$$

Note that this is *not* the free lattice Green's function, but the local Green's function with locally removed interaction. $\mathcal{G}_0(z)$ is a quantum generalization of the effective Weiss field in standard mean-field theory. It accounts for the electronic motion from the impurity site through the lattice and back to impurity site, where $\Sigma(z)$ is present

⁶Capital letters are denoted to Green's functions of the physical lattice system and small letters to Green's functions of the impurity system.

at every site except on the impurity site itself. The crucial point is that $\mathcal{G}_0(z)$ is exactly the free Green's function of the *impurity* model

$$g_0(z) = \mathcal{G}_0(z), \quad (2.21)$$

and thus defines the corresponding impurity system. The parameters of the impurity site (U and $\epsilon_0 = -\mu$) are given by the lattice Hamiltonian, but the bath on-site energies ϵ_i and the hopping parameters t_{0i} of the Hamiltonian 2.15 have to be determined from the bath Green's function \mathcal{G}_0 in compliance with equation 2.21. In fact, these parameters enter only through the hybridization function

$$\Delta(z) = \sum_{i=1}^{\infty} \frac{|t_{0i}|^2}{z - \epsilon_i}, \quad (2.22)$$

which is nothing else but the bath contribution to the non-interacting impurity Green's function

$$g_0^{-1}(z) = z + \mu - \Delta(z). \quad (2.23)$$

From equations 2.17, 2.20, 2.21, 2.22 and 2.23 follows the DMFT self-consistency condition

$$G_{loc}(z) = \hat{\sum}_{\mathbf{k}} \frac{1}{G_{loc}^{-1}(z) - \epsilon_{\mathbf{k}} + \Delta(z)} = \hat{\sum}_{\mathbf{k}} \frac{1}{G_{loc}^{-1}(z) - \epsilon_{\mathbf{k}} + \sum_{i=1}^{\infty} \frac{|t_{0i}|^2}{z - \epsilon_i}}. \quad (2.24)$$

The task of DMFT can be seen as finding the correct parameters t_{0i} and ϵ_i to fulfill equation 2.24. Usually, this has to be done in an iterative way, which includes the crucial step of solving the impurity problem. The simplest method, and most often used, is the forward iteration scheme (DMFT cycle) as shown in figure 2.5:

1. An initial guess for the self-energy $\Sigma(z)$ is required as starting point. Unless we know better, the non-interacting case ($\Sigma(z) = 0$) serves as an appropriate guess. If results from previous calculations with a similar interaction strength U are at hand, those might already offer a starting point close to the desired solution.
2. The local Green's function $G_{loc}(z)$ is calculated with equation 2.17 or 2.18. Additionally, the chemical potential μ should be adjusted at this point to ensure the desired filling n (equation 2.9) of the system.
3. Next, the bath Green's function is obtained from equation 2.20, which also provides the parameters t_{0i} and ϵ_i of the AIM Hamiltonian 2.15.
4. An appropriate impurity solver is used to calculate the impurity Green's function $g(z)$ and subsequently the self-energy $\Sigma(z)$ via the Dyson equation

$$\Sigma_{imp}(z) = g_0^{-1}(z) - g^{-1}(z). \quad (2.25)$$

5. Due to the assumption of a purely local self-energy, $\Sigma_{imp}(z)$ is used as the desired self-energy for the lattice

$$\Sigma^{\text{new}}(z) = \Sigma_{imp}(z) \quad (2.26)$$

and is now set as input self-energy for the next iteration (step 2).

6. Self-consistency is reached when $\Sigma(z)$ ⁷ is converged and that can be checked with

$$|\Sigma^{\text{new}}(z) - \Sigma(z)| < \text{tol}. \quad (2.27)$$

Surprisingly, this simple forward iteration shows already a fast convergence. Although a critical slowing down is observed in regimes close to phase transitions, usually less than 20 iterations are enough to converge the DMFT cycle. In difficult regimes more iterations are necessary and the initial starting point might become important. Simple mixing or the modified Broyden's method can be used (see section 2.5) to enhance the convergence properties of the DMFT cycle.

Typically, the adjustment of the chemical potential μ in step 2 of the DMFT cycle is only done every few iterations, because it requires a repeatedly evaluation of equation 2.17 or 2.18, which can be computationally demanding. As the filling n is a monotonously increasing function of the chemical potential μ the use of a bisection method is favorable.

The only inputs necessary for a DMFT calculation are

- the parameters of the Hubbard model – U and μ (or the filling n) and
- the dispersion relation of the non-interacting system $\epsilon_{\mathbf{k}}$, respectively the non-interacting DOS $\rho_0(\epsilon)$.

It should be mentioned that the real bottleneck is now transferred to solving the arising impurity problem, but fortunately multiple numerical tools are available to deal with the AIM. Those range from methods based on quantum Monte Carlo (e.g. HFQMC [29], CTQMC [30]) and renormalization group techniques (e.g. NRG [31], DMRG [32]) to perturbative approaches (e.g. IPT [33], NCA [34]). Still, obtaining the Green's function of the impurity problem constitutes the crucial point in every DMFT calculation. The different numerical approaches have all their advantages and disadvantages, thus the appropriate choice of method depends strongly on the application.

In calculations for N -orbital system the self-energy and the Green's functions carry an extra orbital index, which turns them into $N \times N$ matrices. Additionally, the impurity Hamiltonian itself needs to be altered to a system with N interacting orbitals coupled

⁷Of course, other quantities can serve as convergence indicator, e.g. $\mathcal{G}_0(z)$ or equivalently the parameters t_{0i} and ϵ_i .

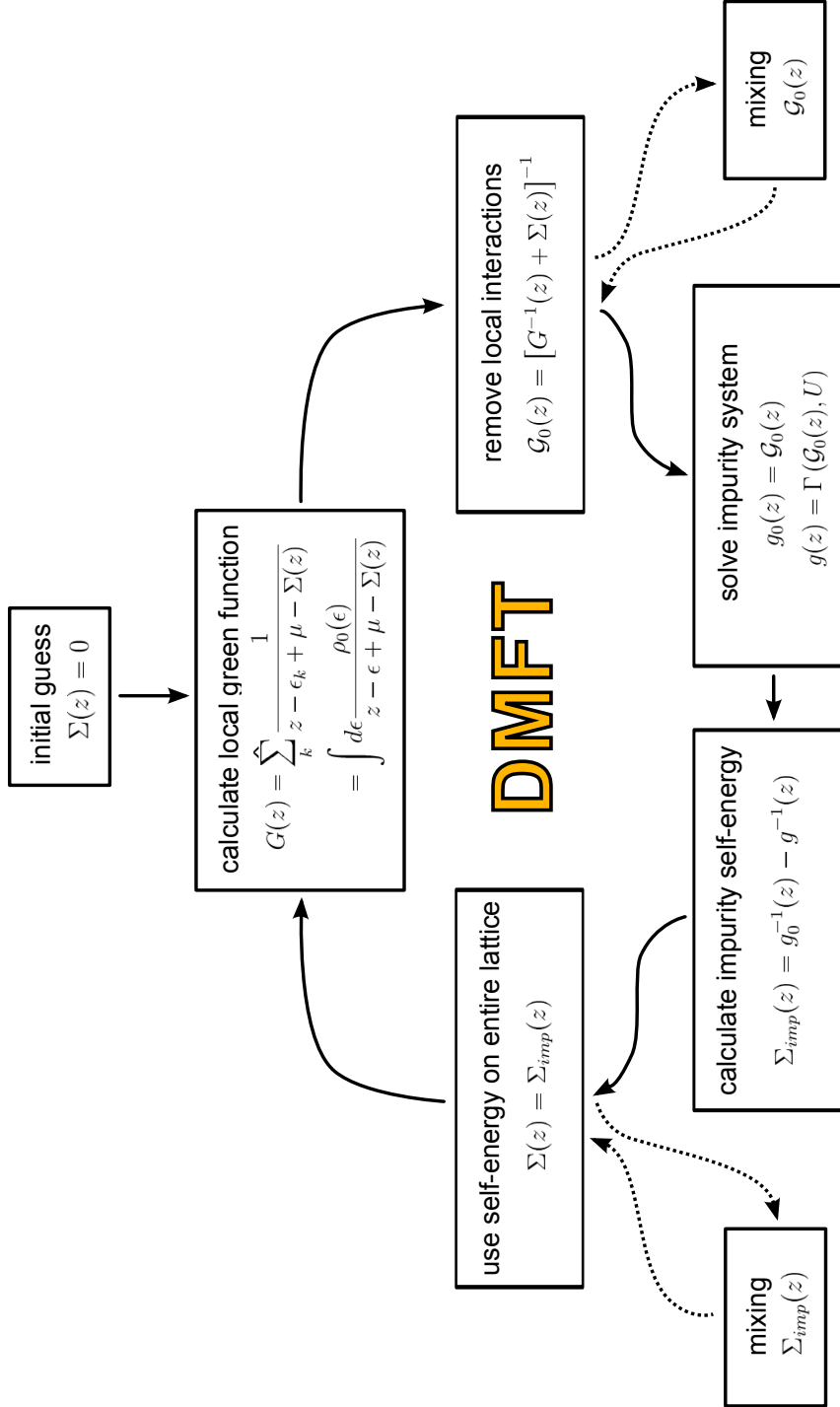


Figure 2.5.: The DMFT self-consistency cycle. Starting from an initial guess for the self-energy $\Sigma(z)$ the local lattice Green's function $G_{loc}(z)$ is obtained in the first step. Next, the bath Green's function $\mathcal{G}_0(z)$ is calculated with the Dyson equation. Solving the impurity model, which is defined by the bath Green's function, gives the impurity Green's function $g(z)$ and leads via the Dyson equation to a new self-energy $\Sigma(z)$. The updated self-energy gets then injected again into the first step. The whole procedure is iterated until convergence is reached. Optional mixing in $\Sigma(z)$ or $\mathcal{G}_0(z)$ can be used to achieve a faster convergence (see section 2.5).

to an appropriate bath⁸. The bath geometry itself depends on the concerned material and its symmetries, but a common choice is to couple one chain of non-interacting sites to each impurity orbital.

Modeling a real material with a Hubbard Hamiltonian and mapping the full lattice problem to an effective impurity problem is of course an approximation. Nevertheless, the DMFT has provided many valuable insights into the nature of strongly correlated materials.

2.4. Exact limits of DMFT

The DMFT approximation 2.14 and consequently the mapping to an impurity problem becomes exact in three limits [12]:

1. **Non-interacting limit** ($U = 0$)

The self-energy vanishes ($\Sigma(z) = 0$) and is therefore trivially \mathbf{k} -independent.

2. **Atomic limit** ($t_{ij} = 0$)

Due to the missing hopping between sites this case describes disconnected atoms with $\epsilon_{\mathbf{k}} = 0$. The hybridization vanishes and the self-energy can only have on-site components.

3. **Limit of infinite connectivity (or infinite dimension)** ($q \rightarrow \infty$)

As shown by Metzner and Vollhard [10], the self-energy becomes a local quantity for a lattice with infinite coordination number q . This statement is similar for the mean-field approximation in classical statistical mechanics.

It turns out that also for low coordination numbers (e.g. for a 3D material) DMFT provides a surprisingly good approximation, because the theory is bounded by both Hubbard limits (1. and 2. above) and additionally by the limit of infinite coordination.

2.5. Mixing

Mixing schemes are commonly used for density functional theory (DFT) calculations and are implemented to accomplish a faster approach to self-consistency [35, 36]. Moreover, oscillations between different solutions can be avoided, which would prohibit further convergence. Such mixing schemes can also be applied to DMFT calculations [37].

⁸The interacting orbitals are essentially the local part of Hamiltonian 2.3.

In principle, the DMFT cycle can be understood as a functional $\mathcal{F}[\Sigma(z)]$. The N -th iteration is then equivalent to

$$\Sigma^{N+1}(z) = \mathcal{F}[\Sigma^N(z)] \quad (2.28)$$

and the self-consistent solution is a fixed-point $\hat{\Sigma}(z)$ of the mapping \mathcal{F} , obeying

$$\mathcal{F}[\hat{\Sigma}(z)] = \hat{\Sigma}(z) \quad (2.29)$$

In this scope, the DMFT cycle is nothing else but searching for a fixed-point solution of the mapping \mathcal{F} . Indeed, reaching self-consistency (where $\Sigma^{N+1}(z) = \Sigma^N(z)$) corresponds to solving a non-linear equation.⁹ As mentioned above, the simplest approach is to inject $\Sigma^N(z)$ back into \mathcal{F} until convergence is reached.

A common way to enhance convergence is to mix $\Sigma(z)$ (or the Weiss field $\mathcal{G}_0(z)$) of two consecutive iterations. Simple mixing is done by linearly adding a certain fraction of the previous self-energy to the self-energy of the current iteration.

$$\Sigma^{N+1}(z) = \alpha \mathcal{F}[\Sigma^N(z)] + (1 - \alpha) \Sigma^N(z) \quad \alpha \in (0, 1) \quad (2.30)$$

Of course, with the parameter α the convergence behavior of the DMFT loop can be strongly influenced. However, if α is chosen too large the effect due to mixing might be low and if chosen too small the DMFT cycle might converge very slowly. Care is advisable for small α , because then the self-energy will not differ much between two consecutive iterations. In this case the stopping criterion given by equation 2.27 should be tightened.

A more sophisticated mixing method is required especially for calculations in the regime around a phase transition. Contrary to simple mixing, Broyden's method [37] incorporates all previous iterations and solves the non-linear system with a quasi-Newton-Raphson procedure. Details on Broyden's method are discussed in appendix B and a comparison of different mixing schemes is shown in section 4.3.

2.6. Mott-Hubbard transition and quasiparticle weight

The physical properties of a correlated material depend strongly on the interaction strength U . With increasing electronic repulsion the electrons of a metallic material become more and more localized to eventually undergo a transition into an insulator. Such a metal-insulator transition can be experimentally driven by temperature, pressure, or doping. This so-called Mott-Hubbard transition [38, 39], is central to the

⁹Strictly speaking it is a system of non-linear equation – one for each z value.

modeling of strongly correlated materials, because it directly describes the competition between kinetic energy and Coulomb repulsion [40]. The following considerations on the Mott-Hubbard transition are made for DMFT on the Bethe lattice. An introduction to the properties of this specific lattice is given in section 4.1.

One extreme limit is the case without interaction $U = 0$ (see figure 2.6 (a)). The electrons are delocalized and the material is well described by conventional band theory and a wave-like electron picture. The other extreme, where electrons localize $U > U_c$, corresponds to a particle-like electron character and atomic-like states. The DOS shows two separated bands (figure 2.6 (d)), one at the ionization energy $E_F + U/2$ and one at the electron affinity $E_F - U/2$ of the individual atoms.

The crucial and most interesting question is how the DOS evolves between these well-characterized limits (figure 2.6 (b and c)). In this intermediate correlation range the DOS is a mixture of the emerging Hubbard bands and quasiparticle features. DMFT offers an accurate description of the distinctive three-peak structure, whereby the Mott-Hubbard transition appears as spectral weight transfer from the quasiparticle peak to the Hubbard bands.

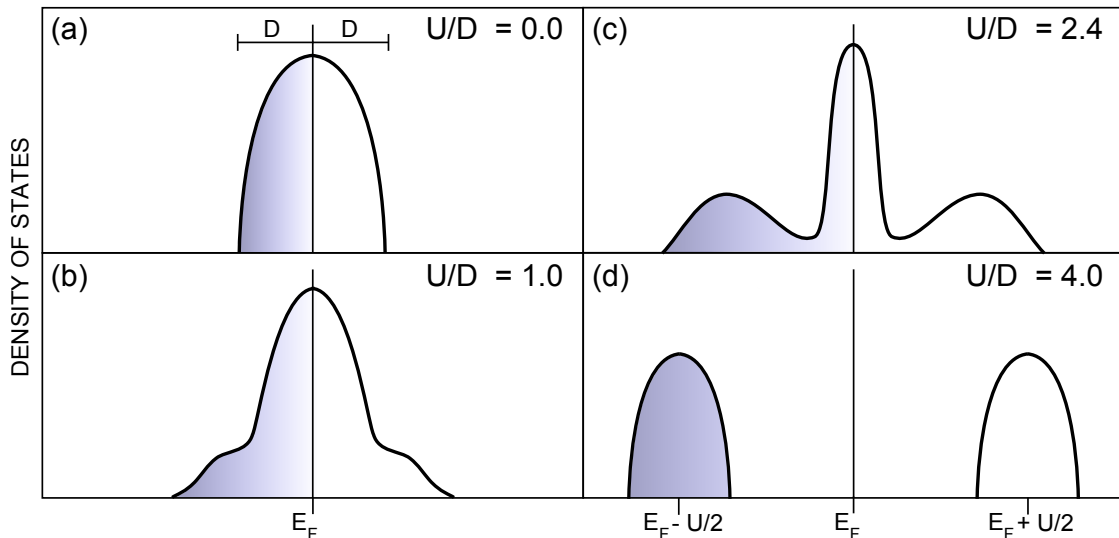


Figure 2.6.: Mott-Hubbard metal-insulator transition on the Bethe lattice. With increasing interaction strength U/D a characteristic three-peak structure emerges. At the phase transition the central quasiparticle peak vanishes and only two Hubbard bands are left.

The Mott-Hubbard transition for the specific scenario where the antiferromagnetic solution, i.e. magnetic ordering, is suppressed has already been studied multiple times [41, 42, 43, 44]. The phase diagram of the paramagnetic Hubbard model on the Bethe lattice is sketched in figure 2.7. The first order transition line $U_c(T)$ is surrounded by a hysteresis region, with borders $U_{c_1}(T)$ in the metallic and $U_{c_2}(T)$ in the insulating

phase. Within this coexistence region a metallic and an insulating solution exist. At the critical temperature all lines end in a second order critical point.

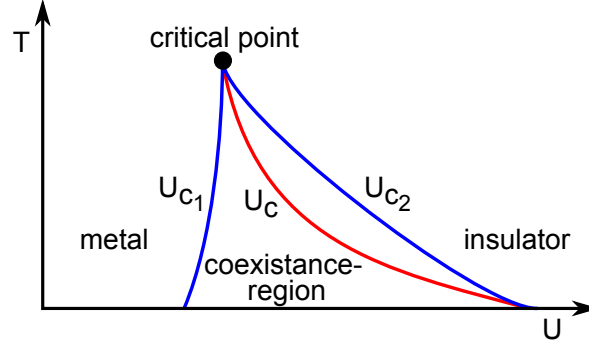


Figure 2.7.: Illustration of the phase diagram of the first order Mott-Hubbard metal-insulator transition line $U_c(T)$ and the two instability edges $U_{c1}(T)$ in the metallic and $U_{c2}(T)$ in the insulating phase.

A quantitative measure for describing the spectral weight of the central quasiparticle peak is the quasiparticle renormalization Z . Within Fermi liquid theory, excitations created by adding a particle to the system are described by free particles with a long life time and a renormalized mass. In this picture, a gas of interacting electrons can be seen as a gas of renormalized non-interacting quasiparticles. Therefore, the quasiparticle picture is only correct, if the retarded Green's function (and consequently the DOS) of the interacting system is similar to that of non-interacting particles around the Fermi energy. The following derivation is based on the argumentation in [27], but for the sake of simplicity and with regard to DMFT, a possible \mathbf{k} -dependence of the self-energy is here neglected.

First, we consider the retarded Green's function

$$G(\mathbf{k}, \omega) = \frac{1}{\omega - \epsilon_{\mathbf{k}} + \mu - \Sigma(\omega)} \quad (2.31)$$

and separate the self-energy $\Sigma(\omega)$ into its real and imaginary parts

$$G(\mathbf{k}, \omega) = \frac{1}{\omega - \epsilon_{\mathbf{k}} + \mu - \Re[\Sigma(\omega)] - i\Im[\Sigma(\omega)]}, \quad (2.32)$$

with $\epsilon_{\mathbf{k}} = \mathbf{k}^2/2m$ as the free electron energy.

In the second step we expand $\Sigma(\omega)$ to the first order in ω to anticipate the quasiparticle picture

$$G(\mathbf{k}, \omega) \approx \left[\omega - \epsilon_{\mathbf{k}} + \mu - \Re[\Sigma(0)] - \omega \frac{\partial \Re[\Sigma(\omega)]}{\partial \omega} \Big|_{\omega=0} \right]^{-1}. \quad (2.33)$$

The imaginary part of the self-energy can be set to zero around the expansion point, because it was shown by Luttinger that in the metal the imaginary part of every diagram contributing to the self-energy goes to zero as $(\epsilon_{\mathbf{k}} - \mu)^2$ or faster [45].

Rewriting equation 2.33 and defining

$$Z^{-1} \equiv 1 - \left. \frac{\partial \Re [\Sigma(\omega)]}{\partial \omega} \right|_{\omega=0} \quad (2.34)$$

and

$$\tilde{\epsilon}_{\mathbf{k}} \equiv Z (\epsilon_{\mathbf{k}} - \Re [\Sigma(0)]) \quad (2.35)$$

leads to

$$G(\mathbf{k}, \omega) \approx \frac{Z}{\omega - \tilde{\epsilon}_{\mathbf{k}} + \mu}. \quad (2.36)$$

This final Green's function is indeed describing non-interacting particles and thus justifies the quasiparticle picture. Concluding from equation 2.36, the interaction has two effects on the spectral function:

1. The integrated spectral weight around the Fermi energy is renormalized to Z .¹⁰
2. The renormalization acts on the dispersion resulting in a shift by $-Z\Re[\Sigma(0)]$ and more importantly in an effective mass

$$m^* = Z^{-1}m. \quad (2.37)$$

The emerging quasiparticles correspond to electrons gaining mass m^* due to fermionic correlations.

The Cauchy-Riemann condition for an analytic complex function necessarily implies

$$Z^{-1} = 1 - \left. \frac{\partial \Im [\Sigma(i\omega_n)]}{\partial \omega_n} \right|_{\omega_n \rightarrow 0} \quad (2.38)$$

with Matsubara frequencies ω_n . This quasiparticle renormalization Z serves as a general measure for the interaction induced effect on the DOS:

- $U = 0 \rightarrow Z = 1$
Uncorrelated system and hence no renormalization. The conventional band structure picture is valid.
- $0 \leq U \leq U_c \rightarrow 1 > Z > 0$
Renormalization due to correlation. System is in a metallic phase, because of

¹⁰Note that there must be a so-called incoherent part of the spectral function with integrated weight $1 - Z$ to guarantee a normalized DOS. This also demands $1 \geq Z \geq 0$.

spectral weight at the Fermi energy E_F , but the quasiparticle peak shrinks with increased U . U_c marks the critical U value of the Mott-Hubbard transition.

- $U \geq U_c \rightarrow Z = 0$

Correlation induced phase transition to a Mott insulator. The spectral weight at the Fermi energy E_F is zero.

2.7. DFT + DMFT

While the Hubbard model and its extensions can provide a qualitative description of real materials, they are still restricted to a few orbitals and depend on often unknown parameters (i.e. U and t). A prosperous technique for strongly correlated materials, which allows for parameter-free ab-initio calculations, is the DFT+DMFT method (or LDA+DMFT) [12, 21, 22, 23].

2.7.1. Density functional theory

Within the density functional theory (DFT) [4, 5] the intractable many-body problem of interacting electrons is reduced to a problem of non-interacting electrons moving in an *effective* potential. DFT considers the electron density $n(\mathbf{r})$ as key variable instead of the wave-function and is based on the two Hohenberg-Kohn theorems [46], stated here without proof:

1. For a given external potential v_{ext} , the total energy of a system is an unique functional of the ground state electron density.
2. The exact ground state density minimizes the energy functional $E[n(\mathbf{r})]$.

The minimization of the energy functional $\delta E[n(\mathbf{r})] = 0$ leads to the one-electron Schrödinger equation [47]

$$\left(-\frac{1}{2}\nabla^2 + v_s(\mathbf{r})\right)\varphi_i(\mathbf{r}) = \epsilon_i\varphi_i(\mathbf{r}), \quad (2.39)$$

where $\varphi_i(\mathbf{r})$ are the so-called Kohn-Sham orbitals. The electron density of N independent particles is then given by

$$n(\mathbf{r}) = \sum_{i=1}^N |\varphi_i(\mathbf{r})|^2, \quad (2.40)$$

with $v_s(\mathbf{r})$ being a density dependent potential. This effective potential reads

$$v_s(\mathbf{r}) = v_{\text{ext}}(\mathbf{r}) + \int d\mathbf{r}' \frac{e^2 n(\mathbf{r}')}{|\mathbf{r} - \mathbf{r}'|} + \frac{\delta E_{xc}[n(\mathbf{r})]}{\delta n(\mathbf{r})} \quad (2.41)$$

and includes the external potential (i.e. stemming from the nuclei and external fields), the Hartree term and the exchange-correlation term. The Hartree term describes the electrostatic contribution to the electron-electron interaction. All the remaining electron-electron interaction and the corrections to the kinetic energy are gathered in the exchange-correlation term, which remains unknown and has to be approximated. However, for an uniform electron gas the exchange-correlation energy can be calculated for all values of the electron density. One of the simplest approaches is the local density approximation (LDA) [48], which uses the exchange-correlation energy for an uniform electron gas also in the case when the electron gas is not uniform, but varies in space. The exchange-correlation energy is then given by

$$E_{xc}[n(\mathbf{r})] = \int d\mathbf{r} \epsilon_{xc}[n(\mathbf{r})] n(\mathbf{r}), \quad (2.42)$$

where the exchange-correlation energy density $\epsilon_{xc}[n(\mathbf{r})]$ does only depend on the local density.

Together, equations 2.39 to 2.42 form the set of Kohn-Sham equation, which can be solved in a self-consistent way to obtain the ground state energy and its density. Additionally, the Kohn-Sham equations yield a whole spectrum of single-particle states which are usually identified as the DFT band structure.¹¹ While for many materials qualitatively correct, this band structure fails completely to give reliable results for strongly correlated materials.

2.7.2. Hamiltonian and Wannier functions

In order to combine DFT with a many-body DMFT calculation it is necessary to obtain the required parameters of the underlying Hamiltonian. First, the strongly correlated subspace of the electronic DFT states has to be identified by selecting certain bands of interest. This subspace is subsequently expressed in terms of atomic-like orbitals. A suitable choice for such orbitals are the maximally localized Wannier functions [49, 50]. They are defined as the Fourier transform of the Bloch states $\varphi_{\mathbf{k}m\sigma}(\mathbf{r})$

$$w_{i\sigma}(\mathbf{r}) = \sum_{\mathbf{k}} e^{-i\mathbf{k} \cdot \mathbf{R}_i} \sum_m T_{im\sigma} \varphi_{\mathbf{k}m\sigma}(\mathbf{r}). \quad (2.43)$$

¹¹Strictly speaking, the interpretation as physical band structure is wrong, because the Kohn-Sham orbitals can only be considered as mathematical tools representing the actual problem.

$T_{imn\sigma}$ is a unitary transformation matrix determined by minimizing

$$\Omega = \sum_{in\sigma} (\langle w_{in\sigma} | r^2 | w_{in\sigma} \rangle - \langle w_{in\sigma} | \mathbf{r} | w_{in\sigma} \rangle^2), \quad (2.44)$$

which is the total spread of all Wannier functions. Wannier functions form an orthonormal basis set and resemble atomic orbitals closely, because they are centered on atoms and decay with increasing distance from the nuclei. For the uncorrelated subspace DFT can be seen as overall good approximation, but for the correlated subspace l the DFT fails and a local short-range correction is required. This leads to the many-body Hamiltonian for the strongly correlated subspace

$$H_{DMFT} = H_{DFT} + H_U^l - H_{DC}^l, \quad (2.45)$$

where H_{DFT} is the single-particle DFT part, H_U^l the effective local electron interaction and H_{DC}^l the double counting term. The DFT part is written as

$$H_{DFT} = - \sum_{\substack{\sigma ij \\ mm'}} t_{imjm'} c_{im\sigma}^\dagger c_{jm'\sigma} \quad (2.46)$$

with

$$t_{imjm'} = - \int d\mathbf{r} \bar{w}_{im\sigma}(\mathbf{r}) \left(-\frac{1}{2} \nabla^2 + v_s(\mathbf{r}) \right) w_{jm'\sigma}(\mathbf{r}). \quad (2.47)$$

The on-site terms $i = j$ are essentially describing a crystal-field while the terms $i \neq j$ are hopping integrals. The local orbital-dependent Coulomb interaction is given by¹²

$$H_U^l = \frac{1}{2} \sum_i \left[\sum_{\substack{mm'm''m'''' \\ \sigma\sigma'}} \tilde{U}_{mm'm''m''''}^l c_{im\sigma}^\dagger c_{im'\sigma'}^\dagger c_{im''\sigma''} c_{im'''\sigma'''} \right], \quad (2.48)$$

where

$$\tilde{U}_{mm'm''m''''}^l = \iint d\mathbf{r} d\mathbf{r}' \bar{w}_{im\sigma}(\mathbf{r}) \bar{w}_{im'\sigma'}(\mathbf{r}') \tilde{U}(\mathbf{r}, \mathbf{r}') w_{im''\sigma''}(\mathbf{r}) w_{im'''\sigma'''}(\mathbf{r}'). \quad (2.49)$$

$\tilde{U}(\mathbf{r}, \mathbf{r}')$ is the Coulomb interaction, but partially screened by the electrons of the uncorrelated subspace. Determining this Coulomb interaction is a difficult task and beyond the scope of this thesis. The interested reader should be referred to [51, 52].

The double counting term H_{DC}^l corrects the Hamiltonian for long-range Hartree and the mean-field exchange-correlation interaction, which have already been taken into account by the LDA energy functional and are included again via equation 2.49. Unfortunately, there is no rigorous way to determine this correction, but approximative

¹²Note that H_U^l has the same form as the local part of Hamiltonian 2.3

methods to estimate the double counting term are available [53]. If only one kind of orbitals¹³ is present in the correlated subspace and if no uncorrelated states are included in the model the double counting correcting can be written as

$$H_{DC}^l = \sum_{im\sigma} \epsilon_{DC}^\sigma n_{im\sigma}. \quad (2.50)$$

This is nothing else but a constant shift to the chemical potential. Anyway, the chemical potential has to be adjusted to give the correct filling and thus in this case the double counting does not need to be treated separately.

2.7.3. DMFT for multi-orbital systems

In the previous sections we have collected all required ingredients for a DMFT calculation of a real material. The local interaction parameters $\tilde{U}_{mm'm''m'''}^l$ of the Hamiltonian 2.45, which are the same for the corresponding impurity model, are determined by equation 2.49. The dispersion $\epsilon_{\mathbf{k}}^{eff}$ is calculated from the integrals 2.47 and the Fourier transform 2.12. Note that $\epsilon_{\mathbf{k}}^{eff}$ is now a matrix in the considered orbitals m , turning also the self-energy and all Green's functions into matrices. For example, the calculation of the local Green's function $\mathbf{G}_{loc}(z)$ reads

$$\mathbf{G}_{loc}(z) = \hat{\sum}_{\mathbf{k}} \frac{1}{(z + \mu) \mathbb{1} - \Sigma(z) - \epsilon_{\mathbf{k}}^{eff}}. \quad (2.51)$$

Often so-called one-shot DFT+DMFT calculations are performed, that is doing DFT and the consecutive DMFT step only once. However, the resulting charge density of the DMFT step can be put back into the Kohn-Sham potential $v_s(\mathbf{r})$ leading to a full charge self-consistent DFT+DMFT cycle [54]. This enlarged cycle is iterated until the charge density converges. In this case equation 2.39 is solved only once per iteration, because otherwise the information of the DMFT step would be lost and the previous Kohn-Sham wave-functions would be restored. Typically, the DMFT step is the computationally demanding part, for which reason a fast and efficient impurity solver is desired. One promising approach based on exact diagonalization will be discussed in the next chapter.

¹³For example t_{2g} as in this thesis

3. Impurity solvers

Generally, the AIM in star geometry, as given by Hamiltonian 2.15, can be unitarily transformed to any other geometry with infinitely many bath sites. The representation shown in figure 2.4, where an impurity site at the far left is coupled to an semi-infinite chain of non-interacting sites, is often used. In this case the impurity hybridizes only with one bath orbital – instead of infinitely many – but the bath possesses hoppings along the chain to compensate for that.

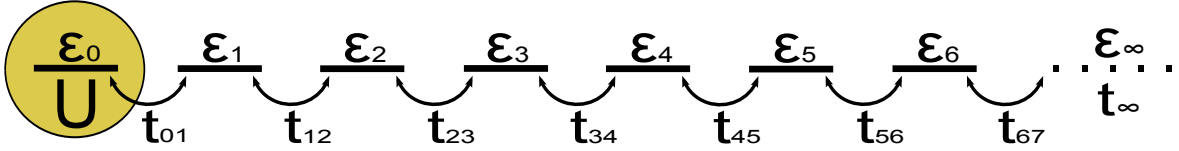


Figure 3.1.: AIM in *chain* geometry, where the impurity hybridizes only with one bath site. Within DMFT the parameters ϵ_0 and U are fixed by the lattice model and the bath parameters get defined by the bath Green's function $\mathcal{G}_0(z)$.

The corresponding Hamiltonian of the AIM in *chain* geometry reads¹⁴

$$\begin{aligned}
 H_{AIM}^{ED} = & \underbrace{U n_{0\uparrow} n_{0\downarrow} + \epsilon_0 \sum_{\sigma} n_{0\sigma}}_{\text{IMPURITY}} + \underbrace{\sum_{i=1, \sigma}^{L-1} \epsilon_i a_{i\sigma}^{\dagger} a_{i\sigma} + \sum_{i=1, \sigma}^{L-2} t_{i, i+1} (a_{i\sigma}^{\dagger} a_{i+1, \sigma} + h.c.)}_{\text{BATH}} \\
 & + \underbrace{t_{01} \sum_{\sigma} (a_{0\sigma}^{\dagger} a_{1\sigma} + h.c.)}_{\text{COUPLING}},
 \end{aligned} \tag{3.1}$$

where L is the total number of sites in the system and $L \rightarrow \infty$ corresponds to an infinitely large bath. Many analytical and numerical studies at zero temperature are based on this single-chain Hamiltonian. In the first part of this chapter we discuss the exact diagonalization (ED) impurity solver [15]. An introduction to cluster perturbation theory (CPT) [16, 17] and the elaboration of our newly developed cluster based approach is presented in the second part.

¹⁴It should be kept in mind that the used parameters are not the same as those in Hamiltonian 2.15, i.e. the star representation of the AIM. However, we will use the same symbols (ϵ, t and a) for readability reasons.

3.1. Exact diagonalization

Basically, exact diagonalization (ED) aims at solving the time-independent Schrödinger equation

$$H_{AIM}^{ED} |\phi\rangle = E |\phi\rangle \quad (3.2)$$

for the eigenvalues E and the eigenstates $|\phi\rangle$ of the Hamiltonian H_{AIM}^{ED} . Of course, this allows only to treat a system with a *finite* number of sites. As an example, the impurity model for the case $L = 6$ is shown in figure 3.2.

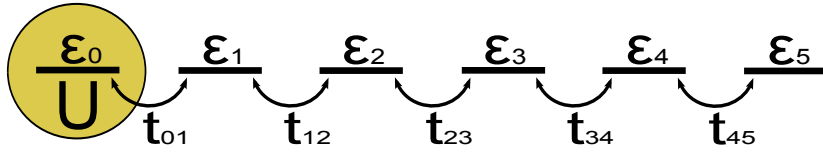


Figure 3.2.: Finite AIM of size $L = 6$.

Writing the impurity system in terms of a finite Hamiltonian comes with a discretization of the bath levels, which is in contrast to the original continuous bath spectrum. Additionally, the system size L is restricted to a small number of bath sites, so that it is still possible to diagonalize the Hamiltonian numerically. Hence, also the number of adjustable parameters \vec{a}^{15} is restricted to $2L - 1$. The computational difficulty of the problem is set by the total number of sites, due to the fact that the size of the full Hamiltonian matrix H_{AIM}^{ED} grows exponentially with system size. In most applications the total number of sites does not exceed twelve (or at most fifteen).

The procedure behind ED is simply to [55]

1. obtain the parameters of the impurity model,
2. generate the many-body basis states,
3. construct the Hamiltonian within this basis,
4. diagonalize the Hamiltonian and
5. calculate the full fermionic Green's function $g(z)$.

Due to the exponential growth of the Hilbert space with system size, some considerations for the practical implementation of this procedure are necessary. The most important aspects will be discussed in the following sections.

¹⁵The vector \vec{a} holds the hoppings t and the on-site energies ϵ of the bath.

3.1.1. Cost function

We have seen in section 2.3 that the impurity system is defined by the bath Green's function $\mathcal{G}_0(z)$. As a matter of fact, it is not possible to fulfill the DMFT condition $g_0(z) = \mathcal{G}_0(z)$ with only a limited number of parameters at hand. Instead, this condition must be approximately satisfied in some optimal way. Typically, a least-squares cost function is defined

$$\chi = \int W(z) |\mathcal{G}_0^{-1}(z) - g_0^{-1}(z, \vec{a})|^2 dz, \quad (3.3)$$

which has to be minimized with respect to the tunable parameters \vec{a} . The inverse of the non-interacting Green's function $g_0^{-1}(z, \vec{a})$ can be most easily generated from a continuous fraction expansion

$$g_0^{-1}(z, \vec{a}) = z - \epsilon_0 - \frac{t_{01}^2}{z - \epsilon_1 - \frac{t_{12}^2}{\dots - \frac{t_{L-2, L-1}^2}{z - \epsilon_{L-1}}}}. \quad (3.4)$$

Certainly, the cost function χ would vanish for $L \rightarrow \infty$, but for a finite system it can only be optimized. It should be emphasized that equation 3.3 is not uniquely defined and can take various forms [13, 56, 57] considering the following points:

- The frequency dependent weights $W(z)$ can be used to assess some frequencies stronger than others, but the choice of $W(z)$ does not follow any rigorous principle. In this work $W(z) = 1$ is used, because of the equal interested in the whole frequency range.
- The fitted quantity in the cost function χ could either be $\mathcal{G}_0^{-1}(z)$ or $\mathcal{G}_0(z)$. As the bath parameters are directly embedded in the hybridization function $\Delta(z)$ and thus in $\mathcal{G}_0^{-1}(z)$ (see equation 2.23), it is somewhat more reasonable to carry out the minimization directly in $\mathcal{G}_0^{-1}(z)$.
- Usually, the complex Euclidean distance summed over all frequencies is used to quantify the difference between $\mathcal{G}_0^{-1}(z)$ and $g_0^{-1}(z)$, as it appears to be the most natural definition. Nonetheless, other distances could be considered instead.
- The minimization can be performed either in $g_0(\omega + i\eta)$ on the real axis or in $g_0(i\omega_n)$ on the Matsubara axis. To circumvent the delta peaks occurring for real frequencies the minimization is often carried out on the Matsubara axis¹⁶. The advantage is due to the fact that $g_0(i\omega_n)$ is a continuous function which can be approximated much more easily, but using discrete Matsubara frequencies comes

¹⁶Then the integral in equation 3.3 is actually a sum over discrete Matsubara frequencies.

with a finite temperature T . Although $g_0(\omega + i\eta)$ consist only of (broadened) delta peaks on the real axis, the focus of this thesis lies on performing DMFT for real frequencies at $T = 0$, in particular regarding the investigated extension to ED.

Especially for a small impurity systems, the freedom of defining a suitable cost function does influence the resulting parameters and subsequently the final DMFT fixed-point. However, this dependence gets less critical the larger the impurity system is.

The cost function χ might be a function with many local minima, which can make it difficult to find the optimal parameters \vec{a} . In practice, minimization procedures such as the conjugate gradient method or simplex schemes turn out to be suitable choices. Every optimization procedure requires a frequent calculation of $g_0^{-1}(z)$ or its derivative, but fortunately this is a numerically inexpensive task in comparison to the diagonalization of H_{AIM}^{ED} . It is beneficial to start the minimization in consecutive iterations with the optimized parameters obtained in the previous iteration step.

3.1.2. Basis states and the Hamiltonian

First of all, it is necessary to define a suitable representation for the quantum basis states of the Hamiltonian. It is important that the basis set allows for [58]:

- a fast generation of the basis itself,
- computing matrix elements easily,
- a low need of memory and a fast access of states.

Within second quantization states are naturally formulated in terms of creation operators acting on the vacuum state $|0\rangle$

$$\left(c_{1\uparrow}^\dagger\right)^{n_{1\uparrow}} \left(c_{2\uparrow}^\dagger\right)^{n_{2\uparrow}} \cdots \left(c_{L\uparrow}^\dagger\right)^{n_{L\uparrow}} \left(c_{1\downarrow}^\dagger\right)^{n_{1\downarrow}} \left(c_{2\downarrow}^\dagger\right)^{n_{2\downarrow}} \cdots \left(c_{L\downarrow}^\dagger\right)^{n_{L\downarrow}} |0\rangle, \quad (3.5)$$

with the occupation number $n_{i\sigma} = \{0, 1\}$. The order of the creation operators is a matter of convention, but important to retain. Specifying the states by the occupation number leads to a binary number for each state, e.g. for the state

$$c_{1\uparrow}^\dagger c_{4\uparrow}^\dagger c_{1\downarrow}^\dagger c_{3\downarrow}^\dagger |0\rangle = |1, 0, 0, 1; 1, 0, 1, 0\rangle. \quad (3.6)$$

This 8-bit binary number can be stored as an unsigned integer, which would be 154 for the example above. Therefore, the entire many-body basis can be cast into a vector of unsigned integer numbers.

The Hilbert space of an impurity system with L sites consists of $d_{\text{full}} = 2^L \cdot 2^L$ basis states in total, but this number can be significantly reduced by exploiting symmetries and quantum numbers.

The AIM Hamiltonian 3.1 conserves the total spin S_z as well as the particle numbers N_{\uparrow} and N_{\downarrow} ¹⁷. This means that the diagonalization can be done separately for each spin and particle sector, reducing the size of the effective Hilbert space to

$$d_{\text{sector}} = \frac{L!}{N_{\uparrow}!(L - N_{\uparrow})!} \frac{L!}{N_{\downarrow}!(L - N_{\downarrow})!} \quad (3.7)$$

For the largest sector ($N_{\uparrow} = N_{\downarrow} = L/2$) equation 3.7 translates into $d_{\text{sector}L/2} = (L!/(L/2)!)^2$, which is still growing exponentially like $4^L/L$ for large L . Nevertheless, the exploitation of those symmetries decreases the complexity of the problem and can make the key difference to be able to treat a system of a certain size.

The second simplification is based on the observation that it is not necessary to store each individual state. It is enough to keep all possible up and down states in two *separate* vectors and bearing in mind that the full basis is obtained by pairing every individual up state with each down state. This reduces the number of stored states to $d_{\text{stored}} = 2 \cdot \sqrt{d_{\text{sector}}}$. This concept is very advantageous when constructing the Hamiltonian matrix from the basis states.

Within one sector the number of up spins N_{\uparrow} (down spins N_{\downarrow}) is fixed and thus the up (down) basis is nothing else but all possible permutation of N_{\uparrow} (N_{\downarrow}) electrons on L sites. Probably the most efficient way to generate all those permutation is by using a code known as ITEM #175 from the legendary technical HAKMEM memo [59, 60]. This little piece of code which given an integer, computes the next highest integer with the same number of one bits can be applied iteratively to generate all subsets with a given number of ones (code is listed in appendix C). By construction, the resulting basis is automatically ordered in an ascending way.

The next step after generating the basis states is to build the full many-body Hamiltonian matrix. This matrix is usually extremely sparse and the number of non-zero elements is typically of $O(N)$ rather than $O(N^2)$. This can be used to save memory by storing only the individual entries and its corresponding row and column indices. Moreover, a spares representation allows speeding up matrix-vector multiplications occurring in exact diagonalization schemes.

Calculating the matrix elements $\langle m | H_{AIM}^{ED} | n \rangle$ simply boils down to acting with each term of the Hamiltonian on every state of the basis: $H_{AIM}^{ED} | n \rangle$. The position of the initial state in the basis corresponds to the row number and the position of the resulting

¹⁷Those operators commute with the Hamiltonian and are therefore conserved quantities.

state to the column number of a matrix element. Due to the fact that the basis is already sorted, the search for the position of the resulting state can be done most efficiently with a bisection algorithm.

The single-particle (hopping) terms destroy a spin on site i and create the same spin on site j , but always act only on up or down states. For each individual hopping term the procedure is:

1. Loop over all up states and check if hopping is permitted (flip bit i from 1 to 0 and bit j from 0 to 1).
2. If yes:
 - a) Search resulting up state within all up states to obtain its position.
 - b) Calculate fermionic sign ξ by counting the electrons between sites i and j .
 - c) Add the element $\xi \cdot t_{ij}$ to the sparse matrix with the correct row and column indices taking into account all down states belonging to the up state.
3. Do the same for all down states.

In C/C++ all the mentioned steps can be implemented very efficiently by using logical bit operators, e.g. flipping bit i is basically a bit-wise XOR applied to the state and a bit pattern having a one shifted i times to the left.

The advantages of separating up and down states gets evident at this point, because we only have to act with the Hamiltonian on d_{store} states and *not* d_{sector} states. Furthermore, the performance of the bisection search is of order $\log_2(d)$ and therefore about a factor of two faster when searching only the up/down states.

Dealing with the interaction and on-site terms is in many cases easier. For instance, in the single-orbital model only diagonal elements occur and thus the evaluation of those terms requires one loop over the whole basis. For each state the interaction contribution is obtained by applying a bitwise AND to the up and down parts. The on-site energy for doubly occupied sites is just added to the interaction term and the single occupied sites are determined with a bitwise XOR operation.

For the interaction part of the multi-orbital model, i.e. the local part of Hamiltonian 2.3, we distinguish between terms with the same spin of all four creation/annihilation operators and terms with two different spins.

For the same spin ($\sigma = \sigma'$) again one loop over all up and down states is used, where the condition of a possible creation/annihilation is checked and if applicable the according bits are flipped. Caution is necessary for the determination of the fermionic sign, because this time it depends not only on the bits between two sites, but also on the indices of the operators.

For different spins ($\sigma \neq \sigma'$) we commute the operators

$$c_{m\sigma}^\dagger c_{m'\sigma'}^\dagger c_{m''\sigma'} c_{m''\sigma} = c_{m'\sigma'}^\dagger c_{m''\sigma'} c_{m\sigma}^\dagger c_{m''\sigma}. \quad (3.8)$$

This term is now evaluated by acting with the first two operators on all spin σ' states and with the second two operators on all spin σ states while storing pairs of initial and resulting states. Consequently, the matrix elements result from all combinations of up and down states and need to be inserted correctly into the Hamiltonian matrix.

3.1.3. Diagonalizing the Hamiltonian – ground state

In this work the LAPACK [61, 62] routine *ZHEEV* is used to compute the eigensystem of a Hamiltonian H ¹⁸. This double precision routine diagonalizes an (optionally) complex but hermitian matrix by first reducing it to a tridiagonal form with unitary similarity transformations, and then applying the QR algorithm to compute the eigenvectors and eigenvalues of the tridiagonal matrix. Such a full diagonalization scheme is only feasible for small impurity systems ($L \leq 6$).

A different approach is the Lanczos algorithm [63], which is a standard scheme from numerical mathematics to obtain a few extremal eigenvalues and eigenvectors. If the system is prohibitively large for full diagonalization, the iterative Lanczos solver provides a fast and reliable method to determine the ground state and its energy. The following discussion of the Lanczos algorithm is based on the references [64, 65].

The starting point of the Lanczos algorithm is a vector which has overlap with the ground state and is typically chosen as a random normalized vector $|\phi_0\rangle$. Applying the Hamiltonian H n -times iteratively on the initial vector spans the Krylov subspace

$$\mathcal{K}_n(H, |\phi_0\rangle) = \text{span} [|\phi_0\rangle, H|\phi_0\rangle, H^2|\phi_0\rangle, H^3|\phi_0\rangle, \dots, H^n|\phi_0\rangle]. \quad (3.9)$$

The generated Krylov vectors are not orthogonal a priori, but have to be orthogonalized with the Gram-Schmidt scheme. This leads to the recursive relation

$$\begin{aligned} |\overline{\phi_{n+1}}\rangle &= H|\phi_n\rangle - \epsilon_n|\phi_n\rangle - \beta_n|\phi_{n-1}\rangle \\ \text{with } \epsilon_n &= \langle\phi_n|H|\phi_n\rangle \\ \beta_n &= \langle\phi_{n-1}|H|\phi_n\rangle = \|\overline{\phi_n}\| \\ |\phi_{n+1}\rangle &= \frac{|\overline{\phi_{n+1}}\rangle}{\|\overline{\phi_{n+1}}\|}, \end{aligned} \quad (3.10)$$

¹⁸From here on the labels of H are omitted, because the presented methods are not subject to a specific Hamiltonian.

which is at the core of the Lanczos method.¹⁹ Directly from those equations we can obtain the matrix

$$\begin{aligned} V_{nm} &= \langle \phi_n | H | \phi_m \rangle = \langle \phi_n | \overline{\phi_{m+1}} \rangle + \epsilon_m \langle \phi_n | \phi_m \rangle + \beta_m \langle \phi_n | \phi_{m-1} \rangle \\ &= \beta_n \delta_{n,m+1} + \epsilon_m \delta_{n,m} + \beta_m \delta_{n,m-1}. \end{aligned} \quad (3.11)$$

Thus, the projection V of the Hamiltonian onto the Krylov subspace yields a tridiagonal matrix

$$V = \begin{pmatrix} \epsilon_0 & \beta_1 & 0 & & & & \\ \beta_1 & \epsilon_1 & \beta_2 & 0 & & & \\ 0 & \beta_2 & \epsilon_2 & \beta_3 & \ddots & & \\ & 0 & \beta_3 & \epsilon_3 & \ddots & 0 & \\ & & \ddots & \ddots & \ddots & \beta_n & \\ & & & 0 & \beta_n & \epsilon_n & \end{pmatrix} \quad (3.12)$$

The eigenvalues of this matrix are an approximation for the eigenvalues of H . Of course, the diagonalization of the matrix V has to be carried out, but this is numerically less demanding since its size is typically of $O(100)$. To ensure convergence to the real ground state energy, the algorithm is iterated until the relative change in the ground state energy, which is the lowest eigenvalue of V , drops below a small tolerance tol . Additionally, the procedure needs to be stopped if the Krylov subspace for a given start vector $|\phi_0\rangle$ is exhausted, indicated by

$$\beta_n = \sqrt{\langle \phi_n | \overline{\phi_n} \rangle} < tol. \quad (3.13)$$

To make the algorithm more efficient, the diagonalization of V is only performed in an appropriate interval N_D of iterations. The eigenvectors c^γ of V correspond to the projection of the H eigenvectors onto the Krylov subspace. At the same time, these are nothing else but the expansion coefficients of the approximate eigenvectors $|\psi_\gamma\rangle$

$$|\psi_\gamma\rangle = \sum_n c_n^\gamma |\phi_n\rangle \quad \text{with} \quad c_n^\gamma = \langle \phi_n | \psi_\gamma \rangle. \quad (3.14)$$

As implied by equation 3.10, it is only necessary to keep the last three Krylov vectors ($|\phi_{n-2}\rangle$, $|\phi_{n-1}\rangle$ and $|\phi_n\rangle$) in memory, but this prohibits evaluating equation 3.14 for the eigenvectors. In practice, the whole algorithm can be executed a second time to iteratively build the approximate eigenvectors $|\psi_\gamma\rangle$ from the Krylov vectors $|\phi_n\rangle$.

The Lanczos scheme is both simple and efficient, because for each iteration only one vector-matrix multiplication contributes to the overall computational costs. Unfortunately, the algorithm turns out to be sensitive to numerical instabilities as soon as

¹⁹The overlines symbolize quantities which are not normalized.

one eigenvector is converged. Then orthogonality of the Krylov vectors is lost, which results in unphysical degenerations and eigenvalues appearing multiple times. An explicit reorthogonalization of the Krylov basis can avoid such ghost states, but again requires to keep all previous Krylov vectors in memory. If the systems itself is not prone to degenerations and interest is only paid to the ground state and its energy, the Lanczos algorithm can be used without the cumbersome reorthogonalization

3.1.4. Band Lanczos algorithm – Green’s function

An extension to the standard Lanczos scheme, commonly known as band Lanczos algorithm [64, 66], is also applicable to systems with degenerate ground states. At the same time, the band Lanczos algorithm allows for a direct calculation of the Green’s function. Instead of a single start vector the band Lanczos scheme is initialized with a block of p vectors

$$[|\phi_1\rangle, |\phi_2\rangle, \dots, |\phi_p\rangle] \quad (3.15)$$

Iteratively applying H to the *multiple* starting vectors spans the Krylov subspace

$$\begin{aligned} \mathcal{K}_n(H, [|\phi_i\rangle]) = \text{span} [& |\phi_1\rangle, H|\phi_1\rangle, H^2|\phi_1\rangle, \dots, H^n|\phi_1\rangle, \\ & |\phi_2\rangle, H|\phi_2\rangle, H^2|\phi_2\rangle, \dots, H^n|\phi_2\rangle, \\ & \vdots \\ & |\phi_p\rangle, H|\phi_p\rangle, H^2|\phi_p\rangle, \dots, H^n|\phi_p\rangle]. \end{aligned} \quad (3.16)$$

In contrast to the standard Lanczos algorithm, it is not possible to use the termination condition 3.13, which indicates linear dependence of the current Krylov vector on the previous ones, for the multiple band Lanczos starting vectors. In the case $p > 1$, the occurrence of the first linearly dependent vector in the Krylov subspace 3.16 does *not* mean that the entire block Krylov sequence is exhausted, but rather that the regarding vector and all its following H -multiples do not provide any new information. Therefore, the corresponding vector should be detected and deleted from the Krylov subspace. This reoccurring process, referred to as exact deflation, reduces the p Krylov vectors to p_c and finally to $p_c = 0$. It is impossible to distinguish numerically between exactly and nearly linear dependent vectors. Thus, a vector has to be deflated if its norm is smaller than a given tolerance, like it was defined in the condition 3.13.

Orthogonality has to be explicitly ensured only for $2p_c + 1$ consecutive band Lanczos vectors and if deflation occurs against $p - p_c$ earlier vectors. The deflation results in a banded matrix V , where each deflation reduces the bandwidth by two. Note that a deflation of nearly independent vectors leads to non-zero entries in the corresponding rows and columns of V .

As a concrete example consider $p = 3$ start vectors. Deflations are occurring after 5 and 8 iterations would yield the V -matrix

$$V = \begin{pmatrix} * & * & * & * & & & & & & \\ * & * & * & * & d & d & d & d & d & \\ * & * & * & * & * & & & & & \\ * & * & * & * & * & * & & & & \\ & d & * & * & * & * & * & & & \\ & d & & * & * & * & * & d & d & \\ & d & & & * & * & * & * & & \\ & d & & & & d & * & * & * & \\ & d & & & & d & & * & * & \end{pmatrix}. \quad (3.17)$$

The stars (*) denote potential non-zero entries within the banded part and the d 's stand for possible non-zero entries due to deflations. The algorithm stops – like in the standard Lanczos scheme – if the eigenvalues of V are converged, or naturally if the block Krylov subspace is exhausted after p deflations.

Now we turn to the evaluation of the full fermionic Green's function $g_{\nu\nu'}(z)$ for temperature $T = 0$, which is given by [27, 28, 67]

$$g_{\nu\nu'}(z) = \sum_{\alpha} \left[\langle \psi_0^{\alpha} | c_{\nu} \frac{1}{z - (H - E_0)} c_{\nu'}^{\dagger} | \psi_0^{\alpha} \rangle + \langle \psi_0^{\alpha} | c_{\nu'}^{\dagger} \frac{1}{z + (H - E_0)} c_{\nu} | \psi_0^{\alpha} \rangle \right]. \quad (3.18)$$

The vector $|\psi_0^{\alpha}\rangle$ is the ground state and the summation over α takes a possibly degeneration of $|\psi_0^{\alpha}\rangle$ into account. The first term in this representation corresponds to the $N + 1$ particle sector, because the creation operator is applied to a N particle ground state: $c_{\nu'}^{\dagger} |\psi_0^{\alpha}\rangle$. Likewise, the second term describes the annihilation of a particle from the ground state leading to a $N - 1$ particle state: $c_{\nu} |\psi_0^{\alpha}\rangle$. Inserting the identity $\mathbb{1} = \sum_m |\psi_m\rangle \langle \psi_m|$ into both terms of equation 3.18 results in the Lehmann representation

$$g_{\nu\nu'}(z) = \sum_{\alpha} \left[\sum_n \frac{\langle \psi_0^{\alpha} | c_{\nu} | \psi_n \rangle \langle \psi_n | c_{\nu'}^{\dagger} | \psi_0^{\alpha} \rangle}{z - (E_n - E_0)} + \sum_m \frac{\langle \psi_0^{\alpha} | c_{\nu'}^{\dagger} | \psi_m \rangle \langle \psi_m | c_{\nu} | \psi_0^{\alpha} \rangle}{z + (E_m - E_0)} \right]. \quad (3.19)$$

To evaluate the Green's function in this form only the ground state, its energy and the full information of the $N \pm 1$ particle sectors are required. Fortunately, the band Lanczos algorithm provides all necessary ingredients:

1. The ground state $|\psi_0^{\alpha}\rangle$ and its energy E_0 are calculated with the standard Lanczos scheme or in case of a likely degeneracy with the band Lanczos algorithm.
2. For each ground state the band Lanczos algorithm is executed two times.

Once with the start vectors²⁰

$$|\tilde{\phi}_1\rangle = c_1^\dagger |\psi_0\rangle, |\tilde{\phi}_2\rangle = c_2^\dagger |\psi_0\rangle, \dots, |\tilde{\phi}_L\rangle = c_L^\dagger |\psi_0\rangle \quad (3.20)$$

for the $N + 1$ particle sector and once with

$$|\tilde{\phi}_1\rangle = c_1 |\psi_0\rangle, |\tilde{\phi}_2\rangle = c_2 |\psi_0\rangle, \dots, |\tilde{\phi}_L\rangle = c_L |\psi_0\rangle \quad (3.21)$$

for the $N - 1$ particle sector. Note that the initial vectors are orthonormalized against each other a la Gram-Schmidt in the first steps of the algorithm

$$|\phi_i\rangle = \frac{1}{N_i} \left(|\tilde{\phi}_i\rangle - \sum_{k=1}^{i-1} |\phi_k\rangle \langle \phi_k | \tilde{\phi}_i \rangle \right). \quad (3.22)$$

3. For the $N + 1$ particle sector the eigenvectors of V are the projected eigenvectors of H onto the Krylov subspace $\langle \phi_i | \psi_n \rangle$. As the starting vectors are part of the Krylov subspace, those also contain $\langle \phi_{1\dots L} | \psi_n \rangle$. To obtain $\langle \tilde{\phi}_{1\dots L} | \psi_n \rangle = \langle \psi_0 | c_{1\dots L} | \psi_n \rangle$ we act with $\langle \psi_n |$ from the left on equation 3.22 and rearrange it to

$$\langle \psi_n | \tilde{\phi}_i \rangle = N_i \langle \psi_n | \phi_i \rangle + \sum_{k=1}^{i-1} \langle \psi_n | \phi_k \rangle \langle \phi_k | \tilde{\phi}_i \rangle \quad \text{for } i = 1 \dots L. \quad (3.23)$$

These and their complex conjugates are exactly the matrix elements required by equation 3.19. The same argument holds also for the $N - 1$ particle sector.

4. The energies E_n and E_m correspond to the approximate eigenvalues of the banded matrix V .

In practice, the occurring inner products in the Lehmann representation 3.19 are cast into a so-called Q -matrix, allowing to deal with the Green's function in a z -independent form. Further details on the Q -matrix formalism are discussed in appendix D.

3.2. Cluster perturbation theory

Cluster perturbation theory (CPT) is an approximation scheme for calculating the Green's function of a strongly correlated system [16, 17, 68] and originates from a leading order cluster extension of strong-coupling perturbation theory [16, 69]. CPT is most often applied to translationally invariant systems (e.g. Hubbard model). The key steps of every CPT calculation are:

²⁰We omit the orbital and the spin index as well as the index α for the sake of simplicity.

1. **Divide the original lattice into a super-lattice of identical clusters.**

These clusters have to be disconnected and of finite size L (see figure 3.3). In terms of the Hamiltonian the system is rewritten as

$$H = H' + T, \quad (3.24)$$

where H' is the Hamiltonian describing all clusters, but leaving out the hopping terms between clusters. The matrix T contains exactly those omitted hoppings.

2. **Calculate the cluster Green's function $G'(z)$.**

This can be done with ED as discussed in the previous section 3.1.

3. **Treat inter-cluster hoppings in strong-coupling perturbation theory.**

It can be shown that the leading order perturbation theory yields for the Green's function the equation

$$\mathbf{G}^{-1}(z) = \mathbf{G}'^{-1}(z) - \mathbf{T}. \quad (3.25)$$

A heuristic justification of this equation is given in appendix E. Applying a partial Fourier transformation on the super-lattice level simplifies this equation to

$$G_{a,b}^{-1}(\mathbf{k}, z) = G'_{a,b}{}^{-1}(z) - T_{a,b}(\mathbf{k}), \quad (3.26)$$

where the appearing matrices are only of size $L \times L$.

4. **Restore translational invariance for the lattice Green's function.**

The Green's function $G_{a,b}(\mathbf{k}, z)$ is only periodical over the cluster super-lattice, but the original translational symmetry is still broken. The periodization procedure for the full translationally invariant Green's function reads

$$G(\mathbf{k}, z) = \frac{1}{N_c} \sum_{r_a, r_b} e^{i\mathbf{k}(r_a - r_b)} G_{a,b}(\mathbf{k}, z). \quad (3.27)$$

A detailed justification for this periodization can be found in [16] or [68].

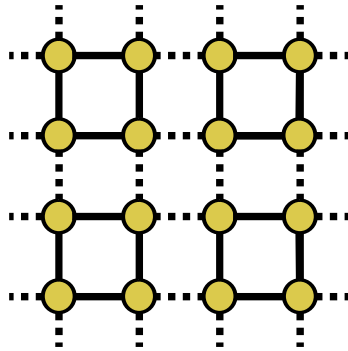


Figure 3.3.: Tiling of a translationally invariant system into finite clusters of size $L = 4$. The hopping between clusters is indicated by the dashed lines.

The CPT result can be controlled by increasing the cluster size, whereby in the limit $L \rightarrow \infty$ the exact solution is recovered. Furthermore, CPT becomes an exact theory in both the atomic-limit and the non-interacting $U = 0$ limit.

3.2.1. CPT for the impurity model

Now we turn to the – for this work relevant – case of a non-translationally invariant system, i.e. the AIM. Recently, the AIM was investigated by means of CPT, and its extended variational version known as variational cluster approach (VCA) [19, 20]. For a non-translationally invariant system the division into clusters is simplified to separating the system into (see figure 3.4)

- a cluster of size L including the interacting impurity site and
- a *semi-infinite* chain of non-interacting sites.

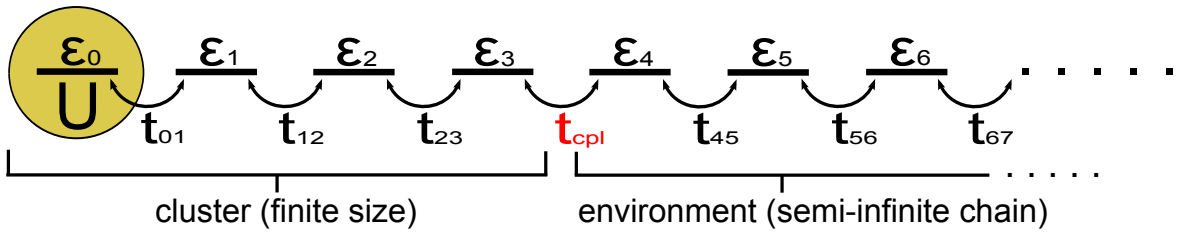


Figure 3.4.: Division of the impurity model into a cluster of size $L = 4$ containing the interacting impurity site and a semi-infinite non-interacting chain. The coupling between these two systems is treated within CPT.

This separation into a cluster and an environment makes it possible to calculate the Green's function of both parts individually. Due to the missing translation invariance, the Green's function of the total system is then already given by equation 3.25, i.e.

$$g^{-1}(z) = \begin{pmatrix} g_{cl}(z) & 0 \\ 0 & g_{env}(z) \end{pmatrix}^{-1} - \begin{pmatrix} & \\ t_{cpl} & t_{cpl} \end{pmatrix} \quad (3.28)$$

Here, the first matrix is two-block diagonal with the Green's function of the cluster $g_{cl}(z)$ in the first block and the Green's function of the environment $g_{env}(z)$ in the second block. The matrix T contains only the coupling between those two systems. In the specific case of a non-interacting environment, the knowledge of the Green's

function on the *first* environment site is sufficient to evaluate the full CPT Green's function $g(z)$. The desired Green's function of the coupled environment can be easily calculated, e.g. with a continuous fraction expansion of the bath chain. To obtain the cluster Green's function ED is the method of choice.

As we still wish to obtain the parameters of the impurity system with the cost function 3.3, one possibility would be to couple a few extra bath sites to the L -site cluster [70]. However, we take a slightly different approach and parametrize our impurity system as a cluster coupled to a semi-infinite chain with *constant* on-site energies ϵ_∞ and hoppings t_∞ .²¹ This choice is based on the observation that the parameters for sites far away from the impurity indeed converge to a constant value if a system with sufficiently many bath sites is used. In this bath representation the remaining parameters to determine are the hoppings and on-site energies within the cluster, the hopping (coupling) between the cluster and the chain as well as *one* on-site energy and *one* hopping for the whole semi-infinite chain. Of course, our bath representation strongly restricts the bath, but it offers a few advantages:

- Only three additional parameters influence the minimization of χ .
- The bath is infinite and therefore the bath Green's function is continuous.²²
- The Green's function of the environment can be expressed analytically and calculated in a fast way (see equation 3.29 below).
- It is well defined in the sense that it does not leave the freedom of choosing the total number of bath sites.

The expression for the Green's function $g_{env}(z)$ of a semi-infinite tight-binding chain with hoppings t_∞ and on-site energies ϵ_∞ reads [71]

$$g_{env,ij}(z) = f_{0,i-j}(z) - f_{0,i+j}(z), \quad \text{whereby}$$

$$f_{i,j}(z) = \frac{-i \operatorname{sign}(\Im[z])}{\sqrt{4|t_\infty|^2 - (z - \epsilon_\infty)^2}} \left(-\frac{z - \epsilon_\infty}{2|t_\infty|} + i \operatorname{sign}(\Im[z]) \sqrt{1 - \left(\frac{z - \epsilon_\infty}{2|t_\infty|}\right)^2} \right)^{|i-j|}. \quad (3.29)$$

Notably, the DOS on site 1 is given by

$$\rho_{env,11}(\omega) = -\frac{1}{\pi} \lim_{\eta \rightarrow 0} \Im [g_{env,11}(\omega + i\eta)] = \Re \left[\frac{\sqrt{4t_\infty^2 - (\omega - \epsilon_\infty)^2}}{2\pi t_\infty^2} \right], \quad (3.30)$$

which has a semicircular shape and a half-bandwidth of $2t_\infty$.

²¹Of course, other representation of the bath are possible or might be better justified.

²²Strictly speaking, this is only true within the bandwidth of the environment.

It turns out that the CPT approach offers a few benefits, but at same time suffers from some limitations. First, we shall have a look at the self-energy $\Sigma(z)$. Within CPT the full and the free Green's functions are given by

$$g^{-1}(z) = \tilde{g}^{-1}(z) - T \quad \text{and} \quad g_0^{-1}(z) = \tilde{g}_0^{-1}(z) - T, \quad (3.31)$$

where $\tilde{g}(z)$ and $\tilde{g}_0^{-1}(z)$ are devoted to the Green's functions of the separated systems. Consequently, it follows for the self-energy²³

$$\begin{aligned} \Sigma(z) &= g_0^{-1}(z) - g^{-1}(z) = \tilde{g}_0^{-1}(z) - T - (\tilde{g}^{-1}(z) - T) \\ &= \tilde{g}_0^{-1}(z) - \tilde{g}^{-1}(z) \stackrel{*}{=} g_{0cl}^{-1}(z) - g_{cl}^{-1}(z) = \Sigma_{cl}(z). \end{aligned} \quad (3.32)$$

This reflects the fact that CPT approximates the self-energy of the whole system $\Sigma(z)$ by the cluster self-energy $\Sigma_{cl}(z)$ (see also appendix E). Correlations within the cluster are fully taken into account, but all correlations going beyond are neglected. Although the used AIM is of infinite size, the self-energy itself is just the self-energy of a finite system and thus a *discrete* quantity. This is especially severe in terms of DMFT, because the self-energy is the only quantity of interest for the lattice system (see the DMFT cycle in figure 2.1).

It should be pointed out that the knowledge of the cluster parameters *only* is sufficient to calculate the self-energy $\Sigma(z)$. CPT can be seen as a truncation of the impurity system at a certain site, whereby all parameters of the system were determined by minimizing the cost function 3.3, but with the non-interacting Green's function $g_0^{-1}(z)$ of the *full* system. Nevertheless, the coupled chain will certainly have a strong influence on the cluster parameters through the minimization of χ and those parameters will therefore differ from that determined by ED.

In contrast to ED, where an artificial L -site system is used as replacement for the full impurity model, CPT works directly with the full infinite system. Lifting our restriction on the bath from above would correspond to $\chi = 0$, because then $\mathcal{G}_0(z)$ can be exactly represented by the infinite bath. On the other hand, ED will always show a rather high χ due to fitting a collection of broadened delta peaks. Of course, $\chi = 0$ does not hold for our choice of the bath parametrization, but still χ is significantly reduced in comparison to ED. Additionally, the DMFT self-consistency condition 2.16, which can never be fulfilled within ED, is fulfilled much better when using CPT as impurity solver as we will show below in section 4.4.

²³In the step marked with * the size of the matrix $\Sigma(z)$ is reduced to $L \times L$, because all entries outside cancel and do not contribute to the self-energy.

3.2.2. Improving on the CPT approach

Undoubtedly, the outlined CPT procedure will suffer from a severe error introduced by approximating the self-energy of the full impurity system with the self-energy of the cluster only. In chapter 4 it will turn out that the CPT results are indeed not satisfying. One reason is simply that CPT is only expected to be reliable as long as the cluster-environment coupling t_{cpl} remains small. Consequently, C. Weber et al. [70] suggested to add a Lagrange term to the cost function 3.3

$$\tilde{\chi} = \chi + \tilde{\lambda} t_{cpl}^2. \quad (3.33)$$

The introduced penalty term directly aims at keeping the coupling t_{cpl} small. However, the added term is somewhat arbitrary, not just its structure, but also the choice of the weight $\tilde{\lambda}$. For example take a small $\tilde{\lambda}$, then the influence of the penalty is negligible and we get again the unrestricted CPT result. On the other hand, for a huge penalty term $\tilde{\lambda} \gg \chi$ the coupling is forced to zero. This case equals a decoupling of the bath and leaves us with the bare ED cost function. Although it seems natural to choose $\tilde{\lambda}$ according to the magnitude of χ , the particular choice will influence the result. As this approach is only ad-hoc and phenomenological, a better founded method will be discussed in the remainder of this chapter. We start by defining a slightly different cost function

$$\chi_{CPT\lambda} = (1 - \lambda) \cdot \chi_{CL} + \lambda \cdot \chi_{CPT}. \quad (3.34)$$

χ_{CL} is the cost function 3.3 evaluated with the non-interacting Green's function of the cluster $g_{0cl}(z)$. This means that all bath parameters \vec{a} outside of the cluster are set to zero. Accordingly, χ_{CPT} is the cost function obtained with the non-interacting Green's function of the full impurity system $g_0(z)$, where our bath parametrization, as discussed in the previous section, is used. The cost function $\chi_{CPT\lambda}$ can be considered as an interpolation between the ED and the CPT solution, because those limits are restored for

$$\begin{aligned} \lambda = 0 & : \rightarrow \text{ED (decoupling of the environment)} \\ \lambda = 1 & : \rightarrow \text{CPT (full coupling of the environment)} \\ 0 < \lambda < 1 & : \rightarrow \text{CPT}\lambda \text{ (interpolation)}. \end{aligned} \quad (3.35)$$

This new definition of the cost function turns out to be more stable and reliable than the cost function 3.33, because it does not only restrict a certain parameter but acts on the whole system in a more general way.

In figure 3.5 the values for $\chi_{CPT\lambda}$ and its individual contributions are depicted. The calculations were performed on the half-filled Bethe lattice²⁴ for a cluster of size $L = 6$

²⁴For details on the Bethe lattice and the settings of the DMFT calculations see chapter 4.

and interaction strength $U/D = 0.5$. For each λ a full DMFT calculation was carried out and only the converged values for $\chi_{CPT\lambda}$ are shown. The cost function $\chi_{CPT\lambda=0} = 2.40$ for ED is in this example about 50 times larger than the resulting cost function $\chi_{CPT\lambda=1} = 0.05$ for CPT.

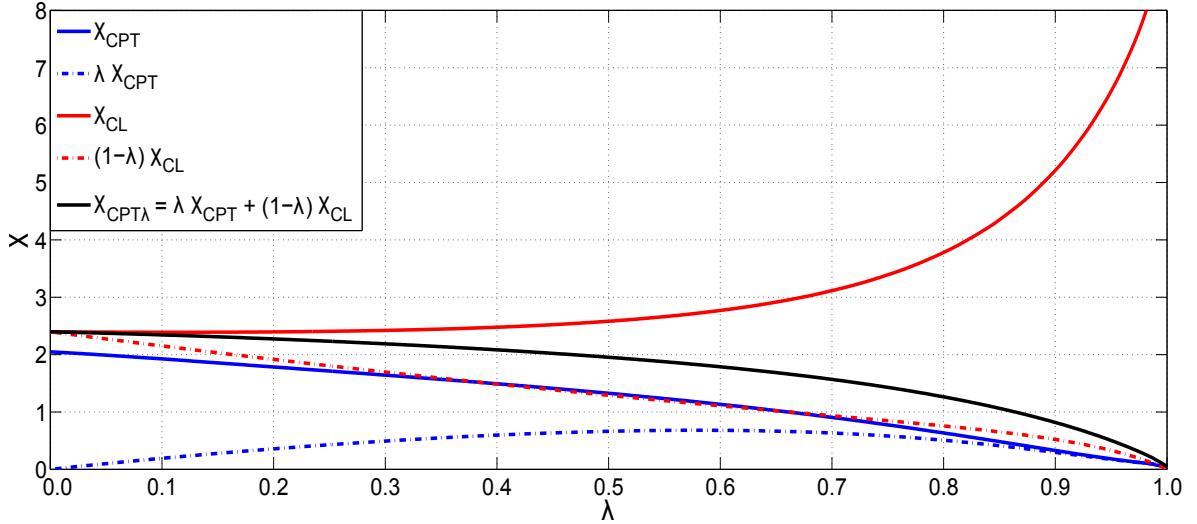


Figure 3.5.: Cost function $\chi_{CPT\lambda}$ and its individual contributions according to equation 3.34 as a function of λ . Calculations were performed on the half-filled Bethe Lattice for a cluster of size $L = 6$ and $U/D = 0.5$.

It can be seen nicely that even for a small λ the contribution coming from χ_{CPT} is smaller than that from the bare cluster χ_{ED} . Surprisingly, the latter exhibits a vast growth with increasing λ , which is made possible by the decreasing prefactor $(1 - \lambda)$. In that case the representation of the bath Green's function $\mathcal{G}_0(z)$ by the cluster Green's function $g_{0cl}(z)$ is extremely poor. Since the self-energy is determined by the cluster quantities alone, this reflects the key reason for the poor performance of plain CPT, which we will encounter in chapter 4.

3.2.3. Determination of the parameter λ

In this section we aim at determining the required parameter λ in *post-processing* the converged DMFT results for the whole λ -range.²⁵ For each λ between zero and one (with a step size of $\Delta\lambda = 0.0025$) and for the cluster sizes of $L = 2, 4, 6$ and 8 a full DMFT calculation was carried out. The open task in this section is to choose the calculation, i.e. the λ , which provides the 'best' result.

²⁵The reason for considering the converged results and not, e.g., the results after one iteration is motivated by the desire to be independent of the initial starting point.

Unfortunately, we still lack of a suitable way to determine the 'best' λ value, because regarding only the cost function would lead to the wrong conclusion $\lambda = 1$. Therefore, we introduce a second figure of merit to justify a certain choice of λ . Without any doubt, the error in the self-energy $\Sigma(z)$ constitutes the most important measure for the correctness of the impurity parameters. To quantify its error we define the difference

$$\Delta\Sigma(\lambda) = \int dz |\Sigma_{EX}(z, \lambda) - \Sigma_{CL}(z, \lambda)|, \quad (3.36)$$

which compares the self-energy of the cluster $\Sigma_{CL}(z, \lambda)$ to the 'exact' self-energy of the actual impurity system $\Sigma_{EX}(z, \lambda)$.

In figure 3.6 hypothetical behaviors of $\Delta\Sigma(\lambda)$ as a function of λ are sketched. The case in the middle would confirm the conclusion $\lambda = 1$, like drawn from the cost function alone. On the other hand, the right case declares $\lambda = 0$ and selects the highest point of the cost function, which would reduce the whole method to ad absurdum. The left case – which is the desired one – provides a minimum of $\Delta\Sigma(\lambda)$ somewhere in between the two extremes and gives at the same time an optimal point for λ .

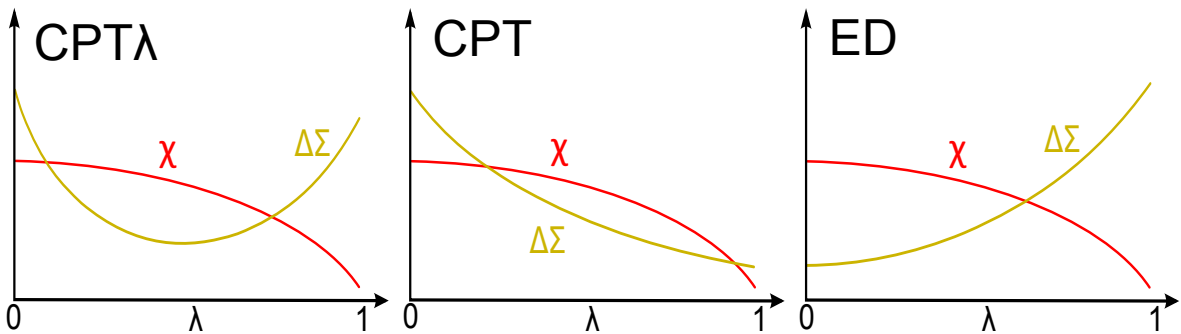


Figure 3.6.: Hypothetical behaviors of $\Delta\Sigma(\lambda)$. The left case would justify the *CPT* λ approach and provide an optimal value for λ .

Of course, it is not possible to calculate the 'exact' self-energy, but second order perturbation theory in U offers a simple equation to obtain an approximation directly from the non-interacting bath Green's function. For half-filling the second order contribution to the self-energy is given by²⁶

$$\Sigma(i\omega_n) \simeq U^2 \int_0^\beta d\tau \mathcal{G}_0^2(\tau) \mathcal{G}_0(-\tau) e^{i\omega_n \tau} \quad (3.37)$$

²⁶The first order contribution is constant ($-U/2$) and can be absorbed into the chemical potential μ .

This approximation is commonly known from the iterative perturbation theory (IPT) [7, 33, 72], where equation 3.37 is basically used as impurity solver. It should be stressed that we are *not* using IPT as impurity solver in the DMFT cycle, because the original IPT is only applicable at half-filling. Equation 3.37 is *exclusively* utilized as a post-processing tool to determine the optimal λ .

Equation 3.37 needs to be evaluated twice to obtain a $\Delta\Sigma(\lambda)$. Once with the full bath Green's function $\mathcal{G}_0(i\omega_n, \lambda)$ to obtain the – within second order perturbation theory – 'exact' $\Sigma_{PT}(i\omega_n, \lambda)$ and once with the Green's function of the cluster $g_{0cl}(i\omega_n, \lambda)$ only, which yields $\Sigma_{CLPT}(i\omega_n, \lambda)$. If we assume that the error introduced by second order perturbation theory effects both $\Sigma_{PT}(i\omega_n, \lambda)$ and $\Sigma_{CLPT}(i\omega_n, \lambda)$ in a similar way, then

$$\Delta\Sigma(\lambda) = \int_0^\infty d\omega_n |\Sigma_{PT}(i\omega_n, \lambda) - \Sigma_{CLPT}(i\omega_n, \lambda)| \quad (3.38)$$

constitutes a suitable measure for the deviation, when approximating the whole system by a L -site cluster.

If we look again at equation 3.37, we realize that \mathcal{G}_0 is required in imaginary time τ . The transformation from the retarded Green's function to Matsubara frequencies can be easily done for the cluster, because with the parameters at hand we can evaluate the continuous fraction representation given by equation 3.4 with $z = i\omega_n$. In a second step, the non-interacting Matsubara Green's function $g_0(i\omega_n)$ needs to be Fourier transformed to imaginary time τ

$$g_0(\tau) = \frac{1}{\beta} \sum_{n=-\infty}^{\infty} g_0(i\omega_n) e^{-i\omega_n\tau}, \quad (3.39)$$

where it is important to take the asymptotic tail of $g_0(i\omega_n)$ correctly into account (see appendix A for details). The transformation of $\mathcal{G}_0(\omega)$, which is necessary for the 'exact' $\Sigma_{PT}(i\omega_n)$, can be done using the spectral theorem

$$\mathcal{G}_0(i\omega_n) = \int_{-\infty}^{\infty} d\omega \frac{A_0(\omega)}{i\omega_n - \omega} \quad \text{with} \quad A_0(\omega) = -\frac{1}{\pi} \Im[\mathcal{G}_0(\omega)], \quad (3.40)$$

or equivalently

$$\Re[\mathcal{G}_0(i\omega_n)] = - \int_{-\infty}^{\infty} d\omega \frac{\omega A_0(\omega)}{\omega_n^2 + \omega^2} \quad \text{and} \quad \Im[\mathcal{G}_0(i\omega_n)] = - \int_{-\infty}^{\infty} d\omega \frac{\omega_n A_0(\omega)}{\omega_n^2 + \omega^2}. \quad (3.41)$$

Again, the obtained $\mathcal{G}_0(i\omega_n)$ is Fourier transformed with equation 3.39.

The resulting $\mathcal{G}_0(\tau)$ and $g_0(\tau)$ are used to calculate $\Sigma_{PT}(i\omega_n, \lambda)$ and $\Sigma_{CLPT}(i\omega_n, \lambda)$.

In figure 3.7 the converged self-energies for a few selected λ values are shown. The calculations were performed on the half-filled Bethe lattice with $L = 2$ and $U/D = 0.5$. It is important to choose U/D not too small, because the self-energy vanishes for $U/D \rightarrow 0$, but also not too large to ensure the validity of second order perturbation theory in U . For each λ both self-energies were calculated from the converged Green's functions as outlined above.

Surprisingly, $\Sigma_{PT}(i\omega_n, \lambda)$ does exhibit only a weak dependence on the parameter λ . On the contrary, $\Sigma_{CLPT}(i\omega_n, \lambda)$ features a strong dependence, especially for $\lambda \geq 0.7$. Even if the imaginary part of $\Sigma_{CLPT}(i\omega_n, \lambda)$ for $\lambda = 0.85$ deviates from $\Sigma_{PT}(i\omega_n, \lambda)$, it shows the best accordance for both low and high Matsubara frequencies. Regarding the real part the best agreement is also found for $\lambda = 0.85$.

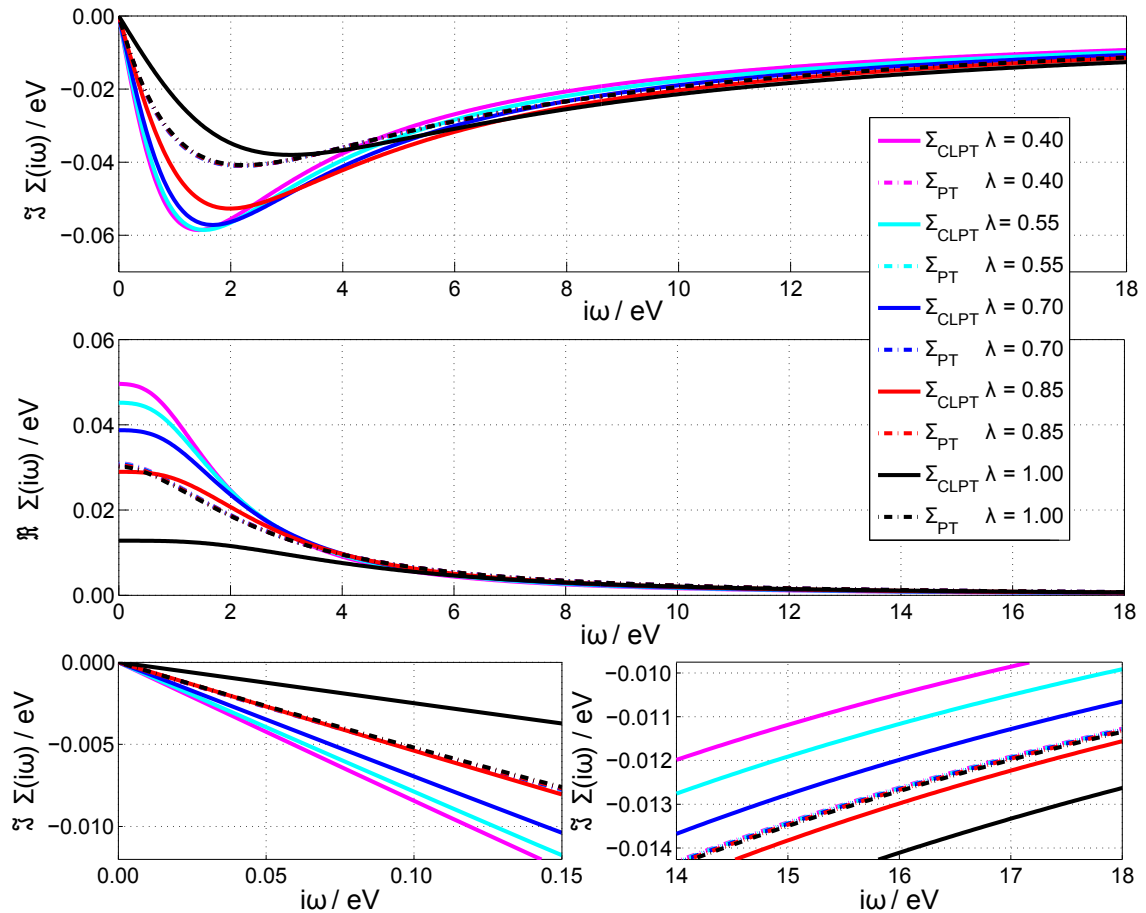


Figure 3.7.: Comparison of the imaginary (upper) and real (middle) part of $\Sigma_{PT}(i\omega_n, \lambda)$ and $\Sigma_{CLPT}(i\omega_n, \lambda)$ for different λ . The lower left (right) picture shows the low (high) frequency behavior of the imaginary part. All calculations were performed on the half-filled Bethe lattice for $U/D = 0.5$. For each λ the converged bath Green's functions were used to obtain the shown self-energies. Note that the results for $\Sigma_{PT}(i\omega_n, \lambda)$ almost cover each other.

It has to be noted that the real part of the self-energy should be zero for the half-filled Bethe lattice,²⁷ which is indeed the case if the self-energy is calculated via the Dyson equation like in the DMFT cycle. However, if we evaluate equation 3.37 with the converged $g_{0cl}(i\omega_n, \lambda)$ and $\mathcal{G}_0(i\omega_n, \lambda)$ this does not necessarily hold anymore.

The resulting $\Delta\Sigma(\lambda)$ for cluster sizes of $L = 2, 4, 6$ and 8 are presented in figure 3.8. All of them exhibit a distinct minimum around $\lambda \approx 0.8$, which gets slightly shift towards lower λ for increasing cluster sizes. The optimal λ values at those minima are listed in table 3.1. As expected $\Delta\Sigma(\lambda)$ decreases with the cluster sizes over the whole λ range and at the same time the shape is flattened leading to a much less distinctive minimum. Certainly, this characteristic behavior of $\Delta\Sigma(\lambda)$ has to continue for even larger cluster sizes, because the limit $L \rightarrow \infty$ requires $\Delta\Sigma(\lambda) \rightarrow 0$ for all λ .

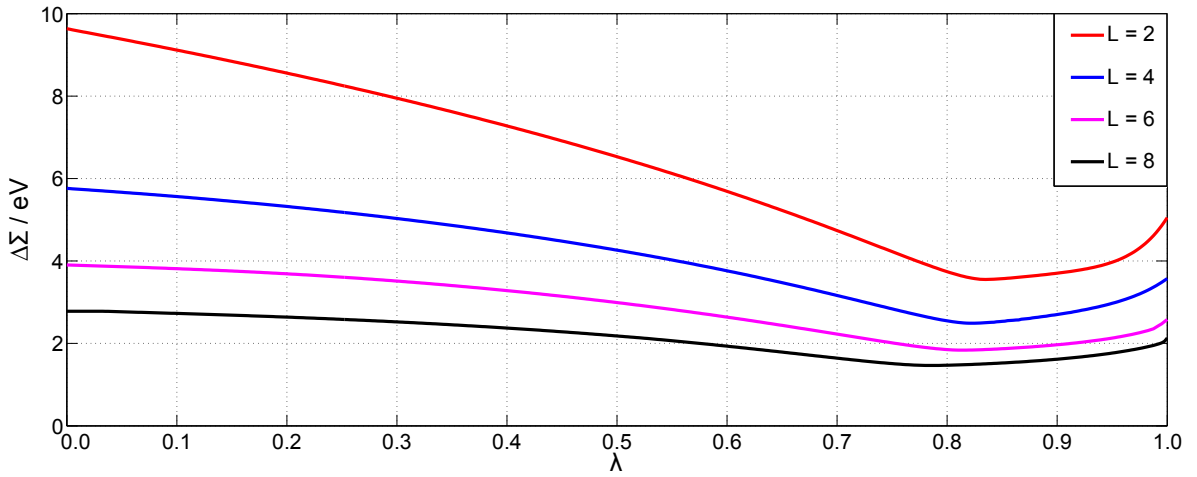


Figure 3.8.: $\Delta\Sigma(\lambda)$ for cluster sizes of $L = 2, 4, 6$ and 8 .

	$L = 2$	$L = 4$	$L = 6$	$L = 8$
λ	0.835	0.823	0.813	0.785

Table 3.1.: Optimal λ for different cluster sizes L according to the minima in figure 3.8

Due to the considerations in this section, we were able to determine the parameter λ and also to base the concept of CPT λ on a well defined cost function. For the calculation of the results presented in the next chapter the obtained optimal λ values (as given in table 3.1) were used.

²⁷or $-U/2$ depending on the definition of the chemical potential μ .

4. Application to a single-orbital system on the Bethe lattice

On the infinitely connected Bethe lattice the DMFT approximation becomes exact and thus the only errors are originating from the impurity solver. This makes the Bethe lattice well suited for benchmarks purposes and for the comparison of impurity solvers. In this chapter the results for ED, CPT and CPT λ are presented for different cluster sizes L and compared to results obtained with continuous-time Monte Carlo (CTQMC) [30], numerical renormalization group (NRG) [31] and matrix product state (MPS) [73] impurity solvers. The main focus is put on the self-energy, the quasiparticle weight and the DOS.

4.1. The Bethe lattice

The Bethe lattice (or Cayle tree) is an infinite lattice where each site has q neighboring sites. The special characteristic of the lattice is that any two sites are connected by an unique shortest path (figure 4.1). In a strict sense the Bette lattice is just a pseudo-lattice, because of the missing translational symmetry for $q > 2$.

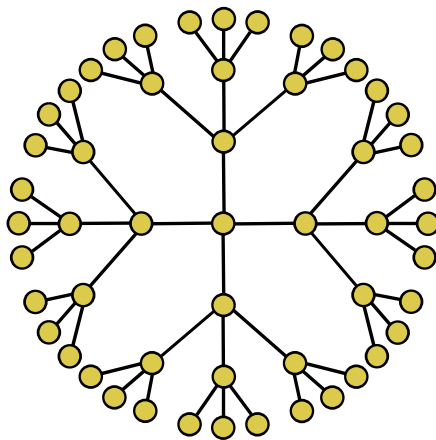


Figure 4.1.: Part of the Bethe lattice with coordination number $q = 4$. The lattice itself is infinite and all sites are equivalent.

An important simplification arises in the limit of infinite coordination ($q \rightarrow \infty$), where the self-energy becomes local in space and thus the DMFT approximation exact (see also section 2.3). To maintain the balance between the kinetic and the Coulomb energy, the nearest-neighbor hopping has to be scaled like [10]

$$\tilde{t} = \frac{t}{\sqrt{q}} \quad (4.1)$$

in this limit. It can be shown that the non-interacting ($U = 0$) DOS on the infinitely connected Bethe lattice is given by [71]

$$\rho_{0,\text{BETHE}}(\omega) = \frac{2}{\pi D} \sqrt{1 - \left(\frac{\omega}{D}\right)^2}. \quad (4.2)$$

This DOS, as drawn in figure 4.2, is smooth and has a semicircular shape with a finite half-bandwidth $D = 2t$.

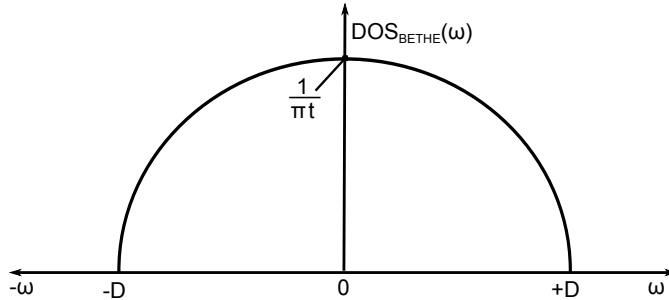


Figure 4.2.: Semicircular non-interacting ($U = 0$) DOS of the Bethe lattice with infinite connectivity ($q \rightarrow \infty$).

The Bethe lattice was pivotal in clarifying the Mott-Hubbard metal-insulator transition of the Hubbard model at half-filling [7, 41, 42, 74, 75] and is now often used for benchmark purposes. The Bethe lattice is usually included in every DMFT code.

4.2. Calculation setup

We adapted an existing `MATLAB` implementation of the DMFT cycle for our purposes, but implemented the impurity solver in `C++` for performance reasons. The impurity solver takes the parameters of the AIM and returns the Green's function in the Q -matrix representation (see appendix D).

In the following sections we will discuss the results of our DMFT calculations for temperature $T = 0$ on the Bethe lattice, where we have chosen $D = 2\text{eV}$ (i.e. $t = 1\text{eV}$) as half-bandwidth of the non-interacting DOS. All calculations were performed on the

real-frequency axis with a numerical broadening of $\eta = 0.05\text{eV}$. As discretization of the frequency axis $4 \cdot 10^3$ points between -20 and 20eV were used. Excitations appearing in the Lehmann representation 3.19 with weights lower than 10^{-10} were neglected, but the fulfillment of the sum-rule 2.7 was checked in every iteration. The calculations were carried out for interactions U/D from 0.0 to 4.5 in steps of $\Delta U/D = 0.05$. The **MATLAB** routine *fminsearch* based on the Nelder-Mead simplex method [76] was used to minimize the cost function 3.3. The starting point for the minimization in the first iteration for a given value of U/D was set to the bath parameters of the converged solution from the previous value of U/D .

On the half-filled Bethe lattice the Hubbard model is particle-hole symmetric and thus the on-site energies are already determined to $\epsilon_0 = -U/2$ and $\epsilon_{i>0} = 0.0$. This simplification was directly implemented to reduce the number of fit parameters. However, if we do not force the solution to be particle-hole symmetric, the required particle-hole symmetry can serve as a check for the correctness of the DMFT implementation.

For each cluster size of $L = 2, 4, 6, 8$ and 10 sites an ED, CPT and CPT λ calculation was performed. The parameter λ of the cost function 3.33 was set to the values determined in the previous chapter (see table 3.1).²⁸ We considered the DMFT self-consistency loop as converged if the integrated absolute change of the bath Green's function $\mathcal{G}_0(\omega)$ between two consecutive iterations dropped below $5 \cdot 10^{-4}$.

Although our DMFT calculations were done on the real axis, we can easily obtain the Matsubara Green's functions of the impurity system and consequently the Matsubara self-energy $\Sigma(i\omega)$ by evaluating the Lehmann representation 3.19 with imaginary frequencies $z = i\omega$. This allows to compare our results to continuous-time Monte Carlo (CTQMC) [30] calculations.²⁹ Note that the CTQMC solver directly works on the Matsubara axis and only for a finite temperature $T > 0$. For the shown results $\beta \cdot D$ was set to 200.

The numerical renormalization group (NRG) [31, 78] impurity solver yields very accurate spectral information around the Fermi energy, due to the logarithmic frequency discretization on the real axis. Therefore, we use NRG to benchmark our results for the quasiparticle weight Z . NRG allows for calculations with $T = 0$ and provides a real-frequency self-energy $\Sigma(\omega)$.³⁰

Another method working on the real axis (and for $T = 0$) is a newly developed matrix product states (MPS) [73] impurity solver. This solver offers a very accurate spectral information over the whole energy range and thus a correct position and shape of

²⁸For $L = 10$ the same λ as for $L = 8$ was used.

²⁹The CTQMC data shown in this thesis was calculated by Markus Aichhorn with the CTQMC impurity solver embedded in the **TRIQS** toolbox [77].

³⁰The NRG self-energy was calculated by Martin Nuss with the **NRG Ljubljana** code [79].

the Hubbard bands. We compare our calculated DOS to the spectra obtained with MPS.³¹

As we will see below, our cluster based impurity solvers can not measure up with all those sophisticated methods in terms of accuracy. However, it should be kept in mind that our solvers benefit from a *low* computational effort, which can be scaled with the cluster size L of the impurity system. A full DMFT calculation for one interaction strength can easily take several hours for CTQMC, NRG or MPS in comparison to a runtime of a few minutes for our cluster based solver, e.g. with $L = 8$. In table 4.2 the CPU time for solving the impurity system is listed for CPT λ and CTQMC. Even if the computational demand of CPT λ is only a few seconds for $L = 10$, it is limited to less than 15 sites due to the exponential growth of the Hilbert space (see discussion in section 3.1). Not too much value should be attached to the necessary number of iterations, because of the strong dependence on the initial starting point and the convergence criteria.

	$L = 2$	$L = 4$	$L = 6$	$L = 8$	$L = 10$	CTQMC
CPU time	0.01s	0.03s	1.00s	3.60s	14.12s	~ 500 s
Iterations	15	27	30	33	32	~ 15

Table 4.1.: CPU time for calculating the impurity Green’s function listed for CPT λ and CTQMC. Calculations were performed on a standard workstation PC.

4.3. Mixing

In figure 4.3 different mixing schemes for the interaction strengths $U/D = 0.5$ (left graph) and $U/D = 1.5$ (right graph) are compared to each other. All calculations were performed with the CPT λ impurity solver and a cluster size of $L = 4$. For simple and Broyden mixing the parameter α was set to 0.8. For this benchmark we used the non-interacting system (i.e. $\Sigma(\omega) = 0$) as initial guess for the DMFT cycle. We measured the convergence by comparing the integrated difference in the bath Green’s function $\mathcal{G}_0(\omega)$ of two consecutive iterations.

In the very first iterations simple mixing and the Broyden’s method show a similar behavior, because the starting approximation is basically the same for both mixing schemes (see appendix B). Clearly, Broyden mixing exhibits a much faster convergence rate after the first initial steps. If CPT λ is used as impurity solver it is likely that the DMFT self-consistency cycle starts to oscillate between solutions. We can observe in figure 4.3 that Broyden mixing is able to break those oscillations.

³¹The MPS calculations were performed by Martin Ganahl and published in [73].

As seen in both graphs and concluding from experience, Broyden mixing typically converges faster and is more stable when performed in $\Sigma(\omega)$.

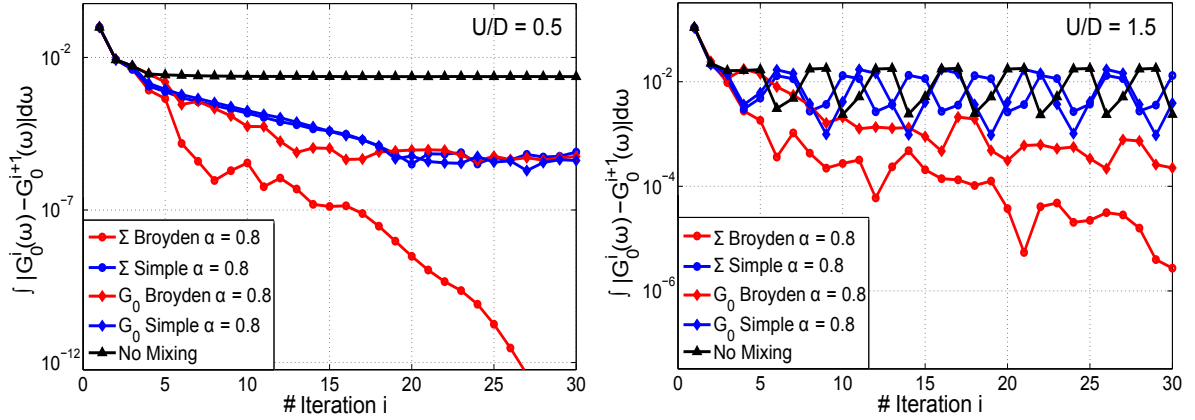


Figure 4.3.: Convergence comparison of simple mixing (blue), Broyden mixing (red) and DMFT without mixing (black). Both mixing schemes were performed in the self-energy $\Sigma(\omega)$ (\bullet) and the bath Green's function $\mathcal{G}_0(\omega)$ (\diamond). The calculations were obtained with CPT λ ($L = 4$) with interactions $U/D = 0.5$ (left) and $U/D = 1.5$ (right). As mixing parameter $\alpha = 0.8$ was used.

However, already simple mixing does improve the convergence for the lower interaction $U/D = 0.5$, but cannot prevent the oscillations for $U/D = 1.5$. Simple mixing usually shows a similar convergence whether performed in the self-energy $\Sigma(\omega)$ or the bath Green's function $\mathcal{G}_0(\omega)$.

Overall, the Broyden mixing scheme works better than simple mixing and turns out to be particularly useful when consecutive iterations start to oscillate. The implementation of Broyden's method is straight forward and the advantages are underlined by the convincing convergence acceleration over the simple mixing scheme.

For the results presented in the following sections, Broyden mixing was switched on after a thermalization period of 10 DMFT steps and restarted after every 20th iteration (as suggested in appendix B).

4.4. Fullfillment of the DMFT self-consistency

One important aspect of every DMFT calculation is the fulfillment of the self-consistency condition 2.16. Therefore, we compare the converged Green's functions of the impurity system $g(\omega)$ and the local lattice Green's function $G_{loc}(\omega)$ in figure 4.4. The results were obtained with an interaction of $U/D = 1.0$ and a cluster size of $L = 6$.

Of course, the claimed self-consistency can never be reached with the finite impurity system used in ED. The impurity Green's function is given by the Lehman representation 3.19 and is thus composed of broadened delta peaks located at the excitation energies. This leads to a rather strong deviation of the impurity Green's function $g(\omega)$ from the local lattice Green's function $G_{loc}(\omega)$ (see upper left graph in figure 4.4).

The CPT impurity Green's function as given by equation 3.25 is a continuous function within the band-width of the coupled semi-infinite chain. The peaks outside the continuous part (see upper right graph in figure 4.4) are stemming from cluster excitation, which do not lie within the band-width of the bath chain. For CPT both Green's functions show a much better agreement than within ED, whereby the remaining deviation is influenced by our restriction on the chain parameters (see section 3.2.1). When we compare the two red lines in the upper graphs of figure 4.4, we note that the converged CPT DOS is very much different from the ED DOS. Our newly proposed method CPT λ does also improve the self-consistency condition, but the CPT λ spectra provides the best accordance with MPS, as we will see below.

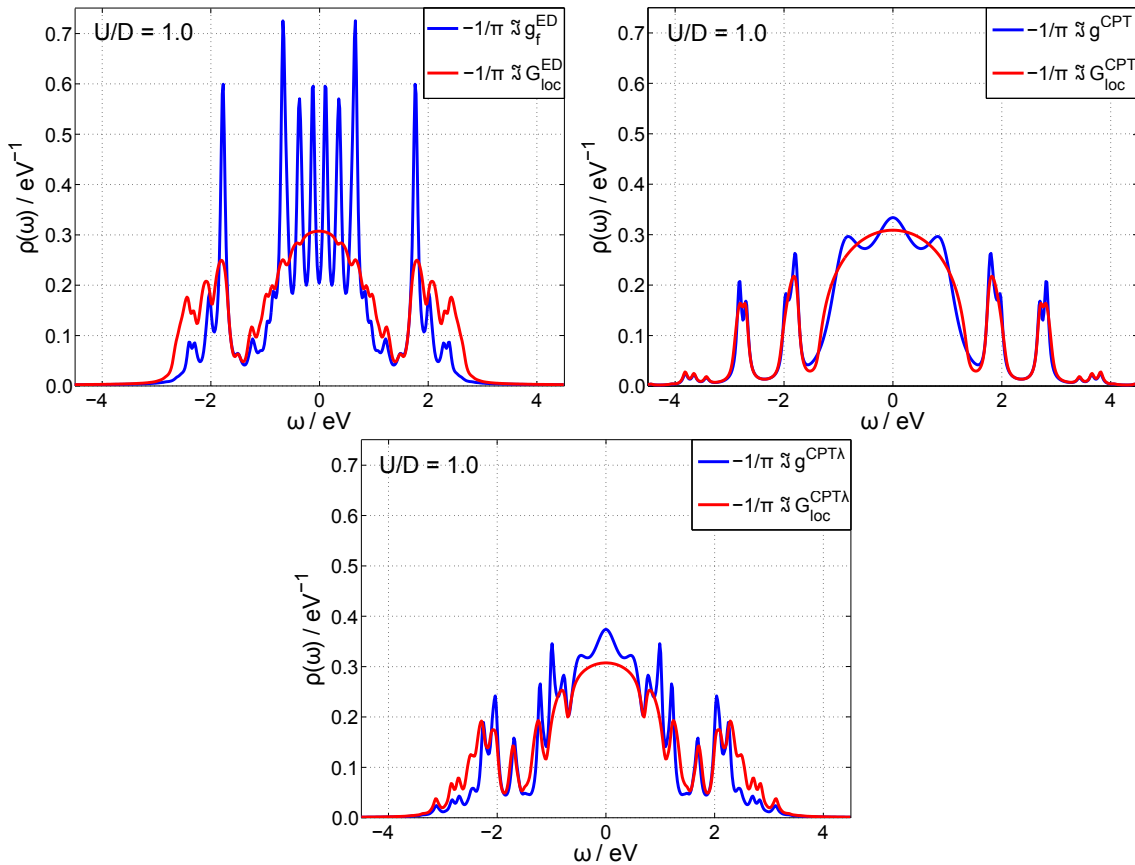


Figure 4.4.: Comparison of the local lattice Green's function $G_{loc}(\omega)$ (red) and the impurity model Green's function $g(\omega)$ (blue) for ED (upper left), CPT (upper right) and CPT λ (lower). The cluster size was set to $L = 6$ and the interaction to $U/D = 1.0$.

4.5. Self-energy and quasiparticle weight

We start our discussion with figure 4.5, where we compare the imaginary part of the Matsubara self-energy $\Im\Sigma(i\omega)$ of our investigated impurity solvers ED (green), CPT (red) and CPT λ (blue) to the exact results from CTQMC (black). The Matsubara self-energy is shown for three interaction strengths in the metallic regime ($U/D = 1.0, 2.0$ and 2.6). The first observation we make is the overestimation of the Matsubara self-energy by ED and the underestimation by CPT for all interactions. The CPT λ self-energy is located somewhere in between those two extremes, but is in general slightly too large. The largest deviations occur for the smallest number of bath sites (i.e. $L = 2$).

For $U/D = 1.0$ the Matsubara self-energies of all three methods are converging towards the CTQMC result with increasing cluster size L . This expected behavior is strongly pronounced in ED, where the smallest impurity system ($L = 2$) yields the Matsubara self-energy farthest from CTQMC. Remarkably, CPT λ shows overall a much weaker spread with $L = 4$ giving a self-energy already closer to CTQMC than ED ($L = 8$). Despite the fact that the CPT self-energies are close to the CTQMC self-energy for this interaction strength, the largest deviations are found in the very important region of low Matsubara frequencies.

Looking at the second depicted interaction strength ($U/D = 2.0$), we observe that the CPT λ results lie close to each other without an apparent trend towards the CTQMC self-energy. Still all CPT λ results provide a better estimation than ED with as much as 8 sites. The wrong low frequency behavior of CPT is now even more pronounced and additionally an increase of the cluster size does not lead to a significant improvement.

In contrast to the two lower interaction strengths, the third example with $U/D = 2.6$ is located in the difficult region close to the phase transition. Unexpectedly, the self-energy given by ED and CPT λ show a reverted trend as a function of the cluster size L , whereby only $L = 2$ falls out of the line. Again, CPT suffers from an extremely poor low energy behavior.

All methods resemble the correct high frequency behavior and feature the required asymptotic course to $\Im\Sigma(i\omega) = 0$ for $i\omega \rightarrow \infty$. Beside that, CPT λ outperforms both ED and CPT when regarding the low Matsubara frequencies (see right column in figure 4.5) up to about 1eV. We argue that CPT λ provides the most reasonable results for the self-energy, because of the correct behavior for both low and high Matsubara frequencies. We will further elaborate on the low energy region in the discussion of the quasiparticle weight Z below.

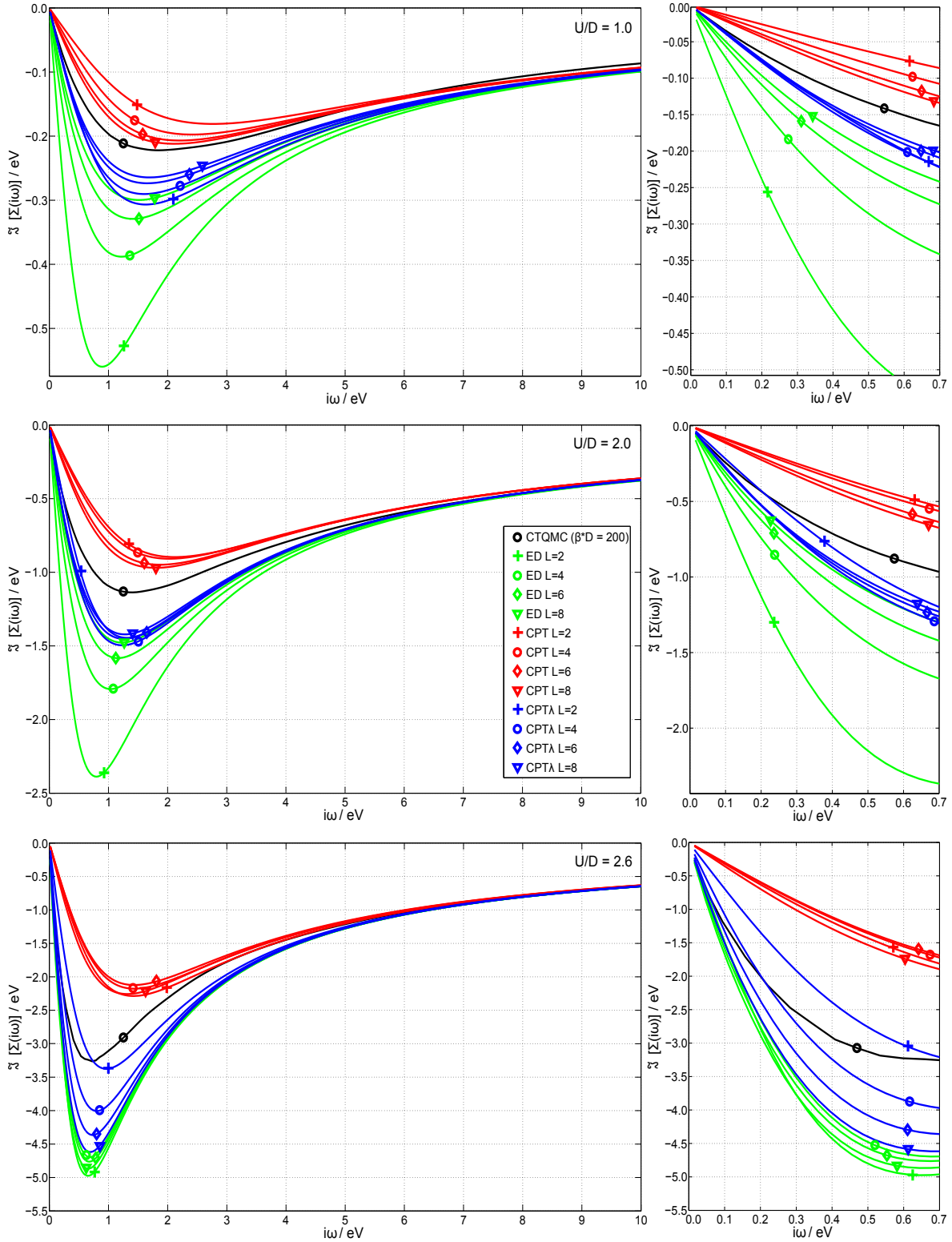


Figure 4.5.: Imaginary part of the Matsubara self-energy $\Im[\Sigma(i\omega)]$ for $U/D = 1.0$ (upper panel), $U/D = 2.0$ (middle panel), $U/D = 2.6$ (lower panel) with ED (green), CPT (red) and CPT λ (blue) as impurity solvers. The calculations were performed for cluster sizes of 2 (+), 4 (\circ), 6 (\diamond) and 8 (∇) sites and are compared to CTQMC (black) with $\beta D = 200$. The right graphs show the low energy details.

On the half-filled Bethe lattice the real part of the Matsubara self-energy is a constant given by $\Re\Sigma(i\omega) = U/2$. As shown in figure 4.6, this is indeed very accurately satisfied by all studied methods. The only exception is the cluster size $L = 2$, where a small deviation from the constant value can be observed at low Matsubara frequencies. The CTQMC self-energy exhibits oscillations, which are caused by the statistical nature of every Monte Carlo calculation. In contrast, our Hamiltonian based impurity solvers do not suffer from any statistical errors.

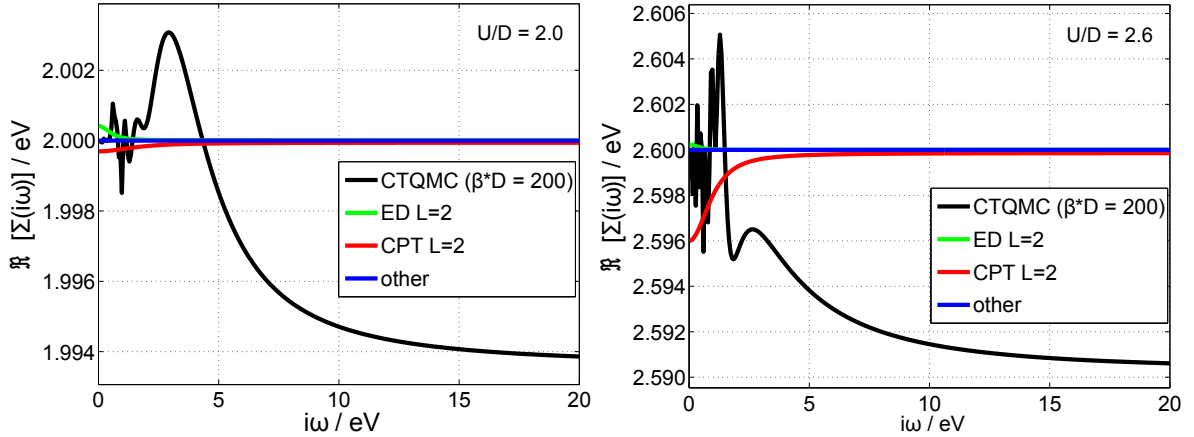


Figure 4.6.: Real part of the Matsubara self-energy $\Re\Sigma(i\omega)$ for ED with $L = 2$ (green), CPT with $L = 2$ (red) and CPT λ as well as all other cluster sizes (blue) compared to CTQMC (black) with $\beta D = 200$. The interaction strength was set to $U/D = 2.0$ (left) and $U/D = 2.6$ (right).

Before we turn to the discussion of the quasiparticle weight Z , we have a brief look on the general form of the Matsubara self-energy as a function of the interaction strength U/D . In figure 4.7 the effect of the electronic correlation is shown for CPT λ ($L = 10$). In the case of a non-interaction system ($U/D = 0$) the self-energy is trivially zero ($\Sigma(i\omega) = 0$). However, for $U/D \neq 0$ it features a very distinctive curvature and develops a minimum, which gets shifted downwards zero with increasing interaction. In the metallic regime the self-energy goes to zero for both $i\omega \rightarrow 0$ and $i\omega \rightarrow \infty$. According to the definition 2.38, the slope at $i\omega = 0$ corresponds to the quasiparticle weight Z . Above the phase transition, i.e. in the insulating regime, the self-energy diverges and thus the quasiparticle weight Z is zero.

We concluded in the discussion of figure 4.5 that CPT λ provides a good approximation of the self-energy especially for low Matsubara frequencies. This observation gets also reflected in the quasiparticle weight Z , which is presented in figure 4.8 as a function of the interaction strength U/D . All investigated impurity solvers (ED, CPT and CPT λ) provide a qualitatively correct behavior of Z . For the non-interacting system ($U/D = 0$) the quasiparticle weight is one and within the metallic phase it gradually

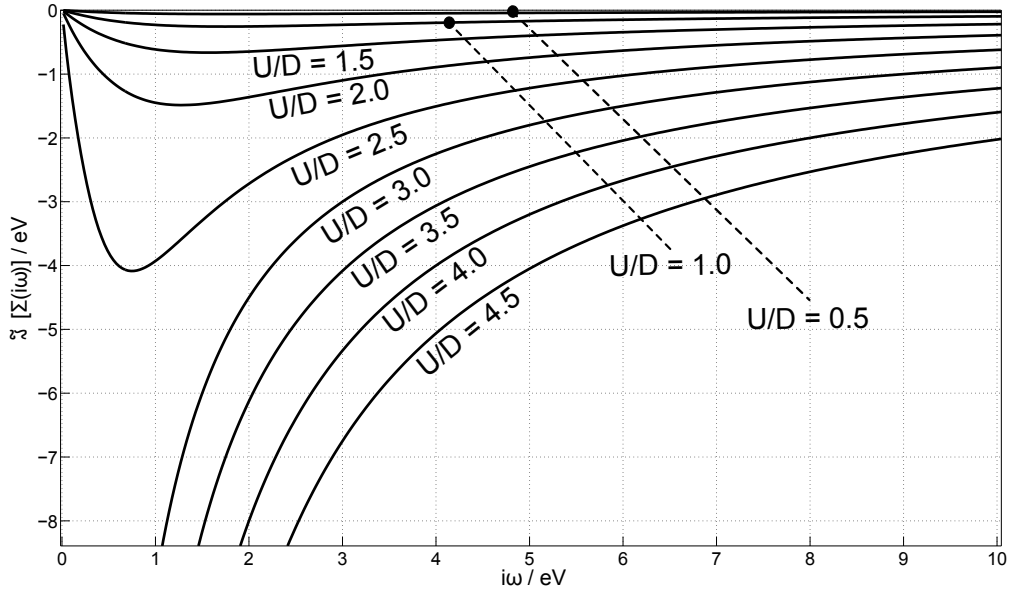


Figure 4.7.: Dependence of the imaginary part of the Matsubara self-energy $\Im\Sigma(i\omega)$ on the interaction U/D for $CPT\lambda$ with a cluster size of $L = 10$.

decreases when U/D is increased. In the insulating regime the quasiparticle weight is equal to zero. Nevertheless, only ED and $CPT\lambda$ reproduce the *characteristic* mirrored \mathcal{S} -shape of the NRG result.

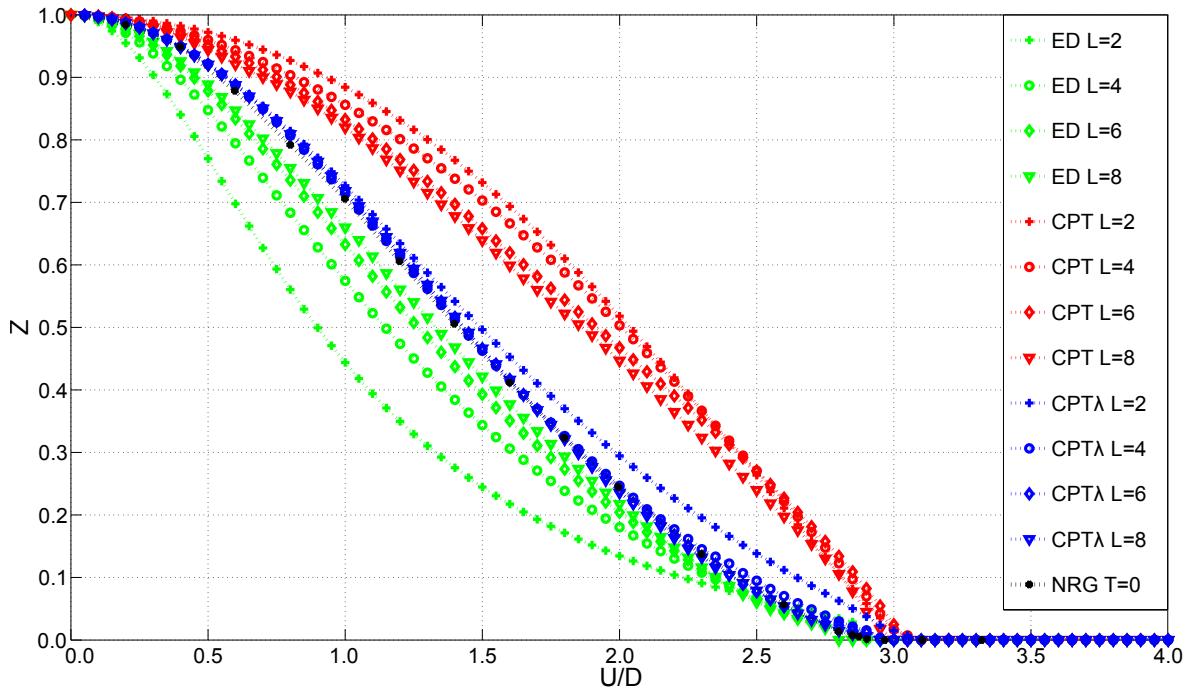


Figure 4.8.: Quasiparticle weight Z over U/D for ED (green), CPT (red) and $CPT\lambda$ (blue). Our results for clusters of 2 (+), 4 (o), 6 (x) and 8 (v) sites are compared to NRG data (black) taken from [80].

In general, ED underestimates the quasiparticle weight Z , but converges towards NRG with increasing cluster size L . On the other side, CPT overestimates Z strongly, but also displays a correct convergence behavior (see also figure 4.9). The quasiparticle weight provided by CPT for a cluster size of $L = 8$ is still far from the NRG data points, particularly for interactions above $U/D \sim 0.5$. $\text{CPT}\lambda$ shows a remarkably good accordance with NRG. For the cluster size $L = 4$ the quasiparticle weight almost covers the NRG data points, whereby the $\text{CPT}\lambda$ results for $L = 6$ and $L = 8$ imply that Z is already well converged to its final value. We want to stress here that there are *no* parameters in the $\text{CPT}\lambda$ theory that are adjusted to fit Z .

The convergence of the quasiparticle weight Z with cluster size L for two selected interactions ($U/D = 0.6$ and 1.6) is depicted in figure 4.9. As we already mentioned above, ED and CPT show a convergence towards the correct NRG quasiparticle weight. While CPT gives a vastly wrong result even for a cluster size of $L = 10$ (see right graph in figure 4.9), $\text{CPT}\lambda$ provides the correct Z already for a cluster as small as 4 sites.

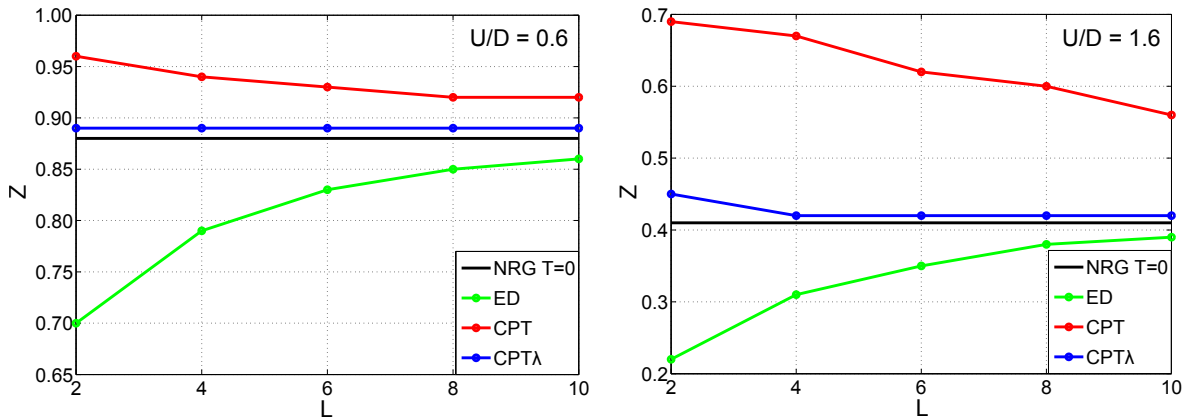


Figure 4.9.: Convergence of the quasiparticle weight Z with increasing cluster size L for ED (green), CPT (red) and $\text{CPT}\lambda$ (blue) to the NRG value from reference [80]. The interaction was set to $U/D = 0.6$ (left) and $U/D = 1.6$ (right).

Here we will investigate the region around the metal-insulator phase transition only briefly, because it is not the main focus of this work. Anyhow, the interested reader shall be referred to [41, 42, 43, 44], where the Mott-Hubbard phase transition on the Bethe lattice is studied in greater detail. A zoom into figure 4.8 of the region around the phase transition is given in the left graph of figure 4.10. Noteworthy, all methods provide a very good estimation for the critical phase transition point U_{c2}/D , which was determined to $U_{c2}/D = 2.95$ for the NRG reference data in [80]. It is important to remember that calculations close to the phase transition are subjected to a slow convergence of the DMFT cycle. Calculating the data points to a high precision is difficult, because the DMFT self-consistency cycle turns out to be rather unstable in this region. This is due to the coexistence of both an insulating and a metallic solution

(see also section 2.6). For example, regard the quasiparticle weight for ED, where Z jumps from a finite value to zero rather abruptly. This happens, because the metallic solution can not be stabilized anymore. Consequently, it is rather difficult to determine the *precise* value of the phase transition point U_{c2}/D .

In our DMFT calculations we move along the $T = 0$ line of the phase diagram illustrated in figure 2.7. Due to our calculation setup, where we increase the interaction stepwise and start each DMFT cycle with the parameters obtained from the previous interaction, the solution is forced to stay in the metallic phase up to the transition point U_{c2}/D . If the calculation is performed in the other direction, thus starting in the insulating phase and decreasing the interaction stepwise, the solutions remains insulating down to U_{c1}/D . The result is a hysteresis in the quasiparticle weight Z , which is displayed for ED ($L = 4$) in the right graph of figure 4.10. In addition to the solution shown in figure 4.8, a second solution is found between the interactions $U_{c1}/D = 2.1$ and $U_{c2}/D = 2.9$. These interactions mark the coexisting region of the metallic and the insulating solution. At the lower transition point the quasiparticle weight jumps abruptly from $Z = 0$ to the finite Z value of the purely metallic phase. It should be mentioned that most likely the insulating solution is found if the DMFT cycle is started with arbitrary parameters for the impurity system. We did not study the hysteresis for CPT/CPT λ or other cluster sizes.

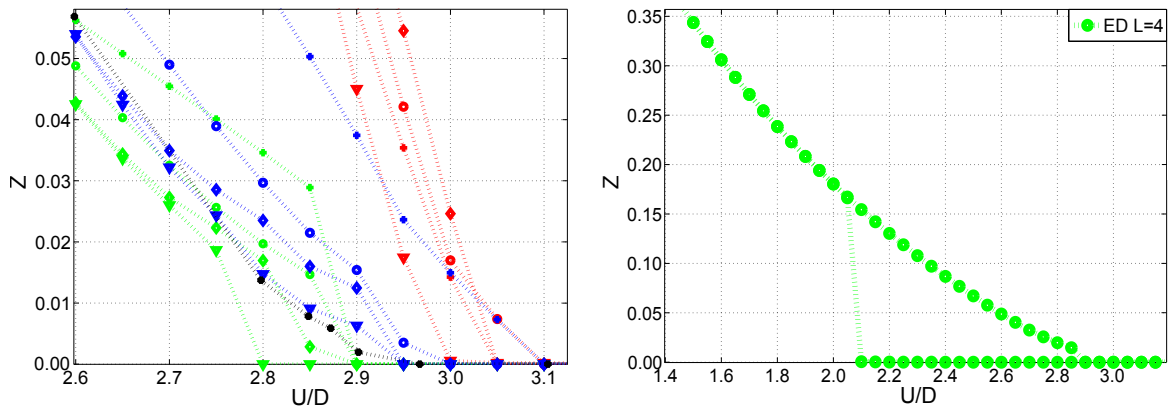


Figure 4.10.: Left: Quasiparticle weight Z versus interaction U/D around the phase transition. For the color code and the markers consider the legend of figure 4.8. Right: Quasiparticle hysteresis obtained with ED ($L = 4$)

After the elaborations on the Matsubara self-energy and the quasiparticle weight, we will now focus on the real-frequency self-energy. The imaginary part of $\Sigma(\omega)$ is presented in figure 4.11, where the results for cluster sizes of $L = 4$ and $L = 8$ are compared to NRG. For this calculations the interaction was set to $U/D = 1.0, 2.0$ and 2.5 . Generally, the self-energy of our cluster based methods feature peaks stemming from finite-size effects of the impurity solvers (see also the discussion in section 3.2.1).

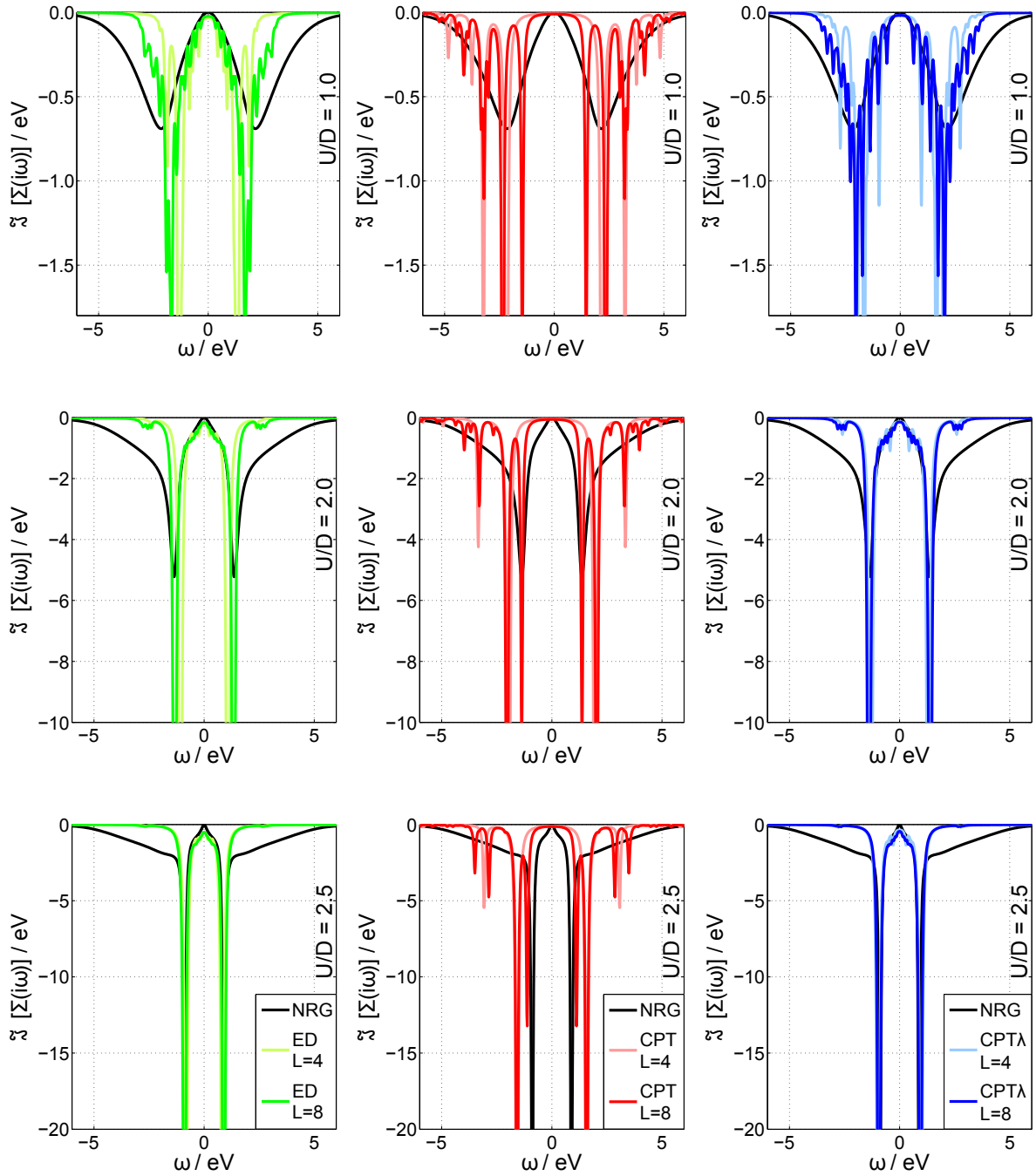


Figure 4.11.: Imaginary part of the real-frequency self-energy $\Im\Sigma(\omega)$ obtained with ED (left column in green), CPT (middle column in red) and CPT λ (right column in blue) for a cluster size of $L = 4$ (light color) and $L = 8$ (dark color) compared to a NRG calculation. Results are shown for interactions U/D of 1.0 (first row), 2.0 (second row) and 2.5 (third row).

For the weakest correlation ($U/D = 1.0$), we find that ED and CPT λ show a good low energy accordance with NRG. In particular for $L = 8$, CPT λ is able to significantly improve on the ED result and to yield a reasonable good representation of the self-energy up to about $\pm 4\text{eV}$. CPT provides only an adequate self-energy above $\sim \pm 4\text{eV}$. As we will see in the next section, contributions above this energy have only a very low spectral weight and are not of primary interest. The extremely poor low energy behavior rules out CPT as a suitable impurity solver.

Turning to the interactions $U/D = 2.0$ and $U/D = 2.5$, we observe that both ED and CPT λ are in a remarkable good accordance with NRG for energies below $\pm 1.5\text{eV}$. Above $\pm 1.5\text{eV}$ both methods show a small imaginary part of the self-energy, which will result in too narrow Hubbard bands (see the DOS $\rho(\omega)$ in the following section). We want to note here that at high energies, NRG suffers from the logarithmic discretization and cannot be taken as an exact reference anymore. CPT, on the other hand, features some parts of the high frequency tail, but entirely fails in the region around the Fermi energy. It should be emphasized that CPT λ ($L = 4$) already provides a self-energy comparable to ED ($L = 8$). This is particularly beneficial when regarding the computational costs, which are of course much lower for a cluster of 4 sites only. For $U/D = 2.5$ the results for CPT λ and ED are very similar and not even a bigger cluster of $L = 8$ leads to an observable improvement.

4.6. Density of states

Finally, we come to the study of the Bethe lattices DOS $\rho(\omega)$, which is shown for calculations performed with a cluster size of $L = 4$ in figure 4.12 and for $L = 8$ in figure 4.13. The DOS $\rho(\omega)$ was calculated from the local lattice Green's function $G_{loc}(\omega)$ with equations 2.6 and 2.8. For the particle-hole symmetric half-filled Hubbard model the DOS is of course symmetric around the Fermi energy. In general, the DOS calculated with our cluster based impurity solvers suffer from severe finite-size effects (e.g. see first panel in figures 4.12 and 4.13), which are due to the peaked structure of the self-energy $\Sigma(\omega)$. In addition, the Hubbard bands for the intermediate interactions are much too high and notably too narrow in comparison to the MPS DOS. This is primarily caused by the unsatisfying high energy representation of the self-energy $\Sigma(\omega)$.

As we conclude in the previous discussion, the weight contributing to the quasiparticle is too high in CPT, too low in ED and almost correct in CPT λ (see the second and third panel in figures 4.12 and 4.13). Both ED and CPT λ provide the correct shape of the quasiparticle peak, but to the contrary, the CPT quasiparticle peak has a strongly semi-elliptical shape. Interestingly, for $U/D = 2.0$ and $U/D = 2.6$ the area under the quasiparticle peak of the CPT λ DOS seems to be too small. However, it is difficult to

determine a sharp end of the quasiparticle peak in the MPS DOS for the estimation of its spectral weight. Especially for $U/D = 2.0$, the Hubbard bands might have large tails reaching into the central region. Importantly, if we integrate the spectra from -1 to 1eV , we find that the difference in the weight of the quasiparticle peak between MPS and CPT λ is only of order $O(10^{-2})$ in absolute numbers.³²

For the lowest depicted interaction strength $U/D = 1.0$ (first panel in figure 4.12), we observe that CPT λ ($L = 4$) not just improves on the central weight, but also shifts the weight of the emerging Hubbard bands to higher energies. Beside the low-energy contribution, the CPT result consists of three distinctive peaks above $\pm 2\text{eV}$ with a very poor representation of the whole spectrum. We argue that CPT λ provides the DOS with a shape closest to the MPS result. The DOS of all three cluster based solvers show a significant improvement when the cluster size is increased to $L = 8$ (first panel in figure 4.13). Again, note the overall good accordance of the CPT λ and the MPS spectrum.

Now we turn to the DOS $\rho(\omega)$ for $U/D = 2.0$ presented in the second panel of figures 4.12 and 4.13. In comparison to CPT λ ($L = 4$), the Hubbard bands in ED are slightly shifted to too low energies. It should be emphasized that the CPT λ bands stay essentially at the same position for $L = 8$, but that the ED bands are moving towards the CPT λ result. On the other hand, the CPT bands feature a two peak structure located at too high energies. Surprisingly, for $L = 8$ and $U/D = 2.0$ CPT gives the broadest, but strongest peaked Hubbard bands, which exhibit a good high energy behavior (between ± 3 and $\pm 5\text{eV}$).

We observe a nearly identical DOS of CPT λ /ED and that even for both cluster sizes ($L = 4$ and $L = 8$) in the third panel of figures 4.12 and 4.13 for $U/D = 2.6$. For this interaction the Hubbard bands obtained with our solvers are centered right in the middle of the MPS Hubbard bands. Again, the CPT ($L = 4$) Hubbard bands possess a two peaked structure shifted to too high energies, but for $L = 8$ a third peak appears leading to a slightly lower and wider Hubbard band. Another small peak is wrongly placed at about $\pm 1\text{eV}$ right in between the Hubbard band and the quasiparticle peak.

In the insulator ($U/D = 3.2$) the spectral weight at $\omega = 0$ vanishes and thus the spectrum consists only of the two Hubbard bands (see lowest panel in figures 4.12 and 4.13). As the electrons become localized the implication for the impurity model is that the interacting site *decouples* from the bath.³³ This means that we are left with an atomic problem which is completely independent of the number of bath sites and consequently also independent of the used impurity solver. It follows from the atomic limit that the Hubbard bands have to be separated by the energy U .

³²This is also confirmed by the quasiparticle weight shown in figure 4.8.

³³i.e. hopping t_{01} goes to zero.

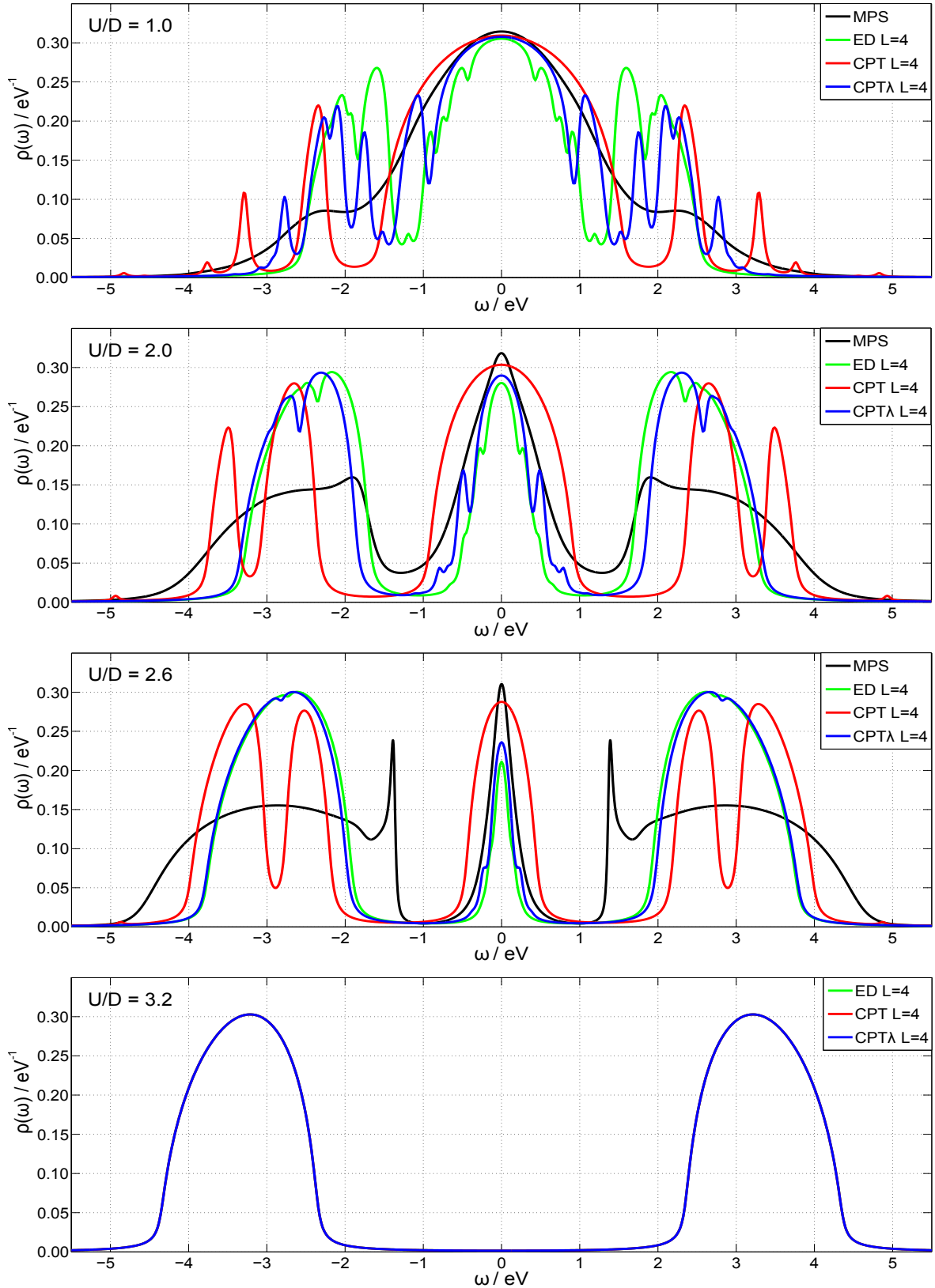


Figure 4.12.: DOS $\rho(\omega)$ for interactions $U/D = 1.0$ (first panel), $U/D = 2.0$ (second panel), $U/D = 2.6$ (third panel) and $U/D = 3.2$ (fourth panel). The ED (green), CPT (red) and CPT λ (blue) results for a cluster size $L = 4$ are compared to a DOS calculated with MPS (black).

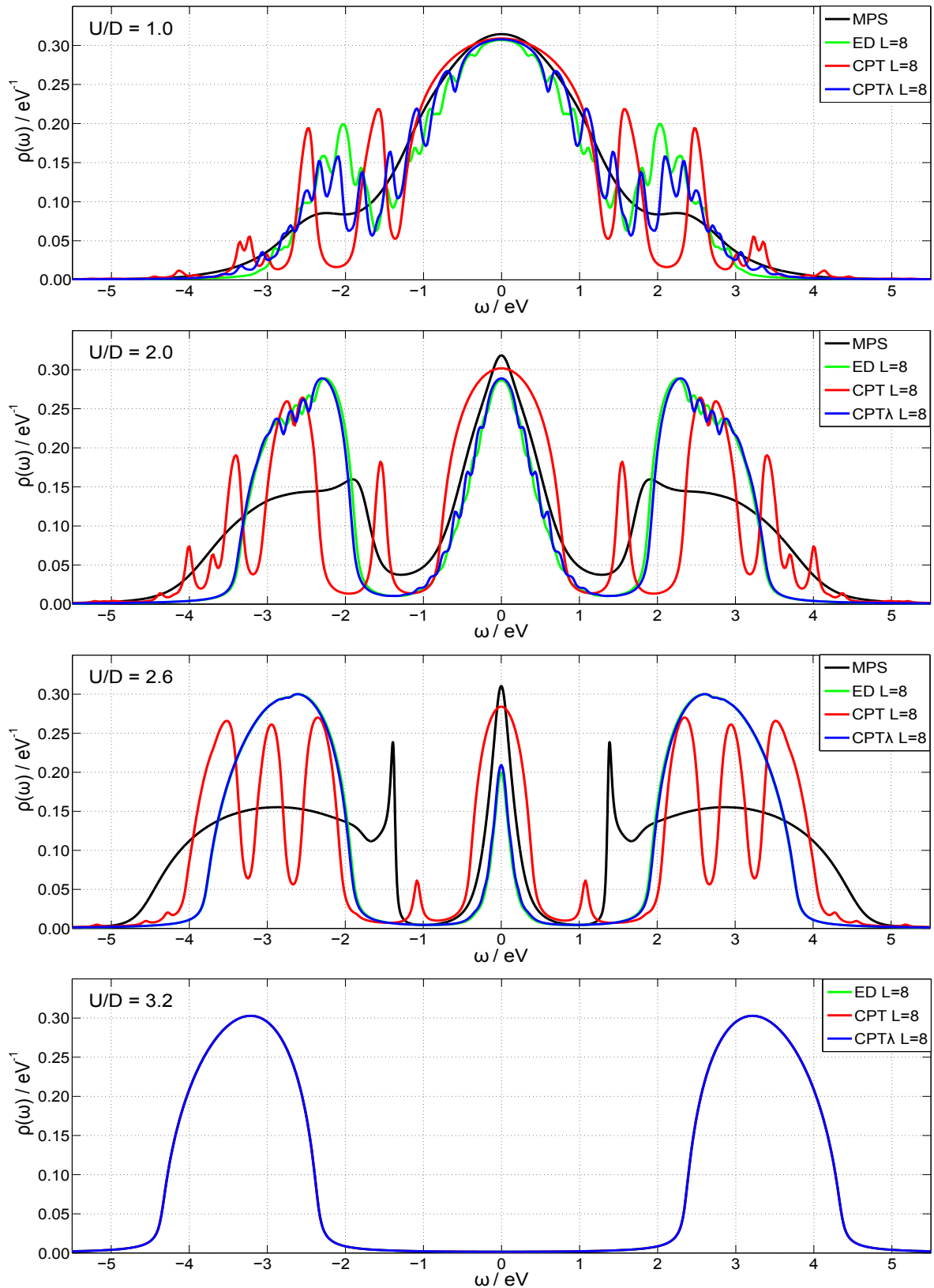


Figure 4.13.: DOS $\rho(\omega)$ for interactions $U/D = 1.0$ (first panel), $U/D = 2.0$ (second panel), $U/D = 2.6$ (third panel) and $U/D = 3.2$ (fourth panel). The ED (green), CPT (red) and CPT λ (blue) results for a cluster size $L = 8$ are compared to a DOS calculated with MPS (black).

Of course, the CPT λ impurity solver can not reproduce the fine details of the spectrum as revealed by MPS. For example, it is not possible to resolve features like the sharp peak at the edge of the Hubbard bands for $U/D = 2.6$ with a feasible number of bath sites. Nonetheless, the general properties of the DOS over the whole interaction range are still represented. Those are the position of the Hubbard bands, the weight distribution between them and the central quasiparticle peak and the shape of the quasiparticle peak itself.

Next, we briefly study the effect of the numerical broadening η . The converged parameters of the impurity system obtained from a DMFT calculation with $\eta = 0.05\text{eV}$ were used to evaluate the self-energy for two additional broadenings ($\eta = 0.5\text{eV}$ and $\eta = 0.005\text{eV}$).³⁴ As usual, the DOS $\rho(\omega)$ for an altered broadening follows from equations 2.6, 2.8 and 2.18 with $z = \omega + i\eta$. The results are depicted for CPT λ ($L = 8$) and $U/D = 2.0$ in figure 4.14.

For the smallest broadening $\eta = 0.005\text{eV}$ the finite-size peaks are strongly pronounced, but it is important to point out that the maximum of the quasiparticle peak at the Fermi energy obeys the Luttinger pinning of the DOS [81], which is in our case $\rho(0) = 1/\pi$ (see also equation 4.2 and figure 4.2). Additionally, the spectral weight around $\omega = 0$ resembles the MPS result closely. For a higher η this is not fulfilled anymore, because at the same time the broadening reduces the height of the peak to preserve the total weight. The extreme example of $\eta = 0.5\text{eV}$ smears out the entire spectrum such that it appears to be smooth. We argue that $\eta = 0.05\text{eV}$ is a good tradeoff between 'correctness' and smoothness of the DOS.

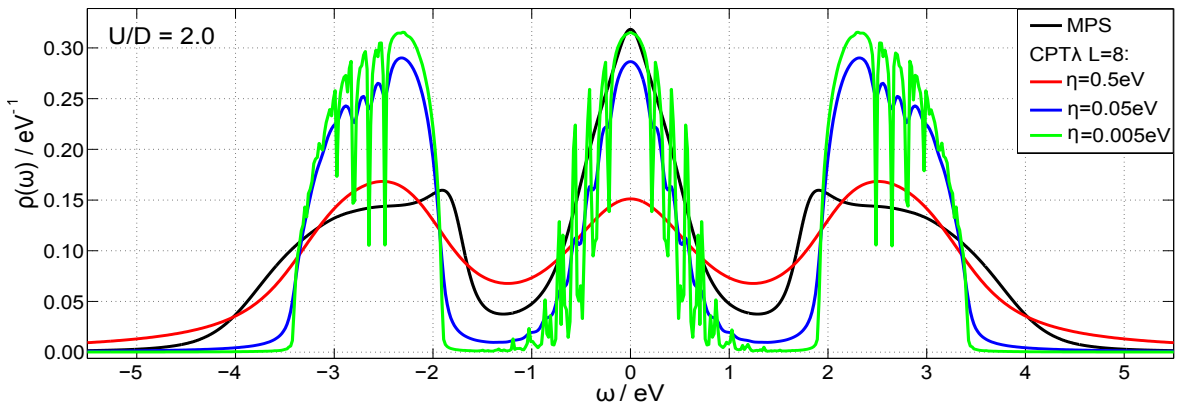


Figure 4.14.: Dependence of the DOS $\rho(\omega)$ on the numerical broadening η . The CPT λ ($L = 8$) calculation for $U/D = 2.0$ was performed with $\eta = 0.05\text{eV}$ (blue). Using equations 2.6, 2.8 and 2.18 the DOS was evaluated again with $\eta = 0.005\text{eV}$ (green) and $\eta = 0.5\text{eV}$ (red).

³⁴Note that this is not the same as performing DMFT with a different broadening η , which was not studied within the scope of this thesis.

The remarkable accordance of the CPT λ ($L = 10$) DOS for $U/D = 1.0$ with the MPS DOS is shown in figure 4.15. Despite the simplicity and the low computational demand of our impurity solver, we are able to reproduce the overall shape of the spectrum in the weakly correlated regime surprisingly well. As mentioned above, the spikes in the CPT λ spectrum are due to finite-size effects of the cluster. To increase the accompanied energy resolution of the bath for a smoother spectrum a cluster size far beyond the computational limit would be necessary.

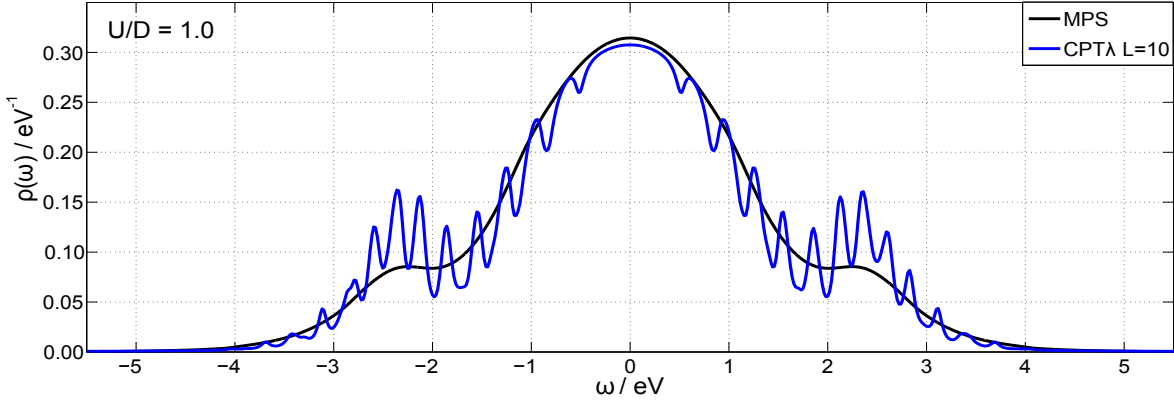


Figure 4.15.: CPT λ ($L = 10$) DOS compared to the MPS DOS for $U/D = 1.0$.

The evolution of the DOS for CPT λ as a function of the interaction U/D is illustrated for $L = 10$ in figure 4.16 and for $L = 8$ in figure 4.17.

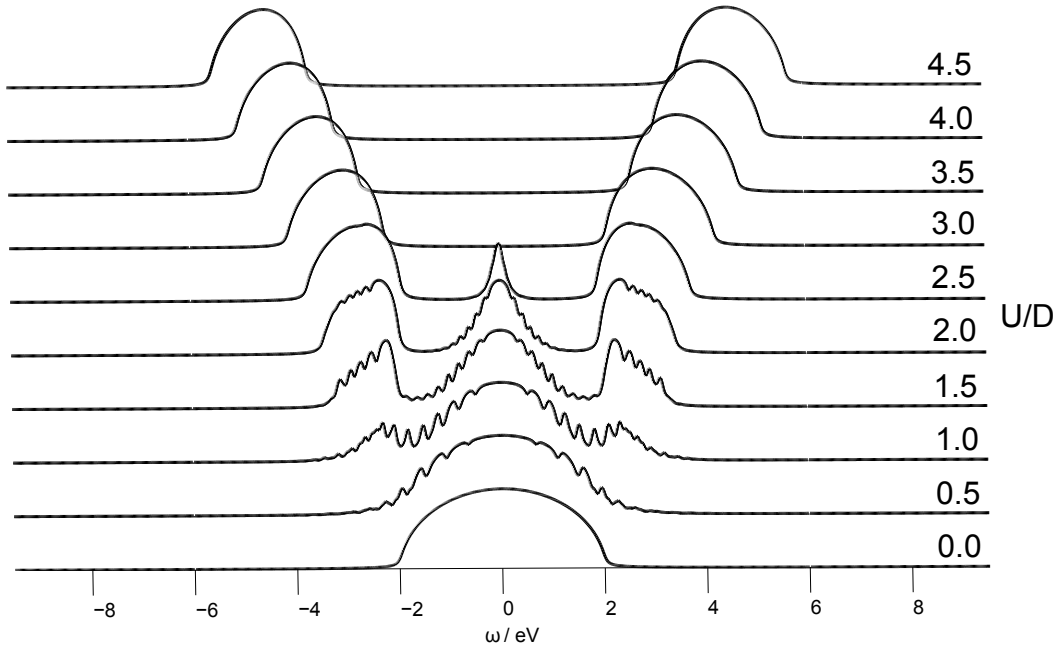


Figure 4.16.: Evolution of the DOS for CPT λ ($L = 10$) as a function of U/D with steps of $\Delta U/D = 0.5$.

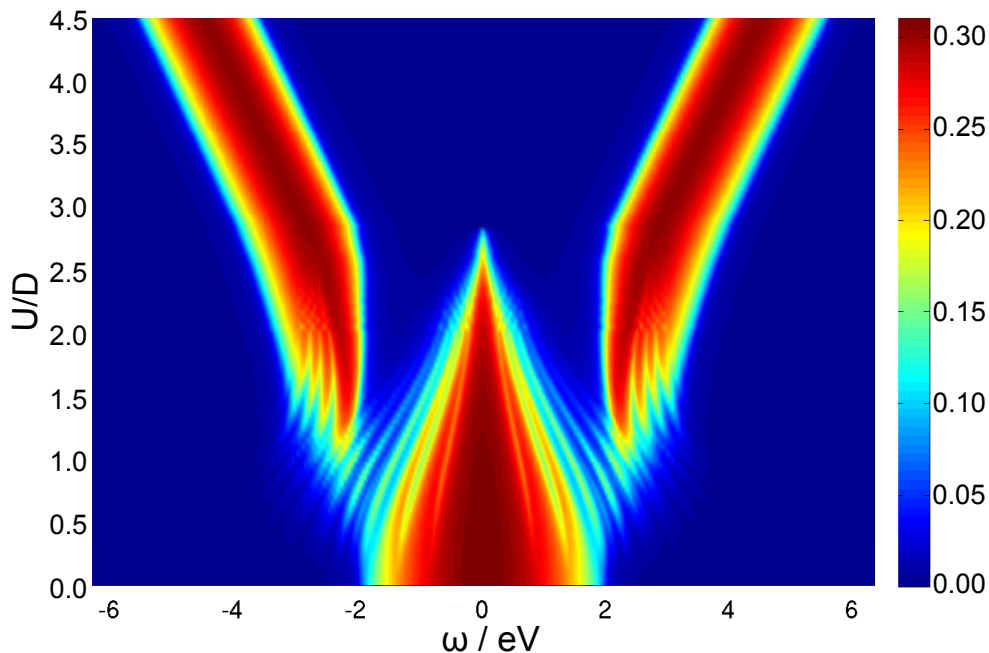


Figure 4.17.: Evolution of the DOS for CPT λ ($L = 8$) as a function of U/D with steps of $\Delta U/D = 0.05$.

Both 3D plots reveal the development of the characteristic three peak structure with increasing interaction U/D . In the weak correlation regime the semicircular DOS of the non-interacting Bethe lattice starts to broaden, but already for $U/D = 1.0$ the emerging Hubbard bands are clearly visible. When approaching the phase transition spectral weight gets transferred from the central quasiparticle peak to the more and more pronounced Hubbard bands. At the phase transition point U_{c_2}/D the quasiparticle peak vanishes and the spectrum is left with the Hubbard bands, which are separated by the energy difference U . In conclusion, CPT λ offers a reasonable description of the DOS over the whole interaction range.

5. Application to a multi-orbital system - SrVO₃

While NRG, MPS and other sophisticated methods are certainly superior to the CPT λ impurity solver in the one-band case, they are not directly applicable to multi-orbital systems. The only restriction of CPT λ is the number of sites treated within the interacting cluster and thus multi-orbital systems can be addressed with our impurity solver. In this chapter we apply ED and CPT λ to the correlated paramagnetic material SrVO₃ and compare the results to a CTQMC calculation. The properties of SrVO₃ were already extensively studied experimentally as well as within the DFT+DMFT approach, e.g. in the references [82, 83, 84, 85, 86].

5.1. The material and DFT results

SrVO₃ belongs to the group of transition metal oxides and has a cubic perovskite crystal structure ($Pm\bar{3}m$) with a $3d^1$ electronic configuration [87] (see figure 5.1). Due to the influence of electric fields caused by the neighboring oxygen atoms in the octahedral environment, the five-fold degeneracy of the vanadium d -orbitals is lifted, because wavefunctions pointing towards the oxygen ions have a higher energy than those pointing between them. This crystal-field causes the $3d$ states to split into e_g and lower lying t_{2g} states. For a crystal with perfect cubic symmetry (like SrVO₃) hybridization between e_g and t_{2g} states is forbidden. The states within both subbands are two-fold and three-fold degenerated (see figure 5.2) [88]. The only electron in the d^1 configuration sits on a t_{2g} level and the empty e_g states are well separated in energy.

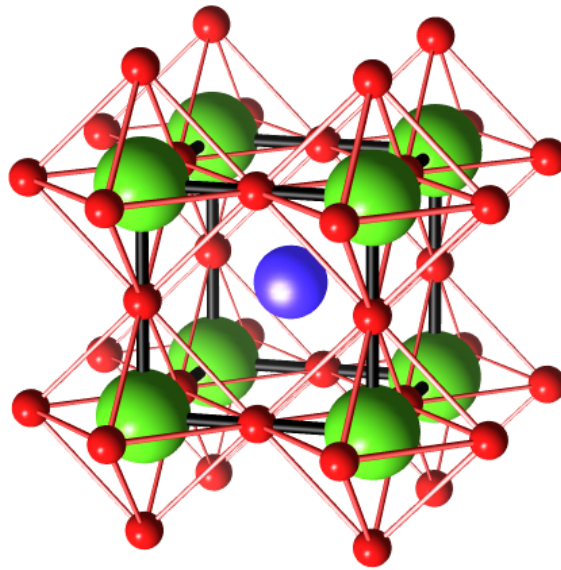


Figure 5.1.: SrVO₃ crystal structure. Blue sphere: strontium; green spheres: vanadium; red spheres: oxygen; red lines: oxygen octahedra; black lines: cubic vanadium grid (unit cell). The size of the atoms is not to scale. Drawn with the free software Balls&Sticks [89].

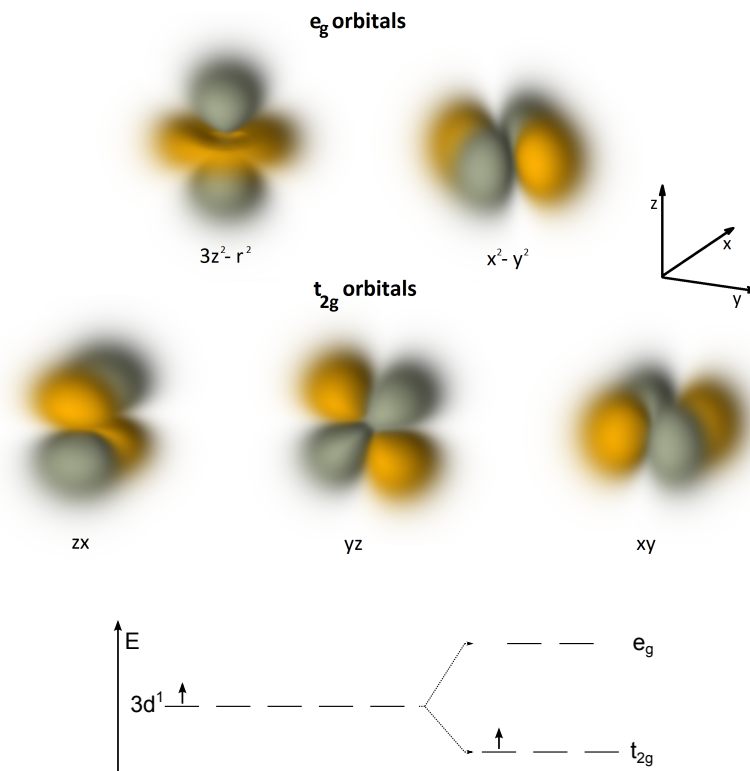


Figure 5.2.: Upper: 3d-orbitals in the cubic crystal-field drawn with the free software Orbital Viewer [90]. Lower: Splitting of the vanadium 3d-orbitals in cubic SrVO₃. The fivefold degeneracy is lifted to two e_g and three t_{2g} orbitals. The energy splitting is not to scale.

The DFT DOS calculated with the DFT code WIEN2K [91] is shown in the left graph of figure 5.3.³⁵ Because of the d^1 configuration, the t_{2g} manifold is partially filled and the Fermi level cuts through these bands. Below the t_{2g} bands the O-2p states show their main contribution between -7 and -2 eV. From about 1.3 to 5.5eV the V-3d states of e_g symmetry form a broad band. The energy difference between the t_{2g} and e_g band centers of gravity indicates a clear separation of those bands. Therefore, it is legitimate to consider *only* the partially filled triply degenerated t_{2g} bands, lying in the energy window from -1.5 to 2.0 eV, for the DMFT calculation.

Subsequently, these strongly correlated subbands are projected to localized Wannier functions with WIEN2WANNIER [92]. The DOS of the t_{2g} Wannier functions (per orbital and spin) is shown in the right graph of figure 5.3. The number of \mathbf{k} -points was set to 9261, because this number is a good tradeoff between sufficiently enough points for an accurate representation of the DFT DOS and an acceptable computational cost for the \mathbf{k} -summation required by equation 2.51.³⁶

The t_{2g} orbitals are effectively described by the multi-orbital Hamiltonian 2.2. The required Coulomb interaction and Hund's coupling were determined to $U = 4.0$ eV, $J = 0.6$ eV, $U' = U - 2J = 2.8$ eV (see also reference [85]).

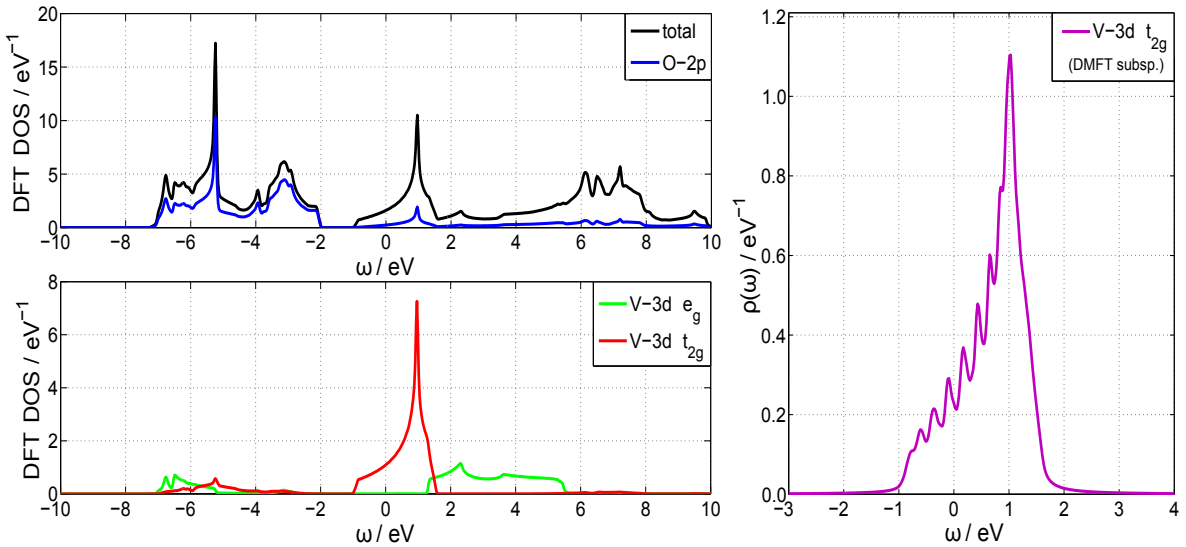


Figure 5.3.: Upper left: Total DFT DOS of SrVO₃ (black) and O-2p contribution (blue). Lower left: Partial DOS of V-3d t_{2g} (red) and e_g (green) orbitals. Right: DOS (per orbital and spin) of the t_{2g} Wannier functions in the subspace from -1.5 to 2.0 eV with 9261 \mathbf{k} -points. Calculations were performed with WIEN2K and WIEN2WANNIER.

³⁵The DFT calculation with WIEN2K and the projection to localized Wannier orbitals with WIEN2WANNIER was performed by Markus Aichhorn.

³⁶Evaluating equation 2.51 requires one loop over all z -points and one *nested* loop over all \mathbf{k} -points.

5.2. DMFT calculation setup

Considering *three* t_{2g} orbitals as subspace for DMFT demands 3×3 self-energy and Green's functions matrices.³⁷ However, in the case of SrVO₃ the self-energy matrix $\Sigma_{mm'}(z)$ is diagonal in the orbital indices and even orbital independent

$$\Sigma_{mm'}(z) = \delta_{mm'}\Sigma(z), \quad (5.1)$$

which means that the self-energy can be still treated as a vector $\Sigma(z)$ – like in the one-orbital case. The impurity model (figure 5.4) consists of three interacting sites, where each one is coupled to a semi-infinite bath chain. Due to the orbital degeneracy each bath chain must have the same parameters, which allows for minimizing the cost function 3.3 for one chain only. Because of those computational simplifications SrVO₃ serves as a popular material for testing numerical implementations of multi-orbital impurity solvers.

The interacting part (colored box in figure 5.4) is determined by the local part of Hamiltonian 2.2 with the parameters (U, J and J') given above. Dealing with the impurity system itself remains a multi-orbital problem and when using ED/CPT λ as impurity solver, three times less bath sites per orbital are feasible in comparison to the single-band system discussed in the previous chapter.

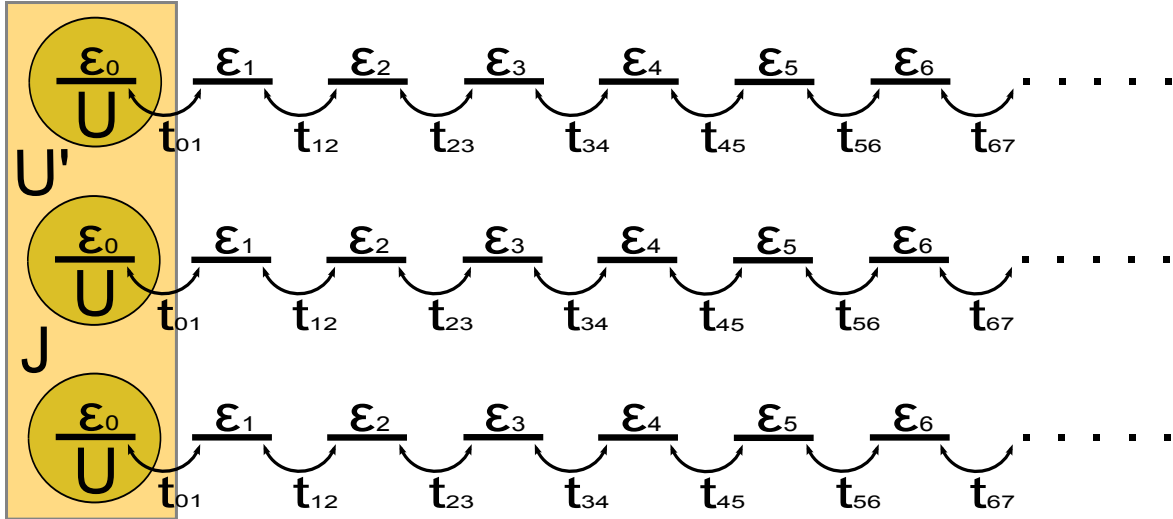


Figure 5.4.: AIM for SrVO₃. Each orbital is coupled to an infinite bath chain. Due to the degeneracy of the three orbitals the bath chains must have the same parameters.

³⁷The matrices are actually of size 6×6 including the spin degrees of freedom.

The results shown in section 5.3 were obtained by one-shot DFT+DMFT calculations on the real frequency axis with $4 \cdot 10^3$ ω -points between -20 and 20eV . The numerical broadening was set to $\eta = 0.05\text{eV}$. To ensure a filling of $1/6$, i.e. one electron per atom, the chemical potential was adjusted after every 7th iteration. The DMFT self-consistency loop was considered as converged if the integrated absolute change of the bath Green's function $\mathcal{G}_0(\omega)$ between two consecutive iterations was smaller than $5 \cdot 10^{-4}$ and the absolute error of the filling less than 10^{-3} . CPT λ was performed with $\lambda = 0.8$. Note that all shown quantities are per orbital and per spin.

5.3. DMFT results

First, we discuss the self-energy on the Matsubara axis $\Sigma(i\omega)$ depicted in figure 5.5, where the ED and CPT λ results for $L = 6$ and $L = 9$ are compared to the self-energy obtained with CTQMC ($\beta = 50\text{eV}^{-1}$). We want to emphasize that the DMFT loop itself is performed on the *real-frequency* axis and only the final result is shown for Matsubara frequencies. As real and constant contributions can either come from the chemical potential μ or the real part of the Matsubara self-energy $\Re[\Sigma(i\omega)]$, we plot the difference of those two quantities.

Regarding the imaginary part of the self-energy first (see upper panel in figure 5.5), we observe that ED predicts a too metallic solution in comparison to CTQMC, but already CPT λ ($L = 6$) lies much closer to CTQMC than ED $L = 9$. The imaginary part of the CPT λ self-energies resembles the CTQMC curve remarkably well and provides the correct behavior for both low and high Matsubara frequencies. Surprisingly, CPT λ ($L = 9$) is in accordance with CTQMC below 1eV and above 4eV . As we expected for both impurity solvers, the self-energy improves when an additional bath site is added to each orbital.

A very similar behavior is found when regarding the real part of the self-energy (lower panel of figure 5.5). ED ($L = 6$) predicts a too low real part, but again the result does improve for $L = 9$. Except for the lowest Matsubara frequencies, CPT λ ($L = 9$) lies almost on top of the CTQMC result. In the case of the Hubbard model, the Fermi liquid theory states $\Sigma(0) - \mu = 0$ [93]. However, the values at $\omega = 0$ for ED and CPT λ are slightly shifted away from zero.

Overall, the CPT λ result shows a very good agreement with the CTQMC data and clearly outperforms ED. Of course, the satisfying low frequency behavior of the self-energy gets also reflected in the quasiparticle weight Z , which is listed in table 5.3 for all used methods and a ARPES measurement [86]. ED overestimates Z , but CPT λ provides a quasiparticle weight very close to CTQMC, and more importantly, within the errors of the experimental reference value.

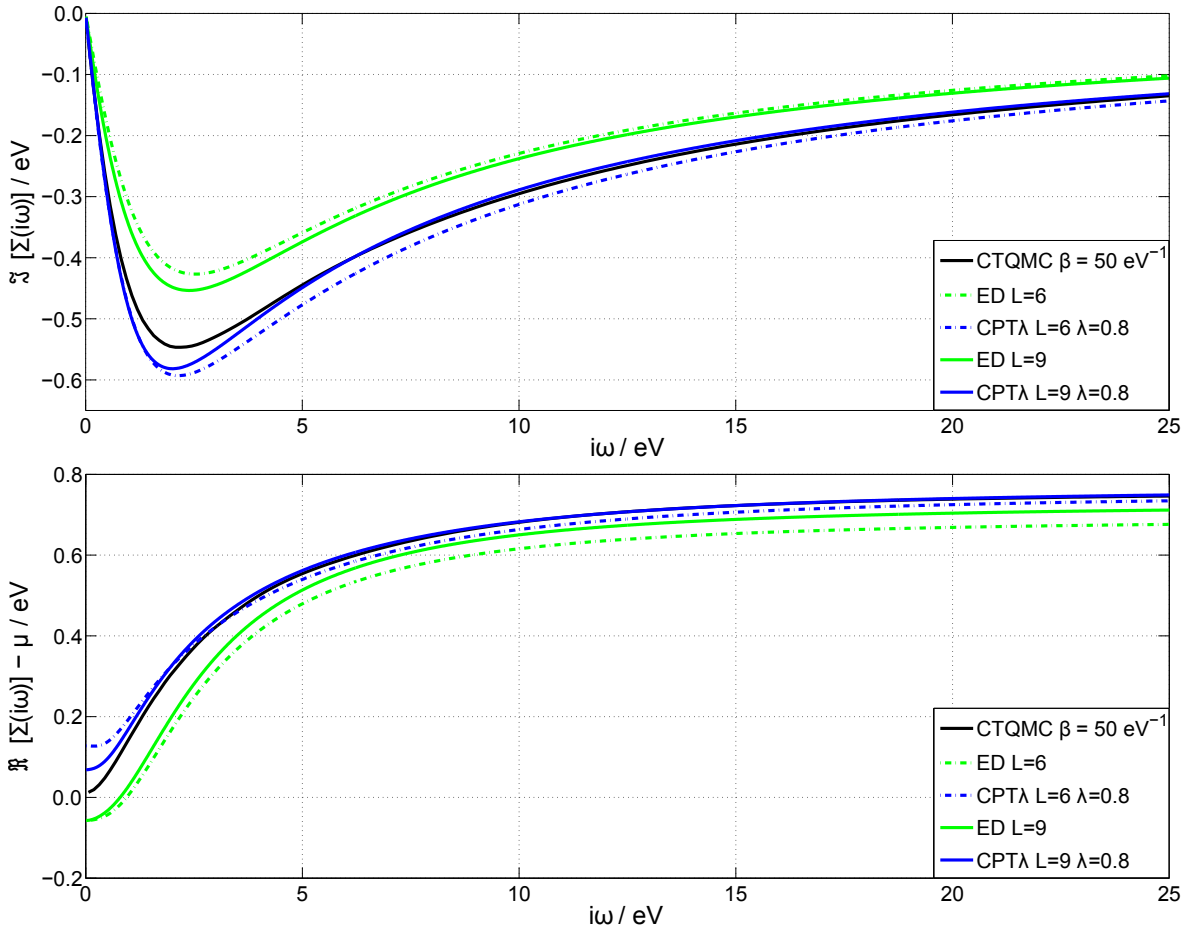


Figure 5.5.: Imaginary part (upper panel) and real part (lower panel) of $\Sigma(i\omega) - \mu$. Calculations were performed for ED (green) and CPT λ (blue) with a system size of $L = 6$ (dotted) and $L = 9$ (solid). Results are compared to CTQMC (black) with $\beta = 50 \text{ eV}^{-1}$.

	ED $L = 6$	ED $L = 9$	CPT λ $L = 6$	CPT λ $L = 9$	CTQMC	ARPES
Z	0.72	0.67	0.59	0.60	0.62	0.56 ± 0.06

Table 5.1.: Quasiparticle weight Z listed for ED, CPT λ , CTQMC and a ARPES experiment [86].

In figure 5.6 the DOS, i.e. $-1/\pi \Im G_{loc}(\omega)$, and the real part of $G_{loc}(\omega)$ are presented. Since the electron filling is only $1/6$, the spectra are strongly asymmetric, with the maximum of the quasiparticle peak at about 0.55 eV above the Fermi energy. Roughly half of the spectral weight is accounted for by the quasiparticle peak. The remaining weight is divided into the two Hubbard bands, whereby the upper Hubbard band contributes $\sim 40\%$ to the overall weight and the lower Hubbard band less than $\sim 10\%$.

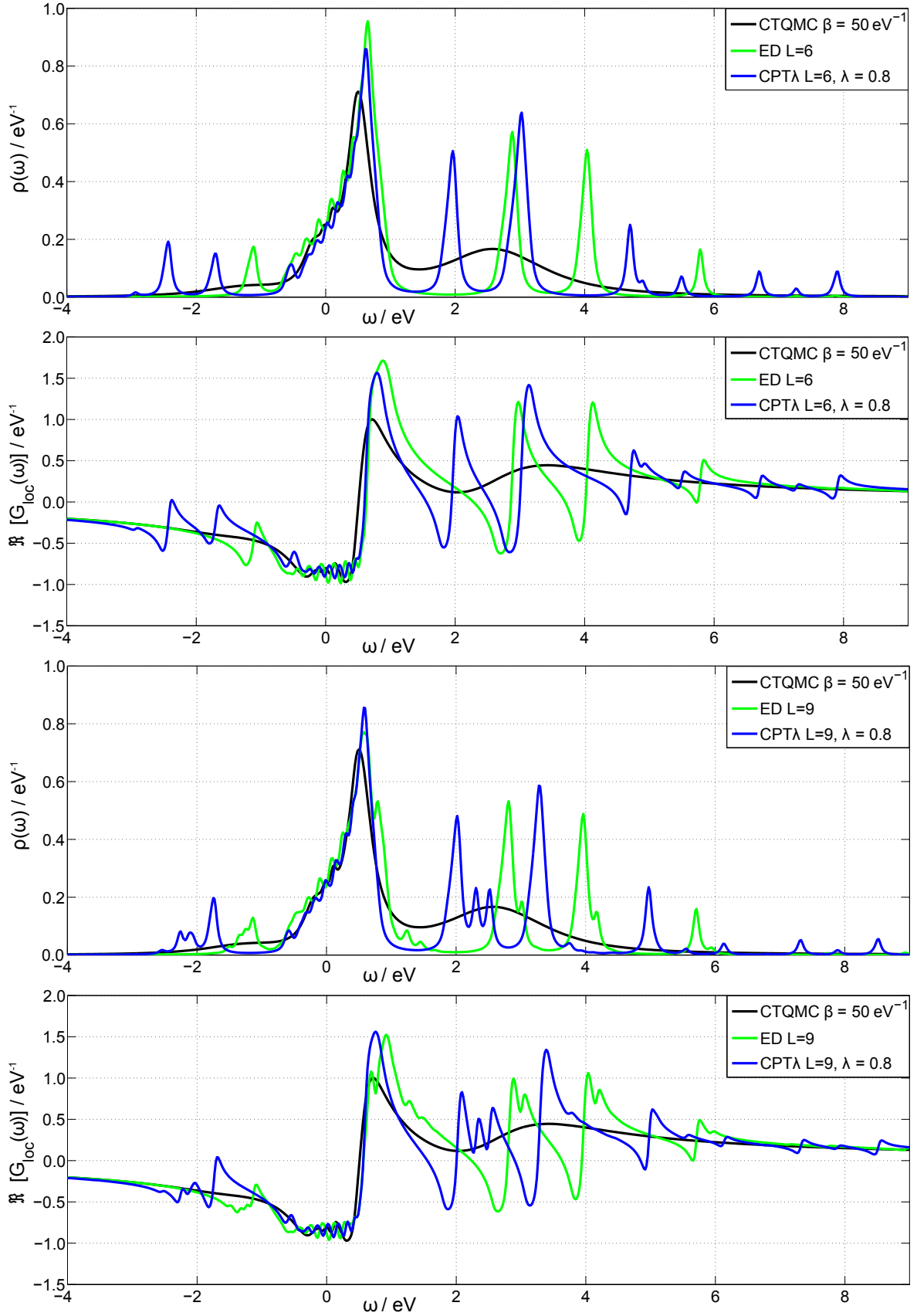


Figure 5.6.: DOS $\rho(\omega)$ and the real part of $G_{loc}(\omega)$ for ED (green) and CPT λ (blue) with a cluster size of $L = 6$ (upper two panels) and $L = 9$ (lower two panels) compared to CTQMC ($\beta = 50 \text{ eV}^{-1}$).

The heavily peaked structure of the Hubbard bands of the ED and CPT λ spectra is due to finite-size effects stemming from the impurity cluster. Increasing the cluster size to $L = 9$ does reveal a few additional details, but it does not provide much further information on the position and shape of the Hubbard bands.³⁸

It should be emphasized that the CTQMC calculation is a method working on the Matsubara axis, thus an analytic continuation is necessary to obtain the spectral information on the real axis. The statistical noise in the simulation data turns the analytic continuation into an ill-posed problem. This means that small changes on the Matsubara axis can have a strong effect on the resulting DOS and thus heavily influence the shape and position of the Hubbard bands. Usually, the analytic continuation is done with the Padé approximation [94] or a maximum entropy method [95]. The advantage of our cluster based method is that real-frequency observables are *directly* available from the calculations without any further approximations.

For an impurity cluster of 9 sites the central quasiparticle peak is slightly narrowed and shifted towards lower frequencies in comparison to the 6 site cluster. Especially for CPT λ ($L = 9$), the central part of the spectrum shows a remarkable agreement with the CTQMC DOS. Also the upper Hubbard band of the CPT λ result exhibits a better accordance to the CTQMC band in comparison to ED. The latter shows a huge gap between 1.7 and 2.3eV with the first ED peak of the upper Hubbard band placed not before 2.8eV, which is even beyond the maximum of the CTQMC band.

It seems that CPT λ places the lower Hubbard band at too low energies. However, the lower Hubbard band of the CTQMC DOS is rather flat and has a long tail towards lower frequencies.³⁹ While the shape of the CPT λ band is not in accordance with the CTQMC result, the central point of gravity is estimated better than by ED. This statement is underlined below by the comparison of the first moments of the DOS. It should be mentioned that other DFT+DMFT results [84] suggest a lower Hubbard band centered around -2eV , but those calculations were performed with larger parameter values for the local Hamiltonian ($U = 5.5\text{eV}$ and $J = 1.0\text{eV}$).

In general, the real part of $G_{loc}(\omega)$ does follow the CTQMC result, but possesses jumps (discontinuities) exactly at the frequencies of the peaks occurring in the DOS. The real and imaginary part of $G_{loc}(\omega)$ essentially contain the same information, because they are connected via the Kramers-Kroning relation [27].

To compare the spectra on the real axis in more detail the integrated spectral weights

$$F_0(\omega) = \int_{-\infty}^{\omega} d\omega' \rho(\omega') \quad \text{and} \quad F_1(\omega) = \int_{-\infty}^{\omega} d\omega' \omega' \rho(\omega'), \quad (5.2)$$

³⁸Cluster sizes far beyond the computational limit would be necessary to achieve a smoother DOS.

³⁹Those are most likely effects of the analytic continuation.

which are the zeroth (left) and first (right) moment of the DOS $\rho(\omega)$ are plotted in figure 5.7.

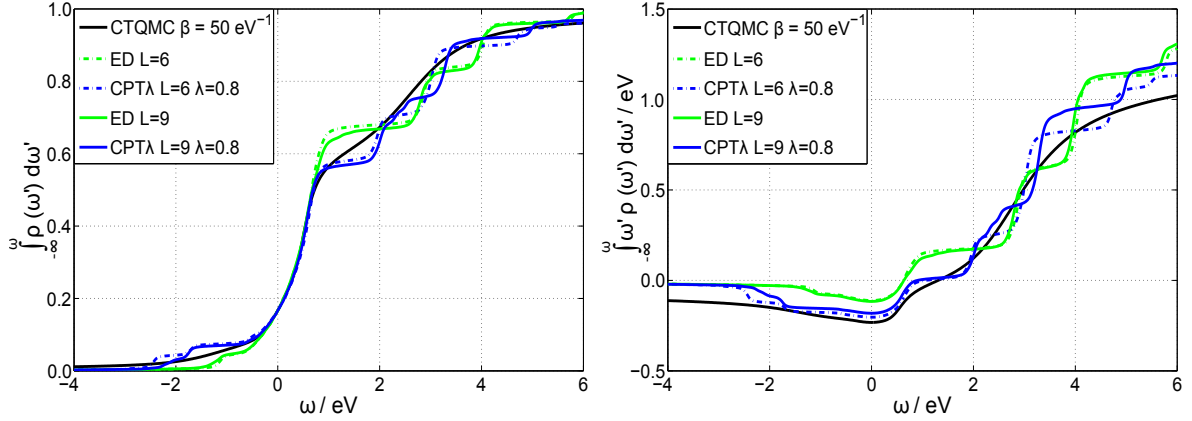


Figure 5.7.: Cumulative zeroth (left) and the first (right) moment of the DOS $\rho(\omega)$ for ED (green) and CPT λ (blue) compared to CTQMC (black).

The zeroth moments of ED/CPT λ show a remarkably good agreement with the integrated weight of the CTQMC DOS in the important frequency range from about -1 to 1 eV. Outside this range the zeroth moment is slightly better reproduced by CPT λ . Regarding the first moment, we note that CPT λ is in reasonable accordance with CTQMC over the whole energy range. From the first moment between -2.5 and 0.0 eV, we can conclude that the lower Hubbard band is located such that its central point of gravity is estimated better by CPT λ . The steps in the moments of the ED/CPT λ DOS are caused by the peaks in their spectra.

In figure 5.8 the spectral functions $A(\mathbf{k}, \omega)$ for the \mathbf{k} -path $\Gamma(0, 0, 0) \rightarrow X(0, \pi, 0) \rightarrow M(\pi, \pi, 0) \rightarrow \Gamma(0, 0, 0)$ are shown for DFT (left) and DMFT with CPT λ ($L = 9$) as impurity solver (right). The spectral functions were obtained for the given \mathbf{k} -path by evaluating equation 2.51, but without performing the \mathbf{k} -summation. Note that only the strongly correlated t_{2g} subbands of the DFT spectral function, which we treated within DMFT, are plotted.

In the DMFT dispersion the quasiparticle peak in the region between -1 and 1 eV and the two Hubbard bands are well pronounced. The peaked structure of the bands is also reflected in the spectral function. Overall, the Hubbard bands have a rather flat dispersion, whereby the lower band has its main weight around -2 eV and the upper band between 1.5 and 3.5 eV (see also the DOS for CPT λ ($L = 9$) in figure 5.6). The DFT t_{2g} bands are renormalized to about half of the initial DFT width, which is well consistent with the quasiparticle renormalization of $Z = 0.6$.

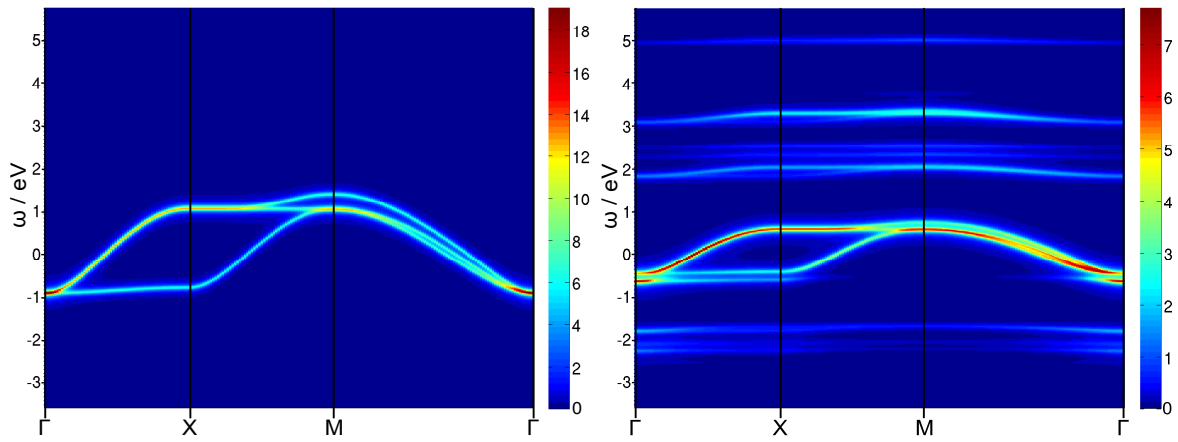


Figure 5.8.: Spectral function $A(\mathbf{k}, \omega)$ for the \mathbf{k} -path $\Gamma(0,0,0) \rightarrow X(0,\pi,0) \rightarrow M(\pi,\pi,0) \rightarrow \Gamma(0,0,0)$. Left: DFT band structure of the t_{2g} subspace around the Fermi energy. Right: DMFT spectral function with CPT λ ($L = 9$) as impurity solver.

6. Conclusions

In this thesis the use of CPT as a real-frequency impurity solver for DMFT was studied. For this purpose, the impurity system was split into a finite cluster containing the impurity site and a semi-infinite non-interacting chain. The coupling between those two systems is treated within CPT. However, CPT is only expected to be reliable as long as the coupling stays small, which was achieved by modifying the cost function for the impurity parameters by introducing an additional parameter λ . With the self-energy as a second figure of merit, we were able to develop a consistent way to determine λ .

This newly developed impurity solver (CPT λ) was first investigated on the infinitely connected Bethe lattice. In contrast to ED/CPT, CPT λ shows a good low and high frequency behavior of the self-energy on the Matsubara axis. Remarkably, CPT λ with an impurity cluster of only four sites provides already a quasiparticle weight very close to NRG comparison data. Although the DOS suffers from finite-size effects and a poor representation of the Hubbard bands, CPT λ yields a qualitatively correct spectrum, especially in the weakly correlated regime. We observe that the spectral weight transfer from the central region around the Fermi energy to the Hubbard bands with increasing interaction strength is well reproduced. Noteworthy, all three impurity solvers (ED, CPT and CPT λ) provide a proper estimation of the phase transition point.

To allow a faster and more stable convergence to the DMFT fixed-point we implemented Broyden's method as mixing scheme. It turns out that this advanced approach works best if mixing is performed in the self-energy.

As final part of this work, our impurity solver was tested in the framework of DFT+DMFT on the strongly correlated paramagnetic material SrVO₃. The splitting of the DFT spectrum into the characteristic three peaked structure consisting of the quasiparticle peak and the two Hubbard bands is well pronounced. CPT λ yields a very accurate representation of the spectrum around the Fermi energy (i.e. the quasiparticle peak) and thus a quasiparticle weight within the errors of available experimental data. Despite the strongly peaked structure of the Hubbard bands, we observe a reasonably good distribution of the spectral weight, which is confirmed by the comparison of the DOS itself and its zeroth and first moments to data obtained with CTQMC.

In general, calculations performed with CPT λ as real-frequency impurity solver do provide qualitatively better results than ED. This concerns in particular the position of the Hubbard bands and the central quasiparticle weight. Of course, the resulting spectra can not measure up with those provided by impurity solvers like NRG, MPS or CTQMC, but CPT λ offers a fast and widely applicable way to obtain good estimates before applying one of the more advanced methods.

Solvers based on ED/CPT can in principle be used on the imaginary or the real-frequency axis and do not suffer from restrictions like the sign-problem or the ill-posed analytic continuation for numerical data. The low computational demand would make them suitable for charge self-consistent DFT+DMFT or total energy calculations of multi-orbital systems. The results for SrVO₃ with only 1 and 2 bath sites per orbital are promising, but of course CPT λ needs to be tested for other strongly correlated materials and in situations with lower symmetry than in the perfectly cubic case of SrVO₃.

A. Matsubara Green's function

This brief introduction to Matsubara Green's functions is based on the books [27, 28], whereby more on the Green's function theory can be found therein. Here, we start with the definition of the Matsubara (imaginary-time) single-particle Green's function

$$G_{\nu\nu'}(\tau, \tau') \equiv -\langle T_\tau c_\nu(\tau), c_{\nu'}^\dagger(\tau') \rangle, \quad (\text{A.1})$$

where τ and τ' are real parameters satisfying $0 < \tau$ and $\tau' < \beta$ with $\beta = 1/T$.⁴⁰ T_τ is the time ordering operator which puts the operators c and c^\dagger in a chronological order. The time evolution of the operators is defined as the usual real-time evolution

$$c(\tau) \equiv e^{H\tau} c e^{-H\tau} \quad \text{and} \quad c^\dagger(\tau) \equiv e^{H\tau} c^\dagger e^{-H\tau}, \quad (\text{A.2})$$

but setting $it = \tau$, which is called Wick rotation. As for the retarded Green's function (introduced in section 2.2), a time-independent Hamiltonian results in a Green's function dependent only on the time difference $\tau - \tau'$, with $-\beta < \tau - \tau' < \beta$ to guarantee the convergence of equation A.1. Using the cyclic properties of the trace the anti-periodicity of the Matsubara Green's function

$$G(\tau) = -G(\tau + \beta) \quad \text{for} \quad \tau < 0, \quad (\text{A.3})$$

can be shown and thus the Matsubara Green's function is periodic in 2β . Due to these properties, the Fourier transformation of the imaginary-time Green's function $G(\tau)$ leads to a *discrete* imaginary-frequency Green's function $G(i\omega_n)$ defined at the (fermionic) Matsubara frequencies

$$\omega_n = \frac{(2n + 1)\pi}{\beta} \quad (\text{A.4})$$

Note that the Matsubara frequencies are directly connected to a finite temperature.⁴¹ Beside poles or branch cuts on the real axis, the Green's function $G(z)$ is analytic in both the upper and lower complex plane. According to the theory of analytic functions, two functions are fully identical if they coincide in an infinite number of

⁴⁰The Boltzmann constant k_B is set to 1.

⁴¹For $T = 0$ the Matsubara frequencies become continuous.

points. This means that the Matsubara Green's function can be analytically continued from Matsubara frequencies to the real axis by substituting $i\omega \rightarrow \omega + i\eta$. However, this is only possible if an analytic expression of the Green's function, like the Lehmann representation (equation 3.19), is available. Otherwise, e.g. in the case of numerical data, the analytic continuation turns out to be an ill-posed problem.

To evaluate equation 3.37 we need to Fourier transform the Matsubara Green's function $G(i\omega_n)$ from the frequency domain $i\omega_n$ to imaginary times τ . Some consideration are necessary to numerically perform this transformation in an efficient and proper way. The following elaborations are based on the lecture notes [96] and outlined for a non-interacting Green's function, but are also valid in the interacting case. The Fourier transformation of the discrete Matsubara frequencies is defined as

$$G_0(\tau) = \frac{1}{\beta} \sum_{n=-\infty}^{\infty} G_0(i\omega_n) e^{-i\omega_n\tau} = \frac{1}{\beta} \sum_{n=-N}^{N-1} G_0(i\omega_n) e^{-i\omega_n\tau} + G_0^T(\tau), \quad (\text{A.5})$$

where the first part can be evaluated numerically only for a finite number of $2N$ points. Not treating the truncation $G_0^T(\tau)$ straightforwardly would require a large number of Matsubara frequencies. Therefore, we shall take a look at the asymptotic behavior of $G_0(i\omega_n)$

$$\begin{aligned} G_0(i\omega_n) &= \int d\epsilon \frac{\rho_0(\epsilon)}{i\omega_n - \epsilon} = \int d\epsilon \rho_0(\epsilon) \left(-\frac{\epsilon}{\omega_n^2 + \epsilon^2} - \frac{i\omega_n}{\omega_n^2 + \epsilon^2} \right) \approx \\ &\approx -\frac{1}{\omega_n^2} \int d\epsilon \rho_0(\epsilon) \epsilon - \frac{i}{\omega_n} \int d\epsilon \rho_0(\epsilon) = -\frac{\epsilon_B}{\omega_n^2} - \frac{i}{\omega_n} \approx -\frac{i}{\omega_n}, \end{aligned} \quad (\text{A.6})$$

where ϵ_B is the band center of mass energy. With this approximation for large Matsubara frequencies it is possible to derive an expression for $G_0^T(\tau)$.

$$\begin{aligned} G_0^T(\tau) &= \frac{1}{\beta} \sum_{n=-\infty}^{-N-1} G_0(i\omega_n) e^{-i\omega_n\tau} + \frac{1}{\beta} \sum_{n=N}^{\infty} G_0(i\omega_n) e^{-i\omega_n\tau} = \\ &= \frac{1}{\beta} \sum_{n=N}^{\infty} [G_0(i\omega_n) e^{-i\omega_n\tau} + G_0(-i\omega_n) e^{i\omega_n\tau}] \approx \\ &\approx -\frac{i}{\beta} \sum_{n=N}^{\infty} \frac{1}{\omega_n} [e^{-i\omega_n\tau} - e^{i\omega_n\tau}] = -\frac{2}{\beta} \sum_{n=N}^{\infty} \frac{\sin(\omega_n\tau)}{\omega_n} = \\ &= -\frac{2}{\beta} \sum_{n=0}^{\infty} \frac{\sin(\omega_n\tau)}{\omega_n} + \frac{2}{\beta} \sum_{n=0}^{N-1} \frac{\sin(\omega_n\tau)}{\omega_n} = \\ &= -\frac{2}{\pi} \sum_{n=0}^{\infty} \frac{\sin\left((2n+1)\frac{\pi\tau}{\beta}\right)}{2n+1} + \frac{2}{\beta} \sum_{n=0}^{N-1} \frac{\sin(\omega_n\tau)}{\omega_n} = \\ &= -\frac{1}{2} \text{sign}(\tau) + \frac{2}{\beta} \sum_{n=0}^{N-1} \frac{\sin(\omega_n\tau)}{\omega_n} \end{aligned} \quad (\text{A.7})$$

Putting together equation A.5 and A.7 gives the final expression for the Fourier transformation

$$G_0(\tau) = \frac{1}{\beta} \sum_{n=-N}^{N-1} G_0(i\omega_n) e^{-i\omega_n\tau} - \frac{1}{2} \text{sign}(\tau) + \frac{2}{\beta} \sum_{n=0}^{N-1} \frac{\sin(\omega_n\tau)}{\omega_n}, \quad (\text{A.8})$$

but now including an asymptotic tail correction. If the Fourier transformation is carried out several times, the second and third term need to be calculated only once, because they are independent of $G_0(i\omega_n)$. To capture the physics correctly it is necessary to choose N large enough to ensure being close to the high frequency asymptote $\approx \frac{1}{i\omega_n}$.

B. Broyden's Method for DMFT

A more advanced mixing approach is the so-called Broyden's method, which incorporates the knowledge of the self-energy $\Sigma(z)$ change over all previous iterations. To stay within the scope of this thesis, only the resulting equations given in the publication [37] are stated. Additional details on the derivation can be found in the references therein. The same considerations hold also for mixing performed in other quantities (e.g. $\mathcal{G}_0(z)$).

First we rewrite equation 2.29 from section 2.5

$$\tilde{\mathcal{F}}[\hat{\Sigma}(z)] = \mathcal{F}[\hat{\Sigma}(z)] - \hat{\Sigma}(z) = 0, \quad (\text{B.1})$$

where the roots $\hat{\Sigma}(z)$ of the mapping $\tilde{\mathcal{F}}$ correspond to the DMFT fixed-points. Basically, Broyden's method is a quasi-Newton-Raphson method and aims at finding precisely those roots.

The mixed self-energy after the N th iteration is given by

$$\Sigma^{N+1}(z) = \Sigma^N(z) - (\mathbf{J}^N)^{-1} \tilde{\Sigma}^N(z), \quad (\text{B.2})$$

where $\Sigma^N(z)$ is the mixed self-energy after the $(N-1)$ th step and $\tilde{\Sigma}^N(z) = \tilde{\mathcal{F}}[\Sigma^N(z)]$ the difference between $\Sigma^N(z)$ and the self-energy resulting from one DMFT iteration with $\Sigma^N(z)$ as input. The true Jacobian matrix $(\mathbf{J}^N)^{-1}$ of the system is unknown, thus a simple approximation (i.e. a diagonal matrix) is used for the initial Jacobian.⁴² Incorporating the information of all previous iterations to update the current Jacobian matrix and simplifying the computational scheme so that only the vectors $\tilde{\Sigma}^N(z)$ and $\Sigma^N(z)$ need to be stored, leads finally to the (modified) Broyden method

$$\Sigma^{N+1}(z) = \Sigma^N(z) + \alpha \tilde{\Sigma}^N(z) - \sum_{n=1}^{N-1} \sum_{k=1}^{N-1} c_k^N \beta_{k,n}^N U^n(z) \quad (\text{B.3})$$

with

$$c_k^N = \left(\Delta \tilde{\Sigma}^k(z) \right)^\dagger \tilde{\Sigma}^N(z), \quad U^n(z) = \alpha \Delta \tilde{\Sigma}^n(z) + \Delta \Sigma^n(z) \quad (\text{B.4})$$

⁴²Using $-\frac{1}{\alpha} \mathbb{1}$ as initial Jacobian corresponds to simple mixing.

and the matrices

$$\beta_{k,n}^N = \left[(\omega_0^2 \mathbf{1} + \mathbf{A}^N)^{-1} \right]_{k,n}, \quad A_{k,n}^N = \left(\Delta \tilde{\Sigma}^n(z) \right)^\dagger \Delta \tilde{\Sigma}^k(z). \quad (\text{B.5})$$

The quantities $\Delta \tilde{\Sigma}^N(z)$ and $\Delta \Sigma^N(z)$ are the normalized differences between consecutive iterations

$$\Delta \Sigma^N(z) = \frac{\Sigma^{N+1}(z) - \Sigma^N(z)}{|\tilde{\Sigma}^{N+1}(z) - \tilde{\Sigma}^N(z)|}, \quad \Delta \tilde{\Sigma}^N(z) = \frac{\tilde{\Sigma}^{N+1}(z) - \tilde{\Sigma}^N(z)}{|\tilde{\Sigma}^{N+1}(z) - \tilde{\Sigma}^N(z)|}. \quad (\text{B.6})$$

The first two terms of equation B.3 correspond to simple mixing with parameter α . The last term is a correction, which accounts for the updates of the initial Jacobian. According to reference [37] the weight ω_0 should be chosen to 0.01.

Implementing Broyden's method (equations B.3 to B.6) into the DMFT cycle is straight forward and the added computational expenses turn out to be very low. In practice, it is advisable to

- use a thermalization period of a few iterations (~ 10) without mixing
- and to restart the mixing after some iterations ($\sim 10 - 20$),

to avoid an incorporation of solutions which are far from the actual one (e.g. due to a poor initial guess).

C. Generation of basis states with HAKMEM #175

This code snippet is adapted from reference [60].

```
1 void permutations(int initial, int nr, std::vector<int> &st)
2     //This function generates the lowest nr permutations
3     //of the initial bit pattern
4
5     unsigned int x = initial;
6     unsigned int u;
7     unsigned int v;
8
9     st.reserve(nr);
10    st.push_back(x);
11    for(unsigned int i = 1; i < nr; i++)
12    {
13        u = x & -x;
14        v = u + x;
15        x = v + ((v^x)/u)>>2);
16        st.push_back(x);
17    }
18 }
```

D. Q-matrix formalism

The Lehmann representation of the Green's function, where we omit a possible degeneration of the ground state $|\psi_0\rangle$, reads

$$G_{\nu\nu'}(z) = \sum_n \frac{\langle \psi_0 | c_\nu | \psi_n \rangle \langle \psi_n | c_{\nu'}^\dagger | \psi_0 \rangle}{z - (E_n - E_0)} + \sum_m \frac{\langle \psi_0 | c_{\nu'}^\dagger | \psi_m \rangle \langle \psi_m | c_\nu | \psi_0 \rangle}{z + (E_m - E_0)}. \quad (\text{D.1})$$

The idea of the Q -matrix formalism (first suggested in [97]) is to write the occurring sums in the Lehmann representation in terms of a convenient matrix multiplication

$$G_{\nu\nu'}(z) = \sum_\gamma Q_{\nu\gamma} \frac{1}{z - \lambda_\gamma} Q_{\gamma\nu'}^\dagger = Q \Lambda(z) Q^\dagger, \quad (\text{D.2})$$

with the Q -matrix of dimension $N_\gamma \times L$

$$Q_{i\gamma} \equiv \begin{cases} \langle \psi_0 | c_\nu | \psi_\gamma \rangle, & \text{for } \gamma \in N + 1 \\ \langle \psi_\gamma | c_\nu | \psi_0 \rangle, & \text{for } \gamma \in N - 1 \end{cases} \quad (\text{D.3})$$

and the diagonal Λ -matrix of dimension $N_\gamma \times N_\gamma$

$$\Lambda_{\gamma\gamma'}(z) \equiv \frac{\delta_{\gamma\gamma'}}{z - \lambda_\gamma}, \quad \text{where } \lambda_\gamma \equiv \begin{cases} E_\gamma - E_0, & \text{for } \gamma \in N + 1 \\ E_0 - E_\gamma, & \text{for } \gamma \in N - 1 \end{cases}. \quad (\text{D.4})$$

The matrix Q comprehends the weights of all excitations, whereby the matrix Λ is the only z -dependent quantity left. This means that the full information embedded in the Green's function can be stored in a single matrix Q and one vector λ_γ . From the computational point of view this formalism is beneficial, because it allows for evaluating equation D.2 for any z be it on the real or the imaginary axis.

The sum-rule given by equation 2.7 transferred to the Q -matrix formalism yields

$$Q Q^\dagger = \mathbb{1}. \quad (\text{D.5})$$

Usually, many excited states contribute with very little weight to the Green's function. Those excitations can be deleted from λ_γ as well as from the corresponding columns in the Q -matrix. Still, it is important to fulfill the sum-rule D.5, ensuring no observable

effect caused by reducing the dimensionality of Q . Throwing out all negligible excitations reduces the computational cost of evaluating equation D.2, which is typically done for many z -values to obtain a full frequency dependent Green's function.

E. Motivating the CPT equation

As starting point we consider the Dyson's equation for both the full system

$$\mathbf{G}^{-1}(z) = \mathbf{G}_0^{-1}(z) - \Sigma(z) \quad (\text{E.1})$$

and the cluster only

$$\mathbf{G}'^{-1}(z) = \mathbf{G}'_0^{-1}(z) - \Sigma'(z), \quad (\text{E.2})$$

where primes mark cluster quantities. CPT is based on approximating the self-energy of the full system $\Sigma(z)$ by the self-energy of the cluster $\Sigma'(z)$ only [55]. Thus we obtain within CPT

$$\begin{aligned} \mathbf{G}^{-1}(z) &= \mathbf{G}_0^{-1}(z) - \Sigma(z) \approx \mathbf{G}_0^{-1}(z) - \Sigma'(z) = \\ &= \mathbf{G}_0^{-1}(z) - \mathbf{G}'_0^{-1}(z) + \mathbf{G}'^{-1}(z). \end{aligned} \quad (\text{E.3})$$

In the last step the self-energy $\Sigma'(z)$ was substituted with the self-energy from equation E.2. Expressing the non-interacting Green's functions in terms of the single-particle Hamiltonians \mathbf{H}_0 and \mathbf{H}'_0

$$\begin{aligned} \mathbf{G}^{-1}(z) &= \mathbf{G}'^{-1}(z) + (z\mathbb{1} - \mathbf{H}_0) - (z\mathbb{1} - \mathbf{H}'_0) \\ &= \mathbf{G}'^{-1}(z) - (\mathbf{H}_0 - \mathbf{H}'_0) = \mathbf{G}'^{-1}(z) - \mathbf{T}, \end{aligned} \quad (\text{E.4})$$

leads finally to the CPT equation as stated in equation 3.25. The matrix \mathbf{T} contains exactly the terms which are not present in the cluster Hamiltonian \mathbf{H}'_0 and that are the inter-cluster hoppings.

List of Abbreviations

ARPES	Angle-Resolved Photoemission Spectroscopy
AIM	Anderson Impurity Model
CTQMC	Continuous-Time Quantum Monte Carlo
CPT	Cluster Perturbation Theory
ED	Exact Diagonalization
DOS	Density Of States
DFT	Density Functional Theory
DMFT	Dynamical Mean Field Theory
DMRG	Density Matrix Renormalization Group
HFQMC	Hirsch-Fye Quantum Monte Carlo
IPT	Iterative Perturbation Theory
LDA	Local-Density Approximation
MPS	Matrix Product States
NCA	Non-Crossing Approximation
NRG	Numerical Renormalization Group
VCA	Variational Cluster Approximation

List of Figures

2.1. 2D Hubbard model.	4
2.2. Mapping to an effective impurity problem.	8
2.3. Temporal correlations on the impurity.	8
2.4. AIM in star geometry.	9
2.5. DMFT self-consistency cycle.	13
2.6. Mott-Hubbard transition on the Bethe lattice.	16
2.7. Phase diagram of the Bethe lattice.	17
3.1. AIM in chain geometry.	23
3.2. Finite AIM of size $L = 6$	24
3.3. Tiling of a lattice into finite clusters.	34
3.4. Division of the impurity model into a cluster and a non-interacting chain.	35
3.5. Contributions to the cost function $\chi_{CPT\lambda}$	39
3.6. Hypothetical behaviors of $\Delta\Sigma(\lambda)$	40
3.7. Comparison of $\Sigma_{PT}(i\omega_n, \lambda)$ and $\Sigma_{CLPT}(i\omega_n, \lambda)$ for different λ	42
3.8. $\Delta\Sigma(\lambda)$ for cluster sizes of $L = 2, 4, 6$ and 8	43
4.1. Bethe lattice with coordination number $q = 4$	45
4.2. Semicircular non-interacting DOS of the Bethe lattice.	46
4.3. Convergence of different mixing schemes for CPT λ	49
4.4. Comparison of $G_{loc}(\omega)$ and $g(\omega)$	50
4.5. Imaginary part of the Matsubara self-energy.	52
4.6. Real part of the Matsubara self-energy.	53
4.7. $\Im\Sigma(i\omega)$ as a function of the Coulomb interaction U/D	54
4.8. Quasiparticle weight Z over U/D	54
4.9. Convergence of the quasiparticle weight with cluster size.	55
4.10. Quasiparticle weight around the phase transition.	56
4.11. Imaginary part of the real-frequency self-energy.	57
4.12. DOS for a cluster of size $L = 4$	60
4.13. DOS for a cluster of size $L = 8$	61
4.14. Dependence of the DOS on the broadening η	62
4.15. DOS obtained with CPT λ ($L = 10$).	63
4.16. Evolution of the DOS for CPT λ ($L = 10$).	63

4.17. Evolution of the DOS for CPT λ ($L = 8$).	64
5.1. SrVO ₃ crystal structure.	66
5.2. 3 <i>d</i> -orbitals and crystal-field splitting.	66
5.3. DFT DOS of SrVO ₃	67
5.4. AIM for SrVO ₃	68
5.5. Matsubara self-energy.	70
5.6. DOS and real part of $G_{loc}(\omega)$	71
5.7. Cumulative zeroth and first moment of the DOS.	73
5.8. Spectral function $A(\mathbf{k}, \omega)$	74

Bibliography

- [1] P. A. Lee, N. Nagaosa, and X.-G. Wen. Doping a Mott insulator: Physics of high-temperature superconductivity. *Rev. Mod. Phys.*, 78:17–85, Jan 2006.
- [2] T. V. Ramakrishnan, H. R. Krishnamurthy, S. R. Hassan, and G. Venketeswara Pai. Theory of Insulator Metal Transition and Colossal Magnetoresistance in Doped Manganites. *Phys. Rev. Lett.*, 92:157203, Apr 2004.
- [3] M. R. Peterson, B. S. Shastry, and J. O. Haerter. Thermoelectric effects in a strongly correlated model for Na_xCoO_2 . *Phys. Rev. B*, 76:165118, Oct 2007.
- [4] W. Kohn. Nobel Lecture: Electronic structure of matter - wave functions and density functionals. *Rev. Mod. Phys.*, 71:1253–1266, Oct 1999.
- [5] U von Barth. Basic Density Functional Theory an Overview. *Phys. Scripta*, 2004(T109):9, 2004.
- [6] J. Hubbard. Electron correlations in narrow energy bands. *Proc. Roy. Soc. A*, 276(1365):238–257, 1963.
- [7] M. J. Rozenberg, G. Kotliar, and X. Y. Zhang. Mott-Hubbard transition in infinite dimensions. II. *Phys. Rev. B*, 49:10181–10193, Apr 1994.
- [8] J. E. Hirsch and S. Tang. Antiferromagnetism in the Two-Dimensional Hubbard Model. *Phys. Rev. Lett.*, 62:591–594, Jan 1989.
- [9] T. Yanagisawa. Physics of the Hubbard model and high temperature superconductivity. *JPCS*, 108(1):012010, 2008.
- [10] W. Metzner and D. Vollhardt. Correlated Lattice Fermions in $d=\infty$ Dimensions. *Phys. Rev. Lett.*, 62:324–327, Jan 1989.
- [11] A. Georges and G. Kotliar. Hubbard model in infinite dimensions. *Phys. Rev. B*, 45:6479–6483, Mar 1992.
- [12] A. Georges. Strongly Correlated Electron Materials: Dynamical Mean Field Theory and Electronic Structure. *AIP Conf. Proc.*, 715(1):3–74, 2004.

- [13] A. Georges, G. Kotliar, W. Krauth, and M. J. Rozenberg. Dynamical mean-field theory of strongly correlated fermion systems and the limit of infinite dimensions. *Rev. Mod. Phys.*, 68:13–125, Jan 1996.
- [14] P. W. Anderson. Localized Magnetic States in Metals. *Phys. Rev.*, 124:41–53, Oct 1961.
- [15] M. Caffarel and W. Krauth. Exact diagonalization approach to correlated fermions in infinite dimensions: Mott transition and superconductivity. *Phys. Rev. Lett.*, 72:1545–1548, Mar 1994.
- [16] D. Sénéchal, D. Perez, and D. Plouffe. Cluster perturbation theory for Hubbard models. *Phys. Rev. B*, 66:075129, Aug 2002.
- [17] D. Sénéchal, D. Perez, and M. Pioro-Ladrière. Spectral Weight of the Hubbard Model through Cluster Perturbation Theory. *Phys. Rev. Lett.*, 84:522–525, Jan 2000.
- [18] M. Potthoff, M. Aichhorn, and C. Dahnken. Variational Cluster Approach to Correlated Electron Systems in Low Dimensions. *Phys. Rev. Lett.*, 91:206402, Nov 2003.
- [19] M. Nuss, E. Arrigoni, M. Aichhorn, and W. von der Linden. Variational cluster approach to the single-impurity Anderson model. *Phys. Rev. B*, 85:235107, Jun 2012.
- [20] M. Nuss. A cluster many body approach to quantum impurity models. *Graz University of Technology*, Master Thesis, 2012.
- [21] V. I. Anisimov, A. I. Poteryaev, M. A. Korotin, A. O. Anokhin, and G. Kotliar. First-principles calculations of the electronic structure and spectra of strongly correlated systems: dynamical mean-field theory. *J. Phys.: Condens. Matter*, 9(35):7359, 1997.
- [22] G. Kotliar, S. Y. Savrasov, K. Haule, V. S. Oudovenko, O. Parcollet, and C. A. Marianetti. Electronic structure calculations with dynamical mean-field theory. *Rev. Mod. Phys.*, 78:865–951, Aug 2006.
- [23] T. Miyake, K. Nakamura, R. Arita, and M. Imada. Comparison of Ab initio Low-Energy Models for LaFePO, LaFeAsO, BaFe₂As₂, LiFeAs, FeSe, and FeTe: Electron Correlation and Covalency. *J. Phys. Soc. Jpn.*, 79(4):044705, 2010.
- [24] Z. Szabó and Z. Gulácsi. Superconductivity in the extended Hubbard model with more than nearest-neighbour contributions. *Philos. Mag. B*, 76(6):911–928, 1997.

- [25] J. E. Han, M. Jarrell, and D. L. Cox. Multiorbital Hubbard model in infinite dimensions: Quantum Monte Carlo calculation. *Phys. Rev. B*, 58:4199, August 1998.
- [26] J. Kanamori. Electron Correlation and Ferromagnetism of Transition Metals. *Prog. of Theor. Phys.*, 30(3):275–289, 1963.
- [27] H. Bruus and K. Flensberg. Many-Body Quantum Theory in Condensed Matter Physics. *Oxford University Press*, 2004.
- [28] K. Elk, W. Gasser, and E. Heiner. Greensche Funktionen in der Festkörper- und Vielteilchenphysik. *Wiley VCH*, 1st edition, 1979.
- [29] J. E. Hirsch and R. M. Fye. Monte Carlo Method for Magnetic Impurities in Metals. *Phys. Rev. Lett.*, 56:2521–2524, Jun 1986.
- [30] P. Werner, A. Comanac, L. de’ Medici, M. Troyer, and A. J. Millis. Continuous-Time Solver for Quantum Impurity Models. *Phys. Rev. Lett.*, 97:076405, Aug 2006.
- [31] K. G. Wilson. The renormalization group: Critical phenomena and the Kondo problem. *Rev. Mod. Phys.*, 47:773–840, Oct 1975.
- [32] Steven R. White. Density matrix formulation for quantum renormalization groups. *Phys. Rev. Lett.*, 69:2863–2866, Nov 1992.
- [33] H. Kajueter and G. Kotliar. New Iterative Perturbation Scheme for Lattice Models with Arbitrary Filling. *Phys. Rev. Lett.*, 77:131–134, Jul 1996.
- [34] H. Keiter and J. C. Kimball. Perturbation Technique for the Anderson Hamiltonian. *Phys. Rev. Lett.*, 25:672–675, Sep 1970.
- [35] P. H. Dederichs and R. Zeller. Self-consistency iterations in electronic-structure calculations. *Phys. Rev. B*, 28:5462–5472, Nov 1983.
- [36] G. P. Srivastava. Broyden’s method for self-consistent field convergence acceleration. *J. Phys. A*, 17(6):L317, 1984.
- [37] R. Žitko. Convergence acceleration and stabilization of dynamical mean-field theory calculations. *Phys. Rev. B*, 80:125125, Sep 2009.
- [38] N. F. Mott. Metal-Insulator Transition. *Rev. Mod. Phys.*, 40:677–683, Oct 1968.
- [39] F. Gebhard. The Mott Metal-Insulator Transition: Models and Methods. *Springer*, 1997.

- [40] G. Kotliar and D. Vollhardt. Strongly correlated materials: Insights from dynamical mean-field theory. *Physics Today*, 57(3):53–59, 2004.
- [41] J. Joo and V. Oudovenko. Quantum Monte Carlo calculation of the finite temperature Mott-Hubbard transition. *Phys. Rev. B*, 64:193102, Oct 2001.
- [42] R. Bulla, T. A. Costi, and D. Vollhardt. Finite-temperature numerical renormalization group study of the Mott transition. *Phys. Rev. B*, 64:045103, Jun 2001.
- [43] M. Capone, L. de’ Medici, and A. Georges. Solving the dynamical mean-field theory at very low temperatures using the Lanczos exact diagonalization. *Phys. Rev. B*, 76:245116, Dec 2007.
- [44] H. Strand, A. Sabashvili, M. Granath, B. Hellsing, and S. Östlund. Dynamical mean field theory phase-space extension and critical properties of the finite temperature Mott transition. *Phys. Rev. B*, 83:205136, May 2011.
- [45] J. M. Luttinger. Analytic Properties of Single-Particle Propagators for Many-Fermion Systems. *Phys. Rev.*, 121:942–949, Feb 1961.
- [46] P. Hohenberg and W. Kohn. Inhomogeneous Electron Gas. *Phys. Rev.*, 136:B864–B871, Nov 1964.
- [47] W. Kohn and L. J. Sham. Self-Consistent Equations Including Exchange and Correlation Effects. *Phys. Rev.*, 140:A1133–A1138, Nov 1965.
- [48] D. M. Ceperley and B. J. Alder. Ground State of the Electron Gas by a Stochastic Method. *Phys. Rev. Lett.*, 45:566–569, Aug 1980.
- [49] N. Marzari and D. Vanderbilt. Maximally localized generalized Wannier functions for composite energy bands. *Phys. Rev. B*, 56:12847–12865, Nov 1997.
- [50] I. Souza, N. Marzari, and D. Vanderbilt. Maximally localized Wannier functions for entangled energy bands. *Phys. Rev. B*, 65:035109, Dec 2001.
- [51] F. Aryasetiawan, M. Imada, A. Georges, G. Kotliar, S. Biermann, and A. I. Lichtenstein. Frequency-dependent local interactions and low-energy effective models from electronic structure calculations. *Phys. Rev. B*, 70:195104, Nov 2004.
- [52] F. Aryasetiawan, K. Karlsson, O. Jepsen, and U. Schönberger. Calculations of Hubbard U from first-principles. *Phys. Rev. B*, 74:125106, Sep 2006.
- [53] I. A. Vladimir, F. Aryasetiawan, and A. I. Lichtenstein. First-principles calculations of the electronic structure and spectra of strongly correlated systems: the LDA + U method. *J. Phys.: Condens. Matter*, 9(4):767, 1997.

- [54] D. Grieger. Charge self-consistency in an LDA+DMFT framework. *University of Hamburg*, PhD Thesis, 2013.
- [55] D. Sénéchal. An introduction to quantum cluster methods. *arXiv*, 0806.2690v2, Nov 2010.
- [56] D. Sénéchal. Bath optimization in the cellular dynamical mean-field theory. *Phys. Rev. B*, 81:235125, Jun 2010.
- [57] A. Liebsch and H. Ishida. Temperature and bath size in exact diagonalization dynamical mean field theory. *J. Phys.: Condens. Matter*, 24(5):053201, 2012.
- [58] W. von der Linden. Numerical Many Body Physics. *Graz University of Technology*, Lecture Notes: Chapter 3.
- [59] M. Beeler, R. W Gosper, and R. Schroepfel. HAKMEM - Technical report. *Massachusetts Institute of Technology*, 1972.
- [60] A. Mycroft. PROGRAMMING HACKS. <https://www.cl.cam.ac.uk/~am21/hakmemc.html>, 1995. Last access: 02.05.2014.
- [61] E. Anderson, Z. Bai, J. Dongarra, A. Greenbaum, A. McKenney, J. Du Croz, S. Hammerling, J. Demmel, C. Bischof, and D. Sorensen. LAPACK: A Portable Linear Algebra Library for High-performance Computers. *IEEE Computer Society Press*, Supercomputing '90:2–11, 1990.
- [62] E. Anderson, Z. Bai, C. Bischof, S. Blackford, J. Demmel, J. Dongarra, J. Du Croz, A. Greenbaum, S. Hammarling, A. McKenney, and D. Sorensen. LAPACK Users Guide. *SIAM*, 3rd edition, 1999.
- [63] C. Lanczos. An iteration method for the solution of the eigenvalue problem of linear differential and integral operators. *J. Res. Natl. Stand.*, 45:255–282, 1950.
- [64] J. Demmel, J. Dongarra, A. Ruhe, and H. van der Vorst. Templates for the Solution of Algebraic Eigenvalue Problems: A Practical Guide. *SIAM*, 2000.
- [65] M. Knap. Quantum many body properties of strongly correlated lattice bosons and polaritons. *Graz University of Technology*, Master Thesis, 2009.
- [66] A. Ruhe. Implementation aspects of band Lanczos algorithms for computation of eigenvalues of large sparse symmetric matrices. *Math. Comp.*, 33:680–687, 1979.
- [67] W. Nolting. Grundkurs Theoretische Physik 7. *Springer Spektrum*, 7th edition, 2009.

- [68] M. Aichhorn. Ordering Phenomena in Strongly Correlated Electron Systems: Cluster Perturbation Theory Approaches. *Graz University of Technology*, PhD Thesis, 2004.
- [69] S. Pairault, D. Sénéchal, and A.-M. S. Tremblay. Strong-Coupling Expansion for the Hubbard Model. *Phys. Rev. Lett.*, 80:5389–5392, Jun 1998.
- [70] C. Weber, A. Amaricci, M. Capone, and P. B. Littlewood. Augmented hybrid exact-diagonalization solver for dynamical mean field theory. *Phys. Rev. B*, 86:115136, Sep 2012.
- [71] E. N. Economou. Green’s Functions in Quantum Physics. *Springer*, 3rd edition, 2006.
- [72] M. J. Rozenberg, G. Kotliar, H. Kajueter, G. A. Thomas, D. H. Rapkine, J. M. Honig, and P. Metcalf. Optical Conductivity in Mott-Hubbard Systems. *Phys. Rev. Lett.*, 75:105–108, Jul 1995.
- [73] M. Ganahl, M. Aichhorn, P. Thunström, K. Held, G. E. Evertz, and F. Verstraete. Efficient DMFT impurity solver using real-time dynamics with Matrix Product States. *arXiv*, 1405.6728v2, Jul 2014.
- [74] R. Bulla. Zero Temperature Metal-Insulator Transition in the Infinite-Dimensional Hubbard Model. *Phys. Rev. Lett.*, 83:136–139, Jul 1999.
- [75] M. J. Rozenberg, R. Chitra, and G. Kotliar. Finite Temperature Mott Transition in the Hubbard Model in Infinite Dimensions. *Phys. Rev. Lett.*, 83:3498–3501, Oct 1999.
- [76] J. Lagarias, J. Reeds, M. Wright, and P. Wright. Convergence Properties of the Nelder–Mead Simplex Method in Low Dimensions. *SIAM J. Optim.*, 9(1):112–147, 1998.
- [77] O. Parcollet and M. Ferrero. Toolbox for Research on Interacting Quantum Systems, Software Version 1.0.
- [78] R. Bulla, T. A. Costi, and T. Pruschke. Numerical renormalization group method for quantum impurity systems. *Rev. Mod. Phys.*, 80:395–450, Apr 2008.
- [79] R. Žitko. NRG Ljubljana - open source numerical renormalization group code, Software Version 2.3.20.
- [80] R. Bulla. Zero Temperature Metal-Insulator Transition in the Infinite-Dimensional Hubbard Model. *Phys. Rev. Lett.*, 83:136–139, Jul 1999.

- [81] E. Müller-Hartmann. The Hubbard model at high dimensions: some exact results and weak coupling theory. *Z. Phys. B*, 76(2):211–217, 1989.
- [82] I. A. Nekrasov, K. Held, G. Keller, D. E. Kondakov, Th. Pruschke, M. Kollar, O. K. Andersen, V. I. Anisimov, and D. Vollhardt. Momentum-resolved spectral functions of SrVO₃ calculated by LDA + DMFT. *Phys. Rev. B*, 73:155112, Apr 2006.
- [83] G. Keller. Realistic Modeling of Strongly Correlated Electron Systems. *University of Augsburg*, PhD Thesis, Jun 2005.
- [84] I. A. Nekrasov, G. Keller, D. E. Kondakov, A. V. Kozhevnikov, T. Pruschke, K. Held, D. Vollhardt, and V. I. Anisimov. Comparative study of correlation effects in CaVO₃ and SrVO₃. *Phys. Rev. B*, 72:155106, Oct 2005.
- [85] H. Lee, K. Foyevtsova, J. Ferber, M. Aichhorn, H. O. Jeschke, and V. Roser. Dynamical cluster approximation within an augmented plane wave framework: Spectral properties of SrVO₃. *Phys. Rev. B*, 85:165103, Apr 2012.
- [86] T. Yoshida, K. Tanaka, H. Yagi, A. Ino, H. Eisaki, A. Fujimori, and Z.-X. Shen. Direct Observation of the Mass Renormalization in SrVO₃ by Angle Resolved Photoemission Spectroscopy. *Phys. Rev. Lett.*, 95:146404, Sep 2005.
- [87] M.J. Rey, Ph. Dehaudt, J.C. Joubert, B. Lambert-Andron, M. Cyrot, and F. Cyrot-Lackmann. Preparation and structure of the compounds SrVO₃ and Sr₂VO₄. *J. Solid State Chem.*, 86(1):101–108, 1990.
- [88] Y. Tokura and N. Nagaosa. Orbital Physics in Transition-Metal Oxides. *Science*, 288(5465):462–468, 2000.
- [89] S. J. Kang and C. Ozawa. Balls & Sticks, Software Version 1.51.
- [90] D. Manthey. Orbital Viewer, Software Version 1.04.
- [91] K. Schwarz and P. Blaha. Solid state calculations using WIEN2k. *Comput. Mater. Sci.*, 28(2):259–273, 2003.
- [92] K. Kuneš, R. Arita, P. Wissgott, A. Toschi, H. Ikeda, and K. Held. Wien2wannier: From linearized augmented plane waves to maximally localized Wannier functions. *Comput. Phys. Commun.*, 181(11):1888–1895, 2010.
- [93] E. Müller-Hartmann. Correlated fermions on a lattice in high dimensions. *Z. Phys. B*, 74(4):507–512, 1989.

- [94] K. S. D. Beach, R. J. Gooding, and F. Marsiglio. Reliable Padé analytical continuation method based on a high-accuracy symbolic computation algorithm. *Phys. Rev. B*, 61:5147–5157, Feb 2000.
- [95] R. N. Silver, D. S. Sivia, and J. E. Gubernatis. Maximum-entropy method for analytic continuation of quantum Monte Carlo data. *Phys. Rev. B*, 41:2380–2389, Feb 1990.
- [96] H. Strand. Many Body Theory: Iterated Perturbation Theory and Dynamical Mean Field Theory. *University of Gothenburg*, Lecture Notes, 2010.
- [97] M. G. Zacher, E. Eder, R. and Arrigoni, and W. Hanke. Evolution of the stripe phase as a function of doping from a theoretical analysis of angle-resolved photoemission data. *Phys. Rev. B*, 65:045109, Jan 2002.